INVESTIGATING THE IMPACT OF OCEAN WARMING ON ANTARCTIC ICE SHELVES

David Evan Gwyther
Grad. Dip. Mar. Sci., B.Sc. Hons (Qld)

Submitted in fulfilment of the requirements
for the Degree of Doctor of Philosophy

Institute for Marine and Antarctic Studies
University of Tasmania
August, 2015

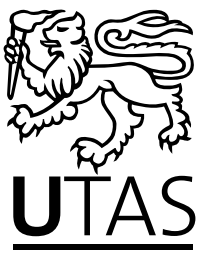

I declare that this thesis contains no material which has been accepted for a degree or diploma by the University or any other institution, except by way of background information and duly acknowledged in the thesis, and that, to the best of my knowledge and belief, this thesis contains no material previously published or written by another person, except where due acknowledgement is made in the text of the thesis.

Signed: _____

David Evan Gwyther

Date: February 2, 2016

Signed: _____

David Evan Gwyther

Date: February 2, 2016

ABSTRACT

The Antarctic ice sheet contains enough ice to raise global sea levels by over 50 metres. The stability of the Antarctic ice sheet and subsequently, projections of future sea level rise, depends strongly on interactions with the Southern Ocean. The ice sheet begins to float around the coastal margins of Antarctica, forming floating ice shelves. These ice shelves buttress the flow of ice sheets into the ocean, and control contributions to sea level rise. Changes to the thickness of ice shelves, such as through melting at the base (basal melting), is thus a critically important factor controlling Antarctic ice discharge, and future sea level. Scientists and field technicians are limited logistically in their ability to observe basal melting in situ and so numerical modelling, such as with the Regional Ocean Modelling System (ROMS), forms an important tool for investigating these critical environments.

In order to produce credible modelling results, key uncertainties in modelling must first be addressed. One such uncertainty is the effect of basal roughness on modulating turbulence within the ice–ocean boundary layer, and how the parameterisation of this affects melting and freezing. Using ROMS with an idealised ice shelf geometry, the link between basal roughness and melting and freezing was explored. A rougher interface led to more turbulent exchange and stronger melting or freezing. This showed that the scheme employed to simulate turbulent mixing across the boundary layer was important for simulating refreezing. Lastly and most importantly, employing a spatially-varying drag coefficient, which was rougher for areas of refreezing and smoother for areas of melting, led to variations in the melt/freeze rate across the entire ice shelf. This is strong motivation for geophysical estimation of this parameter and improving ice shelf–ocean models to account for spatial variability in basal roughness.

Idealised models were also used to investigate how melting responds to changes in the thermal environment of the ocean cavity. The simulations showed that while circulation is weak in a cold ocean cavity environment, it is the strongest driver of melting. This is opposed to a hot ocean cavity environment, where buoyancy driven circulation is strong but melting is mostly strongly driven by heat availability. These simulations further reinforce that melting is not necessarily primarily driven by heat availability and strongest at the deep, grounding line. Instead, melting can be driven by strong flow, such as tides.

The understanding that was further developed through idealised modelling was applied to a realistic scenario: basal melting beneath the Totten Glacier ice shelf, East Antarctica. The Totten Glacier drains a significant portion of the East Antarctic Ice Sheet. The modelled area average basal melt rate was 9.1 m yr^{-1}, which varies on seasonal and interannual ($\sim$ 6-year) time scales. Furthermore, a causal link

was demonstrated between cold, dense water production in the nearby Dalton ice tongue polynya blocking access of warmer off-shelf waters to the Totten ice shelf cavity environment.

Several models of the Totten Glacier ice shelf were run, where the forcing was identical but the shape and geometry of the cavity was varied. Comparing the melt rate of different cavity geometries gives us insight into the sensitivity of melting to geometry and internal variability. The melt rate is relatively insensitive to the shape of the cavity, and instead is controlled by the heat flux into the cavity. These model runs were climatologically forced, and yet displayed significant variability. As a result, any glaciological and oceanographic observations of the Totten Glacier ice shelf should be long enough in order to filter this internal variability. Lastly, a simple linear relationship between ocean water on the adjacent continental shelf to melt rate is developed, which suggests that the current contribution to sea level rise from the Totten Glacier outflow is ~ 0.20 mm yr^{-1}, which under the RCP8.5 scenario, will rise by 80% by 2100.

This thesis improves understanding of the Totten Glacier ice shelf, a possible future cause of significant sea level rise, through explaining the main drivers of melt. Furthermore, these results improve understanding of the uncertainties within ice shelf–ocean numerical models, and help to further constrain projections of sea level change in the future.

ACKNOWLEDGEMENTS

This thesis is the product of more than three years of hard work – and it's fair to say that I am rather proud of it. However, the pathway to completing a Doctor of Philosophy is never straight forward and indeed I don't believe that I would by standing at the end of this path, if not for several people who have helped me along the way.

If not for the patient guidance and insightful direction offered by my supervisors, Ben Galton-Fenzi, Jason Roberts, John Hunter and John Church, I would not be where I am now.

I am especially thankful to my PhD father, Ben, for being a fantastic supervisor. Your infectious drive and passion for science has pushed me to do the best that I could. Your support and belief in me has been amazing; from suggesting that I apply for a Fulbright Scholarship, to flying to Canberra for the Fulbright award ceremony, and to helping drive my PhD research forward when I was on the other side of the world. I could not have done it without you.

And, to my PhD mother Jason, I am so grateful for how generous you are with your time. Your pragmatism has taught me how to approach science in a rational way and your encouraging and positive manner meant a lot to me when things got hard.

My research could not have occurred without the support of several institutes; the Antarctic Climate & Ecosystems Cooperative Research Centre; the Institute for Marine and Antarctic Studies Quantitative Marine Science PhD Program; and, the Australian Research Council Special Research Initiative. Computing resources were provided by both the Tasmanian Partnership for Advanced Computing and the National Computational Infrastructure under grant m68.

To Don Blankenship and Jill Kempf – thank you for taking in two lost Australians and showing us Southern hospitality. You also taught me how to run a meeting properly, and gave me an appreciation for Scandinavian crime shows. To Jamin Greenbaum, Benjamin Wagman and my other Texan friends, thank you for taking us on board and showing us all the amazing things Texas has to offer, like Texas Two-Step and BBQ! I will cherish the memories.

My PhD experience has been vastly improved by the support of Wenneke Ten Hout. Thank you for your constant help to keep my PhD ticking along, shielding me from bureaucracy and lending us your garage to store our gear while we were overseas!

The publications presented in this thesis were improved by comments and suggestions from Malte Thoma, Craig Stevens, Ben Caspani, Guy Williams, Laurie Padman and 4 anonymous reviewers.

To Dad and Mum, thank you for sparking my passion for science and for encouraging me to question and develop an inquisitive mind.

To the Kelly Gang, thank you for your unwavering support.

However, it is to my wife Kathleen that I am most grateful. You are unfailingly positive and your belief in me has given me the courage to attempt what I would not have otherwise done. Thank you being with me every single step of this wild ride. You've pushed, prodded and proofed, and learnt a lot about science and research along the way. With support through the tough times and passion during the good times, you brighten every day, and I am so glad that it's you by my side. *I love you.*

Publications resulting from research completed during candidature

Published/in press
Refereed:

1. **D. E. Gwyther**, B. K. Galton-Fenzi, M. S. Dinniman, J. L. Roberts & J. R. Hunter. *The effect of basal friction on melting and freezing in ice shelf–ocean models*. Ocean Modelling, 95:38–52. doi:10.1016/j.ocemod.2015.09.004. (2015)

2. **D. E. Gwyther**, B. K. Galton-Fenzi, J. R. Hunter & J. L. Roberts. *Simulated melt rates for the Totten and Dalton ice shelves*. Ocean Science, 10(3):267–279. doi:10.5194/os-10-267-2014. (2014)

3. **D. E. Gwyther**, B. K. Galton-Fenzi & J. L. Roberts. *Controls of the basal mass balance of floating ice shelves*. In proceedings of the 18th Australasian Fluid Mechanics Conference, pages 1–4. (2012)

Non-refereed:

4. A. Orsi, N. Zielinski, W. Durkin, P. Clark, C. Wiederwohl, M. A. Rosenberg, B. Huber, **D. E. Gwyther**, J. Greenbaum, C. Lavoie, A. Shevenell, A. Leventer, D. D. Blankenship, S. Gulick & E. Domack. *On the Revealing First-hand Probing of Ocean-Ice-Atmosphere Interactions off Sabrina Coast During NBP1402*, AGU Fall Meeting, 15-19 December 2014, San Francisco, United States, PP24A-02. (2014)

5. **D. E. Gwyther**. *2013 Fulbright Postgraduate Scholar heads south*, The Fulbrighter, Australian-American Fulbright Commission, Canberra, Australia, 2014, July, p.4. (2014)

6. **D. E. Gwyther**, B. K. Galton-Fenzi, J. R. Hunter & J. L. Roberts. *Melt rate predictions for the Totten and Dalton ice shelves from a numerical model*, AGU Fall Meeting, 9-13 December 2013, San Francisco, United States, GC31A-1022. (2013)

7. **D. E. Gwyther**, B. K. Galton-Fenzi, J. R. Hunter & J. L. Roberts. *Oceanic heat flux, on-shelf flow and basal melting of the Totten Glacier, East Antarctica*, Strategic Science in Antarctica, June 2013, Hobart, Australia. (2013)

Submitted/In preparation
Refereed

8. **D. E. Gwyther**, E. A. Cougnon, B. K. Galton-Fenzi, J. L. Roberts, J. R. Hunter & M. S. Dinniman. *Modelling ice shelf melting in a changing ocean cavity environment*. Annals of Glaciology, In review. (2015)

9. J. L. Roberts, B. K. Galton-Fenzi, A. M. Le Brocq, **D. E. Gwyther**, F. Paolo, D. A. Young, A. P. Wright, R. C. Warner, H. A. Fricker, N. W. Young, J. S. Greenbaum, T. D. van Ommen, D. D. Blankenship, M. J. Siegert, T. Payne, S. Cornford & L. Padman. *Variable flow of the Totten Glacier responding to ocean forcing.* In prep. (2015)

10. C. Greene, **D. E. Gwyther** & Donald D. Blankenship *Antarctic Mapping Tools for* MATLAB. Computers & Geosciences, Submitted. (2015)

International conferences attended during candidature

1. International Glaciological Society (IGS) Symposium on Contemporary Ice-Sheet Dynamics: ocean interaction, meltwater and non-linear effects, August 2015, Cambridge, United Kingdom.

2. American Geophysical Union (AGU) Fall Meeting, December 2013, San Francisco, United States of America.

3. Strategic Science in Antarctica, June 2013, Hobart, Australia.

4. 18$^{\text{th}}$ Australasian Fluid Mechanics Conference, December 2012, Launceston, Australia.

Presentations resulting from research completed during candidature

1. Conference poster presentation, "Using idealised models to explore uncertainties in ice shelf-ocean interaction", IGS Symposium, Cambridge, United Kingdom, August 2015.

2. Invited oral presentation, "The effect of roughness on ice shelf basal melting", Ice–Ocean Modelling Workshop, Hobart, Australia, November 2014.

3. Invited oral presentation, "Investigating the Ocean-driven melting of the Totten Glacier Ice Shelf, East Antarctica", Centre for Coastal Physical Oceanography, Norfolk, United States of America, April 2014.

4. Conference poster presentation, "Melt rate predictions for the Totten and Dalton ice shelves from a numerical model", American Geophysical Union (AGU) Fall Meeting, San Francisco, United States of America, December 2013.

5. Conference poster presentation, "Oceanic heat flux, on-shelf flow and basal melting of the Totten Glacier, East Antarctica", Strategic Science in Antarctica, Hobart, Australia, June 2013.

6. Introductory candidature oral presentation, "Investigating the impact of ocean warming on Antarctic Ice Shelves", Institute for Marine and Antarctic Studies, University of Tasmania, Australia, February 2013.

7. Oral presentation, "Controls of the basal mass balance of floating ice shelves". 18^{th} Australasian Fluid Mechanics Conference, Launceston, Australia, December 2012.

Statement of Co-Authorship

The following people contributed to the publication of the work undertaken as part of this thesis:

Paper 1/Chapter 1 (*Controls of the basal mass balance of floating ice shelves*):

- **David E. Gwyther** (75%)
- Benjamin K. Galton-Fenzi (15%)
- Jason L. Roberts (10%)

Paper 2/Chapter 3, in review (*The effect of basal friction on melting and freezing in ice shelf–ocean models*):

- **David E. Gwyther** (75%)
- Benjamin K. Galton-Fenzi (8%)
- Michael S. Dinniman (5%)
- Jason L. Roberts (8%)
- John R. Hunter (4%)

Paper 3/Chapter 4, in review (*Modelling ice shelf melting in a changing ocean cavity environment*):

- **David E. Gwyther** (70%)
- Eva A. Cougnon (8%)
- Benjamin K. Galton-Fenzi (8%)
- Jason L. Roberts (8%)
- John R. Hunter (4%)
- Michael S. Dinniman (2%)

Paper 4/Chapter 5 (*Simulated melt rates for the Totten and Dalton ice shelves*):

- **David E. Gwyther** (75%)
- Benjamin K. Galton-Fenzi (15%)
- John R. Hunter (5%)
- Jason L. Roberts (5%)

Paper 5/Chapter 6, in preparation (*Internal variability, sensitivity to geometry and melt susceptibility of the Totten Glacier*):

- **David E. Gwyther** (80%)
- Benjamin K. Galton-Fenzi (10%)
- Jason L. Roberts (5%)
- John R. Hunter (5%)

Details of the authors' roles:

Benjamin K. Galton-Fenzi contributed with extensive project development and refinement, technical and conceptual aspects, and manuscript preparation.

Jason L. Roberts contributed with project development and refinement, and assisted extensively with technical and conceptual aspects of this research.

John R. Hunter contributed with concept development, technical guidance and manuscript development.

Michael S. Dinniman contributed with extensive technical guidance and manuscript development.

Eva A. Cougnon contributed with model development and manuscript editing.

We the undersigned agree with the above stated "proportion of work undertaken" for each of the above published (or submitted) peer-reviewed manuscripts contributing to this thesis:

Signed: _____
Dr. Benjamin K. Galton-Fenzi
Supervisor
Australian Antarctic Division, and
Antarctic Gateway Partnership, and
Antarctic Climate & Ecosystems Cooperative Research Centre
Date: 3/February/2016

Signed: _____
Prof. Nathan Bindoff
Head, Oceans and Crysophere Program
Institute for Marine and Antarctic Studies
Date: 3/February/2016

TABLE OF CONTENTS

Chapter 1

INTRODUCTION

The Antarctic ice sheet, the single largest mass of ice on the earth, was formed by the accumulation of snow over many millions of years. The East and West Antarctic ice sheets (EAIS and WAIS, respectively) are separated by the Transantarctic Mountains (Fig. 1.1) and have very different properties such as sea level rise potential. This ice flows towards the ocean through both broad, slow ice sheet flow and via many fast flowing ice streams and glaciers. Floating ice shelves form where the ice thickness is insufficient to maintain contact with the bedrock due to the upwards buoyancy associated with the displaced ocean. An ocean-filled cavity, insulated from the atmosphere, forms beneath the ice shelf (Reddy et al., 2010). These ice shelves can range in thickness from 100 m to over 2000 m, and they cover 40% of the ocean southwards of the continental shelf (Holland and Jenkins, 1999). The deep and extensive contact between ice shelves and the Southern Ocean, guarantees that thermodynamic interaction (such as melting) will be an important process controlling mass loss of the Antarctic ice sheets.

Understanding Antarctic mass loss is critical for quantifying current and future sea level change. Antarctica contains enough ice to raise sea level by ∼58 m (Fretwell et al., 2013). Of this, 0.2 m is stored in the ice of the Antarctic Peninsula, 4.3 m is stored within the WAIS and 53.3 m is stored within the EAIS. Of particular importance is ice that is grounded below sea level (marine ice sheet), as it is most susceptible to continued oceanic driving as the grounding line retreats. This may occur in the case of reverse slope bedrock which becomes deeper inland, where a stable grounding line cannot exist due to the so-called Marine Ice Sheet Instability (Schoof, 2007; Bamber et al., 2009). The EAIS contains 19.2 m of marine ice sheet, including 3.5 m from the Aurora Subglacial Basin (Greenbaum et al., 2015).

The WAIS is one such ice sheet displaying rapid mass loss (e.g. Chen et al., 2009; Pritchard et al., 2009), which is due to relatively high drainage through several outlet glaciers and ice shelves. Some of these ice shelves, such as those along the Amundsen Sea coast (for example, Pine Island Glacier and Thwaites Glacier ice shelves), have been shown to be melting rapidly at their base (e.g. Dutrieux et al., 2013). Recent modelling and observational studies suggest that these glaciers are now in the process of retreating inland (Joughin et al., 2014; Rignot et al., 2014).

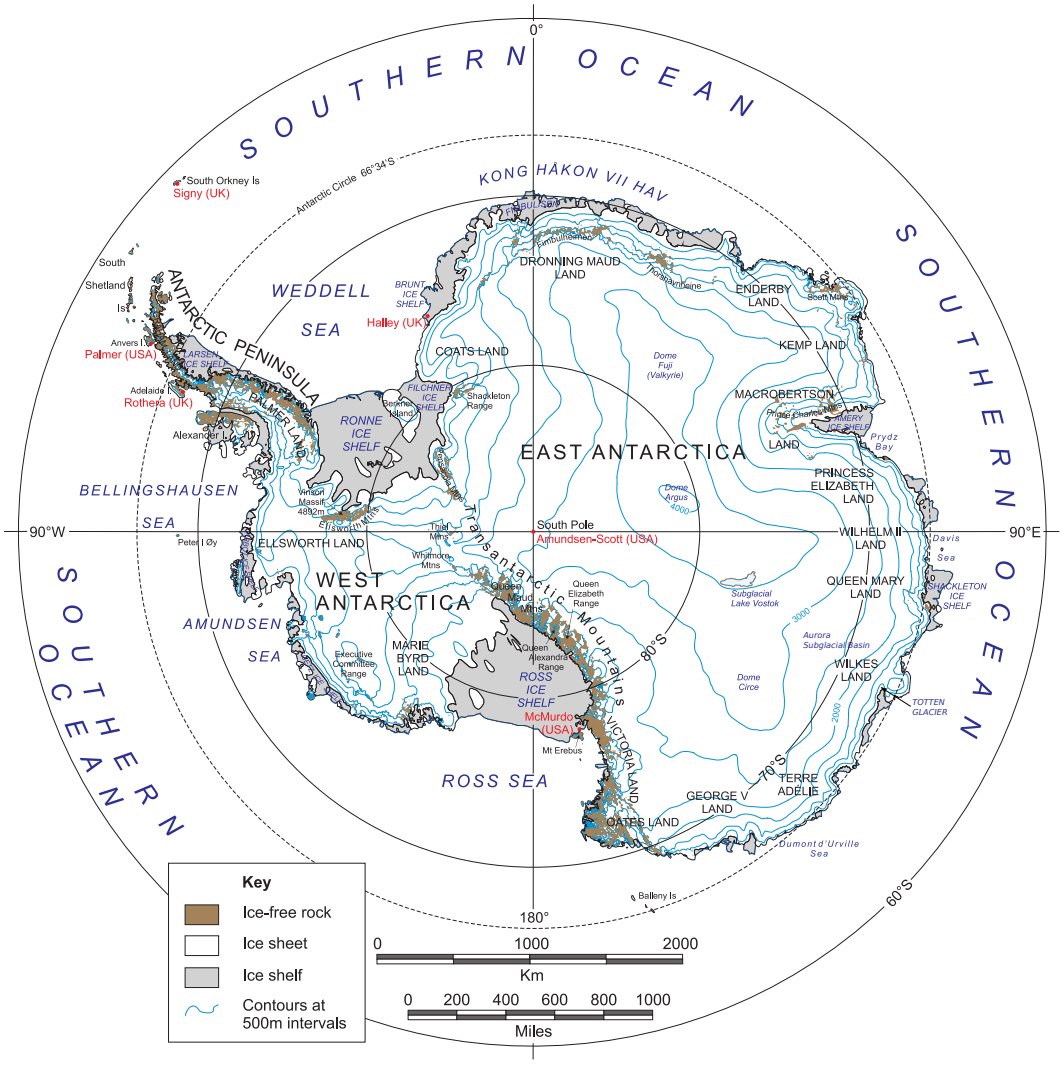

Figure 1.1: Overview of Antarctica, showing West and East Antarctica and the Antarctic Peninsula. Figure courtesy of USGS (http://lima.usgs.gov)

Mass loss from East Antarctica is less certain; outlet glaciers tend to have lower surface change rates and hence the mass balance of the EAIS is smaller in magnitude and higher in uncertainty (Shepherd et al., 2012). Among the glaciers draining the EAIS, the Totten Glacier (Fig. 1.2) has been repeatedly highlighted as a likely source of large mass loss from this region of Antarctica.

Investigating the ice shelf environment through application of ocean models occurred as early as the 1980s (e.g. MacAyeal, 1984; Hellmer and Olbers, 1989). This has continued as models and the parameterisations of the interactions inherent in the ice shelf environment have evolved in complexity. Applications have been 'realistic', modelling a specific geographic region in order to better understand this region or observations taken there (e.g. Dinniman et al., 2003), or 'idealised', with a simplified geometry which approximates an archetypical ice shelf in order to investigate the

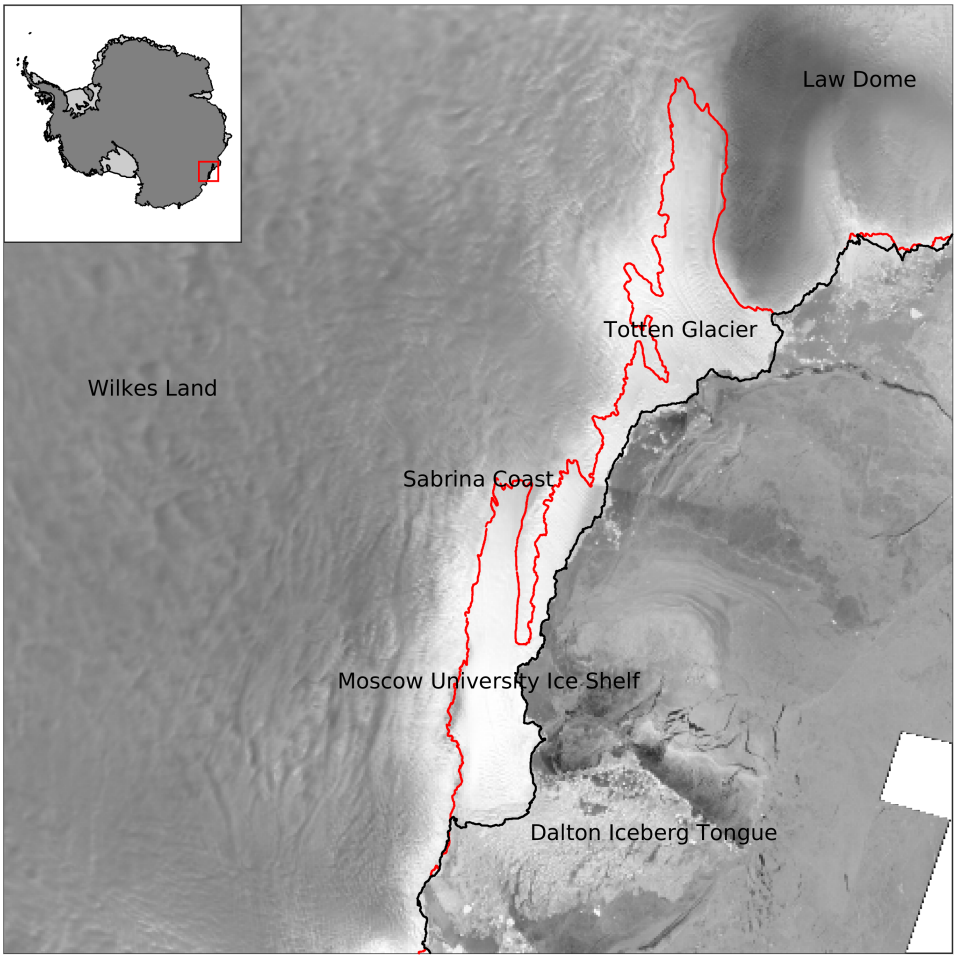

Figure 1.2: Key features of the Sabrina Coast, including the Totten Glacier ice shelf, are marked. The coastline and grounding line are marked with black and red lines, respectively. Inset shows location in Antarctica. Background imagery from RAMP (Radarsat Antarctic Mapping Project; Liu et al., 2001) and compiled with the Antarctic Mapping Toolbox for Matlab (Greene et al., 2013).

fundamental physical processes (e.g. Grosfeld et al., 1997).

This thesis aims to follow a similar route, applying an ocean model to the ice shelf cavity problem. The Regional Ocean Modeling System (ROMS; Shchepetkin and McWilliams, 2005) has been established as being suitable for ice shelf–ocean applications because it is designed for continental shelf applications, and has had significant community modifications to enable ice–ocean interaction. This model has been applied to ice shelves before (e.g. Dinniman et al., 2007; Galton-Fenzi et al., 2012) and has proved to be reliable in reproducing the distribution of melting and freezing (Fricker et al., 2001).

This thesis will investigate the Totten Glacier region in East Antarctica, which is 1) significantly under-studied in ocean modelling and oceanography literature, and 2) potentially critical for accurately projecting future sea level rise. These results

will represent a significant improvement to our understanding of the distribution and magnitude of melting and freezing in this region. The oceanographic processes that drive the ice shelf–ocean interaction will also be explored. Together, these results will also help to inform future observational missions. Further to this realistic application, key uncertainties still present in ice shelf–ocean interaction will be investigated. Uncertainties include the effect of bathymetry and cavity geometry on ice shelf–ocean interaction; ice shelf basal drag affecting turbulent transfer of heat to the ice shelf base; the effect of the ice shelf thermal environment on controlling melt distribution. These uncertainties will be investigated using process-oriented, idealised ice shelf–ocean models.

The objectives of this thesis are summarised as:

- Improve understanding of key uncertainties in ice shelf–ocean interaction
  - To develop understanding of effect of basal friction on melting and freezing; in particular, the importance of spatially varying basal friction.
  - To increase understanding of the fundamental differences between a cold and warm cavity thermal environment without interference from winds and external currents that are present in a realistic application.
- Apply understanding of ice shelf–ocean interaction to a realistic scenario and key relevant uncertainties.
  - To investigate the sensitivity of thermodynamic interaction beneath the Totten ice shelf to the shape of the ice shelf cavity.
  - To model melting and freezing beneath the Totten ice shelf, as compared to glaciological estimates, and diagnose oceanographic or atmospheric drivers for this interaction.
- To make an estimate of the sensitivity of ice shelf–ocean interaction beneath the Totten Glacier ice shelf to external forcing, and hence estimate sensitivity to future climate scenarios.

The remainder of this chapter provides a general overview of Antarctic mass loss, ice shelves and ice sheet stability, and global sea level changes. The oceanography, glaciology and observed changes of the Totten Glacier–Ice Shelf system are introduced, and the future study of this region is motivated. Lastly, uncertainties that govern the interaction between ice shelves and the ocean are introduced.

1.1 Antarctic mass loss

Antarctica has been observed to be losing mass (Vaughan et al., 2013). Several studies, using different measurement techniques, have found the mass balance of the Antarctic ice sheet is negative; the amount of ice removed from the ice sheet through

calving, basal melting and surface ablation is greater than that added through surface accumulation of snow. Zwally et al. (2005) showed, using ERS-1 satellite altimetry data and accounting for varying firn (surface snow layer) compaction, that Antarctica had a mass balance of -31 ± 12 Gt yr^{-1}. Pritchard et al. (2009) used repeat-track laser altimetry from the NASA ICESat satellite while accounting for confounding signals from tides, atmospheric pressure changes, surface accumulation and firn compaction to quantify surface elevation change and show intensified lowering in key Antarctic grounding line regions. Chen et al. (2009) used satellite based gravity estimates from the Gravity Recovery and Climate Experiment (GRACE) to calculate the Antarctic mass balance to be -190 ± 77 Gt yr^{-1}. Flament and Rémy (2012) used repeat-track Envisat observations to confirm thinning and increased mass loss of several Antarctic glaciers, while Rignot et al. (2013) used interferometric Synthetic Aperture Radar (InSAR), to compare volume flux divergence against surface accumulation and quantify strong basal melting of many smaller ice shelves (including Pine Island, Thwaites, Getz, Totten and Shackleton ice shelves). Depoorter et al. (2013) used a steady-state mass balance budget to determine the basal mass balance of Antarctic ice shelves, and showed that it was the medium sized ice shelves (such as Getz, Totten and Pine Island) that were likely experiencing the greatest basal mass loss. However, this mass loss is regionally varying and some regions display mass gain (e.g. Filchner ice shelf is thickening at 1.5 ± 0.5 m decade^{-1} Paolo et al., 2015).

1.1.1 Ice Shelf Buttressing

Increased basal melting and surface ablation leads to the thinning of an ice shelf, a reduction in back stress and buttressing supplied by the ice shelf, and a subsequent acceleration of the upstream ice flow (Hughes, 1973; Weertman, 1974; Mercer, 1978; Thomas and Bentley, 1978). The time scale of changes at the ice sheet–ocean boundary (for example, rapid ice shelf melting or collapse) is short compared to the long response time of the ice sheet interior. This leads to an acceleration in flow rate of the ice stream and causes subsequent local thinning. It is this dynamic coupling between the ice shelf and ice stream which makes the grounded ice sheet susceptible to oceanic changes (Dupont and Alley, 2005). Indeed, ice shelf thinning is highly correlated with the location of warm water and deep bathymetric ocean access, and is coupled with dynamic thinning of the grounded tributary glaciers (Pritchard et al., 2012). Ice shelf-ocean interaction is therefore an important control on the discharge of grounded ice into the oceans and on global mean sea level rise.

1.1.2 Sea level rise

Global mean sea level is increasing, with the largest contributors being the thermal expansion resulting from increased heat storage in the ocean, and increased glacial melting (Church et al., 2013). Instrumental observations of sea level change are derived from tide gauge records and satellite altimetry. Church et al. (2011) found over the period 1972-2008, global sea level rise was observed to be 2.10 ± 0.16 mm yr^{-1}

(1.83 ± 0.18 mm yr^{-1} for the tide gauge only record), while in recent decades the rate has increased; from 1993-2007 an average rate of 3.22 ± 0.41 mm yr^{-1} is inferred (2.61 ± 0.55 mm yr^{-1} from tide gauge only records). Church et al. (2011) also suggest the contribution from the Antarctic Ice Sheet to be 0.43 ± 0.20 mm yr^{-1} for the period 1993-2008. Uncertainty in these estimates needs to account for all the contributions to this rate, such as thermal expansion of the ocean, ice sheet and glacial mass loss, and direct anthropogenic impacts such as groundwater extraction and damming. As Munk (2002) stated when referring to the sea level rise record for the 20^{th} century, "it began too early, it had too linear a trend, and it was too large". Historically, summing all sea level contributions has resulted in estimates inconsistent with observed sea level rise. However, it has lately been shown that the budget could be closed by applying several corrections, such as including the effect of volcanic forcing on oceanic thermal expansion (Gregory et al., 2013). Once these corrections were applied, the budget could be adequately closed, with a small residual which can be attributable to mass loss from the Antarctic Ice Sheet (Gregory et al., 2013). Furthermore, corrections for bias drift in satellite observations leads to a marginally smaller sea level rise of between 2.6 ± 0.4 mm yr^{-1} and 2.9 ± 0.4 mm yr^{-1} over 1993 to mid-2014, as well as an acceleration in the rate of sea level rise (Watson et al., 2015).

Examining historical sea level proxies to assess past sea level change provides us with valuable constraints on sea level contribution during the last interglacial. During the last interglacial, ~125 thousand years ago, proxies indicate global mean sea level peaking between 5.5 m and 9 m higher than present (Dutton and Lambeck, 2012). Only a fraction of this can be explained by contributions from Greenland (for example, ice core records indicate the Greenland ice sheet contributed at most 2 m to global sea level (NEEM community members, 2013)), glaciers and thermal expansion, leading to a substantial contribution originating from the WAIS (approximately 3-4 m contribution; Bamber et al., 2009) and EAIS. This implies that the East Antarctic Ice Sheet may be susceptible to substantial mass loss in the future - and understanding EAIS outlet glaciers currently displaying change is important for projecting future sea level rise.

1.2 An East Antarctic perspective: Totten Glacier

1.2.1 Motivation for modelling of Totten Ice Shelf

The Totten Glacier has been repeatedly highlighted as a source of potential future sea level rise, due to both its large drainage basin with substantial ice volume grounded below sea level and recent elevation changes, (e.g. Zwally et al., 2005; Pritchard et al., 2009; Chen et al., 2009; Pritchard et al., 2012; Flament and Rémy, 2012; Rignot et al., 2013; Depoorter et al., 2013). The Totten Glacier ice shelf is the main focus of this research project. The Totten Glacier, located on the Sabrina Coast to the east of Law Dome, drains some 570,000 km^2 of the East Antarctic ice sheet (Rignot et al., 2008) and has the highest flux of ice mass across the grounding

line in East Antarctica (71.0 ± 3 Gt ice/yr; Rignot et al., 2013). Of this area, a large percentage is from the Aurora Subglacial Basin (Young et al., 2011) and is marine based. Consequently, the stability of this portion of the ice sheet is highly dependent on back pressure from the buttressing ice shelf (Weertman, 1974). In the situation where the grounding line can retreat back to the region of marine ice sheet and an unfavourable bedrock gradient, mass loss could proceed until the entire Aurora Subglacial Basin (ASB) is deglaciated (Young et al., 2011). Observations from multibeam sonar and benthic geology indicate that the continental shelf adjacent to the Totten Glacier to be a region of large previous grounding line advance and retreat (Fernandez-Vasquez et al., 2014) which further strengthens the importance in understanding this region.

1.2.2 Glaciology and observed changes in mass balance

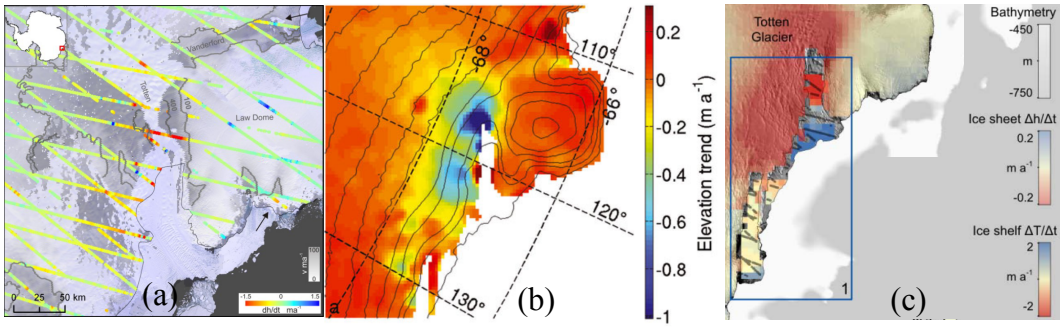

Figure 1.3: (a) Grounded ice satellite-measured altimetry change, from Pritchard et al. (2009) (b) Satellite-altimetry change, as estimated by Flament and Rémy (2012) (c) Ice sheet and ice shelf altimetry change, from Pritchard et al. (2012).

Observations of thinning for the Totten Glacier range include 1.9 m yr^{-1} for the period 2003-2007 (see Fig. 1.3(a) from Pritchard et al., 2009), three times the rate previously reported (Rignot, 2006). Updated satellite altimetry suggests thinning rates of 1.2 ± 0.6 m yr^{-1} on average over the period 2003-2009 (See Fig.1.3(b), from Flament and Rémy, 2012). Interestingly, results from Flament and Rémy (2012) also report spatial variance in strong thinning such as a high thinning signal on the eastern flank of the Totten ice shelf, which could indicate a region of higher melt.

Recently, Paolo et al. (2015) report 18 years of Totten ice shelf elevation change from continuous satellite radar altimetry (Fig. 1.4). Over the study period, 1994–2012, Totten ice shelf area average elevation varies ±40 m from the mean over that period, and displays an interannual variation period of approximately 6 years and a mean linear elevation change for the whole period of $+2 \pm 7.5$ m $decade^{-1}$. However, the size of the uncertainty and the large variation year to year, indicate that the interannual variation in mass balance of the Totten Glacier is large and poorly understood. From the longer time record, it is obvious that the results of Pritchard et al. (2009) (red line; Fig. 1.4), are poorly representative of the longer term change in elevation of the Totten Glacier.

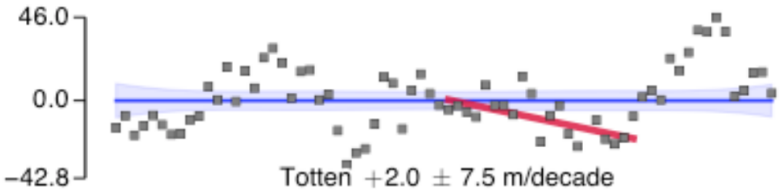

Figure 1.4: Elevation change from 1994–2012 of the Totten Glacier Ice Shelf measured by radar altimeters aboard ERS-1, ERS-2 and Envisat, from Paolo et al. (2015). Totten Glacier displays strong interannual variability, with no trend (blue line) differentiable from the uncertainty. The trend in ICESAT data from 2003–2008 Pritchard et al. (red line; 2009) is not representative of the 1994-2012 trend.

There have been no sub-ice shelf measurements to infer basal melt of the Totten ice shelf. Therefore, basal melt must be inferred glaciologically; flux into the ice shelf system from the ice sheet and snow accumulation is compared to ablation processes such as wind scouring, iceberg calving and basal melt. Area-averaged basal melt for the Totten ice shelf, inferred using this technique, are 20 ± 9 m yr^{-1} (Rignot, 2002); 26 ± 8 m yr^{-1} (Rignot and Jacobs, 2002); and 10.5 ± 0.7 m yr^{-1} (Rignot et al., 2013).

Ice shelf melt is a thermodynamic process, but the controls on the variation, both spatial and temporal, may be due to several different driving factors. These have been well studied and determined in parts of the Antarctic coastline, but the driving factor or combination of factors that influence the delivery of heat, and control the spatial and temporal variation of melt beneath the Totten region ice shelves are unknown. Some of the causes of variation and increase in basal melt include changing ocean dynamics, such as altered circulation patterns (Jacobs et al., 2011) that drive warmer and saltier Modified Circumpolar Deep Water (MCDW) onto the continental shelf (Shepherd and Wingham, 2004); changing local meteorological conditions that led to increased wind strength and upwelling of MCDW onto the continental shelf, but not necessarily to increased basal melting (Dinniman et al., 2012; Steig et al., 2012); and a link between heat for melting and sea ice formation and conditions (Holland et al., 2010; Gwyther et al., 2014).

1.2.3 Oceanography of Totten ice shelf region

Oceanographically, this region is characterised by relative proximity to the southernmost front of the Antarctic Circumpolar Current (ACC). Water bodies present north of Antarctica include Antarctic Surface, Intermediate and Bottom Waters (AASW, AAIW and AABW, respectively), and Circumpolar Deep Water (CDW), the most prominent component of the ACC (Rintoul et al., 2001). The AAIW body outcrops then flows northward and therefore is unlikely to be relevant to ice–ocean interaction around Antarctica. AASW generally forms through atmospheric interaction and is cold and fresh (Whitworth III et al., 1998). AABW, the densest water mass in the region, is formed by mixing of very cold ice shelf melt water and saline shelf

water, and is an important source feeding global overturning circulation (Rintoul et al., 2001). CDW is implicated as an important heat source for melting in other regions of Antarctica (for example, Pine Island Glacier; Jacobs et al., 2011) where the ability of CDW to enter the continental shelf has been well research and is now understood. In this region of East Antarctica, it is uncertain what water masses are present on the continental shelf. In 1996 and 2010, oceanographic cruises measured MCDW (Modified Circumpolar Deep Water, formed as CDW flows on-shelf and mixes with shelf waters) at the shelf break (Bindoff et al., 2000; Williams et al., 2011) adjacent to the Sabrina Coast region. Yet, it is still not known how much of this heat reaches the continental shelf proper, and more importantly, the potential for heat on the shelf to reach the deep grounding lines of the ice shelves.

Once oceanic heat is on the continental shelf, there is a strong dependence on the bathymetry of the seafloor. For oceanic heat to enter a cavity, bathymetric pathways at the correct depth (e.g. deep troughs) must exist for the heat to reach the cavity opening, without any shoals which may steer heat away from the cavity opening. However, much uncertainty remains in the bathymetry of the continental shelf in this region, and particularly in small scale troughs, which have been shown to be important for steering warmer, off-shelf water to ice shelf cavities (Dinniman et al., 2003; Klinck and Dinniman, 2010). Furthermore, it may not even be necessary for relatively warm water to reach the deep grounding lines if there is local production of cold and dense shelf water. This shelf water will likely be the densest water body on the continental shelf, and consequently, will be dense enough to sink to the deep grounding lines. Here, it will be above the in situ freezing point and will thus strongly contribute to melting.

Observational studies in this region are limited. Fast ice is persistent almost year round as the large bay, formed by the edge of Law Dome and the north-south oriented ice tongue, inhibits the advection and removal of sea ice during the transition into the minimum sea ice period during summer/autumn. Since the ice is persistent, fast ice can grow to be relatively thick, and combined with high snowfall rates, severely limits ship access. Consequently, oceanographic research in the bay adjacent to the Totten Glacier has been limited. In January-March 1996, the Baseline Research on Oceanography, Krill and the Environment (BROKE; Bindoff et al., 2000) experiment was conducted along the East Antarctic coastline between 80°E and 150°E. A north-south transect off the shelf break, at longitude 120.3°E, was sampled by CTD (conductivity-temperature-depth) to categorise the water masses present, and investigate the structure of the water at the slope front (see Fig. 1.5). Bindoff et al. (2000) found MCDW present as the deepest water mass at the shelf break and warmer MCDW present just offshore of the shelf break. In September-October 2007, the Sea Ice Physics and Ecosystem eXperiment (SIPEX; Williams et al., 2011) voyage returned to the Totten region, and performed one CTD station on the continental shelf at 118.5°E, 65.6°S. They measured water they categorised as MCDW, south of the continental shelf break, in the vicinity of the BROKE observations of MCDW. Williams et al. (2011) posit that observations of MCDW on the continental shelf in summer 1996 (BROKE), and 10 years later in winter (SIPEX), indicate that there is a strong case for persistent interannual and seasonal

presence of MCDW on the continental shelf in this region (see Fig. 1.5). The other research in this region has been mainly non-oceanographic. Operation Highjump surveyed the western edge of the Dalton ice tongue in 1946-49, performing scattered depth measurements and a Japanese seismic line was shot over the continental shelf break in 1983. The Investigating the Cryospheric Evolution of the Central Antarctic Plateau (ICECAP) project, involved extensive airborne geophysics surveys of the entire Aurora Subglacial Basin, and most recently, of the floating portion of the Totten and Dalton ice shelves. These missions used ice-penetrating radar to infer depth to the bedrock of grounded ice, and potential fields such as gravity and magnetics to infer depth to bathymetry (Young et al., 2011; Roberts et al., 2011; Greenbaum et al., 2015). These missions will prove crucial to future study of this region, as the important constraints the ICECAP data places on the bathymetry in this region will help ensure realistic ocean modelling results. Furthermore, repeat tracks flown by ICECAP will shed light on ice mass loss in this region, which helps to pinpoint regions of potentially higher basal melt. In January-March 2014, the R/V Nathaniel B. Palmer icebreaker visited the Mertz and Totten regions where the icebreaking abilities of this vessel allowed entry into the Totten basin. While this cruise was not purely oceanographic (there was a strong emphasis on multi-beam sonar measurements for bathymetry and marine geology sediment coring to understand the past glacial environment), many CTD stations were performed.

Since this system is largely an oceanographic mystery, modelling presents a powerful method to not only improve understanding of possible continental shelf processes but also inform future observational missions. Khazendar et al. (2013) were able to show a link between satellite measured altimetry change and polynya activity. Chapter 5, will demonstrate a link between the seasonal and interannual fluctuations in ice formation and the melt rate of the two nearby ice shelves (Gwyther et al., 2014).

The Totten Glacier region is characterised by; being relatively unexplored and uncharacterised, especially in terms of hydrography and bathymetry; highly likely to be experiencing rapid ice loss and ice shelf basal melt; an important possible source of potential sea level rise, and very likely important to Antarctica mass loss. Questions that remain to be answered include:

- What is the basal melt of the Totten Glacier ice shelf system?
- What is the hydrography on the continental shelf and what continental shelf processes influence heat transport on the shelf?
- What is the effect of the largely undetermined bathymetry on continental shelf flow?
- How does ice shelf cavity shape and characteristics affect basal melt distribution?

This thesis will attempt to address these questions to improve understanding of this important glacial system.

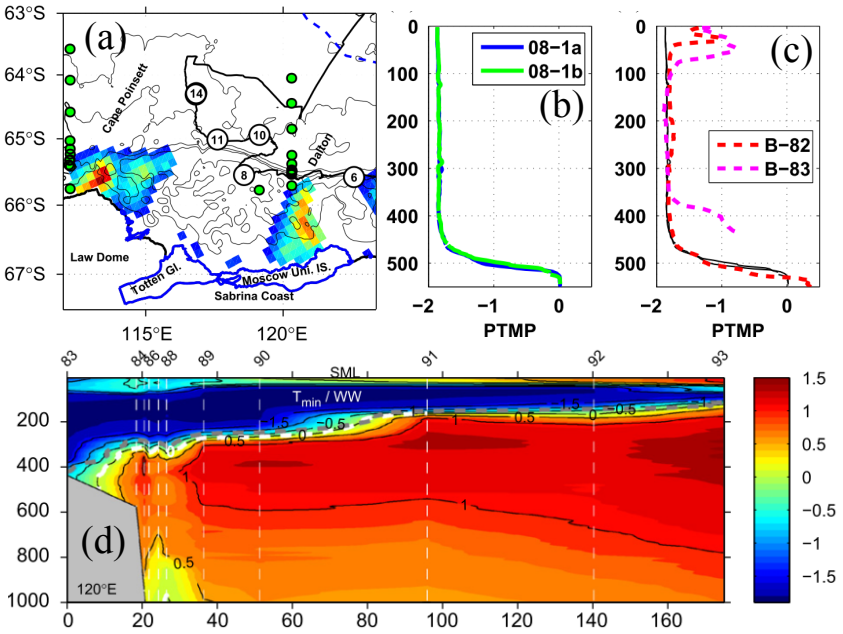

Figure 1.5: (a) SIPEX CTD stations (white numbered circles) and BROKE transect (green circles) in the Totten region. (b) Potential temperature variation with depth for SIPEX station 8 (c) Potential temperature variation with depth at BROKE stations 82 and 83 (d) 120°E BROKE temperature transect. All plots from Williams et al. (2011).

1.3 Uncertainties in ice shelf–ocean interaction

The physical properties of ice and water (such as density, heat capacity and thermal diffusivity) are well known. However, uncertainties in the interaction of ice and water still remain. This section will report the key uncertainties in ice shelf–ocean interaction and demonstrate why they are important yet illusive to solve.

With the exception of Section 1.3.1 and Section 1.3.3, this section is sourced (with modifications for formatting, flow, sectioning and an update of references) from the peer-reviewed conference proceeding: Gwyther, D. E., Galton-Fenzi, B. K., and Roberts, J. L. Controls of the basal mass balance of floating ice shelves. In *18th Australasian Fluid Mechanics Conference*, pages 1–4, 2012.

1.3.1 Cavity and ice shelf geometry

Accurate geometry of the continental shelf and ice shelf cavity is important for realistically simulating flow. One consequence of poorly observed continental shelf bathymetry is degradation in the accuracy of simulated flow across the continental shelf break of off-shelf waters such as MCDW (Klinck and Dinniman, 2010). Likewise, the geometry of ice shelf cavity entry pathways are critical to allowing or inhibiting oceanic heat flow into an ice shelf cavity. If the cavity entry pathway is

too shallow then lower density, cold surface waters are likely to fill the entranceway and prohibit the inflow of warmer continental shelf waters of mid-density. If the cavity entranceway is modelled too deep, then water denser (and possibly warmer) than reality can possibly flood the cavity. The shape of the cavity (the difference between the elevation of the ice shelf basal surface and the bathymetry) is important as it helps to control the degree of thermal forcing of the ice–ocean interaction. Deeper ice shelf cavities lead to a stronger depression of the freezing point, and hence strong thermal forcing and melt rate. The cavity shape is also important for controlling the flow pathways and internal circulation in the cavity, in particular, the pathways of inflow and outflow water, high melt and low melt and likely regions of refreezing.

Logistical issues make in situ measurements of cavity geometry difficult. However, ice thickness can be measured with airborne ice-penetrating radar (Young et al., 2015). The returning radar echo will contain information on the distance to the major dielectric interfaces (air-ice and ice-water). Taking into account aeroplane elevation and ice and air density, the depth below mean sea level of the ice-water interface can be estimated with relatively high accuracy ($\mathcal{O}(10)$ m error in ice thickness). High EM absorption by water means that radar signal cannot penetrate to the lower water-bedrock interface. Instead, bathymetry must be estimated with an 'inversion' model. Airborne gravitimetric measurements combined with estimates of bedrock density can be inverted for 'depth to basement' (Greenbaum et al., 2015). This kind of bathymetry estimate will have larger uncertainties (as compared to ice penetrating radar observations), as 1) estimations must be made for bedrock properties (density, sediment depths) 2) gravity meter observations are susceptible to interference and 'leakage' of signals close to the grounding line, and 3) the footprint of the gravity signal is large (on order of 2 km for most modern instruments, which is partly a function of aircraft speed). The alternative to airborne bathymetry inversions is to directly measure the bathymetry, either with a bottom-scanning sonar (mounted on an autonomous underwater vehicle (AUV) platform) or with seismic/sonar measurements conducted through boreholes in the ice shelf. In the former case, AUV deployment from an icebreaker is expensive and hindered by sea ice close to the ice shelf (a particular issue in the Sabrina Coast region), while in the latter case, deep crevasses limit surface activities on the Totten Glacier.

Greenbaum et al. (2015) conducted an extensive airborne geophysics analysis of the Totten Glacier and ice shelf as a part of the ICECAP consortium (Fig. 1.6). They found the grounding line region at the south of the cavity to be deep ($\sim$ 2500 m below MSL), shallower regions at the calving front, with deep depressions near the centre of the cavity mouth and to the east of grounded peninsula (on the far east side of the cavity opening). Deep basins intrude along the main glacier flow path and along the eastern edge of the ice shelf. The eastern deepening has previously been shown to have no ocean access, however, Greenbaum et al. (2015), with higher horizontal resolution than previous studies, indicate this channel to have deep ocean access. This new pathway, allowing ocean heat access to the grounding line, could explain localised mass loss observed in this region (Flament and Rémy, 2012).

As an illustration of the uncertainty in bathymetry in this region, Greenbaum et al.

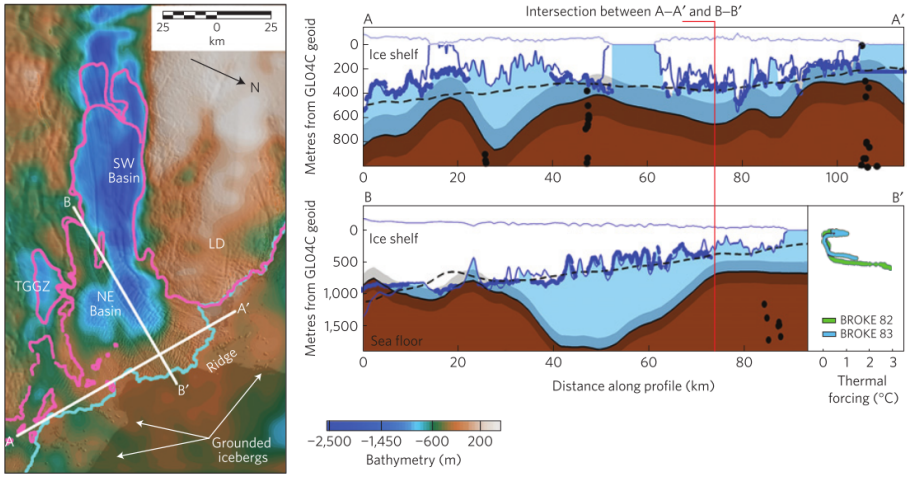

Figure 1.6: Bathymetry inversion for the Totten Glacier region, with ice and bedrock geometry along the AA' and BB' transects, as taken from Greenbaum et al. (2015).

(2015) posit the existence of a previously undetected channel, 3-5 km wide, connecting the ocean to the eastern side of the cavity. This channel is likely too thin to be detectable by InSAR, and hence is not reported by Rignot et al. (2011). The bathymetry produced by Greenbaum et al. (2015) should be thought of as the best current representation of the Totten cavity bathymetry.

1.3.2 Errors and Approximations in Thermodynamics

Melting and freezing at the ice shelf base is a thermodynamic process, whereby heat energy is removed from the ocean to melt ice, and vice versa. This occurs at the thin liquid water layer immediately adjacent to the ice interface, which is not resolvable by a standard numerical ocean model. Hence, parameterisations of the thermodynamics must be introduced (see Section 2.4), and along with that, uncertainties and assumptions. The first uncertainty that is implicitly included is in the freezing point of water.

The freezing temperature of water (T_B) as employed in the three-equation parameterisation (Holland and Jenkins, 1999), is the linearised version of the true, non-linear relationship. Since T_B is integral to numerically solving for the temperature and salinity characteristics at the ice–ocean interface, it is computationally efficient to use the linearised equation. Linearisation of T_B introduces an error, as shown in Fig. 1.7, which becomes more important with depth.

The choice of description of the temperature profile through the ice shelf is also important for the melt rate, as heat is conducted from the ice–ocean interface into the ice shelf while melting and freezing are occurring. The ice shelf temperature profile is constrained at the surface by the ice shelf surface temperature ($\sim -20°C$, but varying seasonally and annually) and at the base by the freezing temperature.

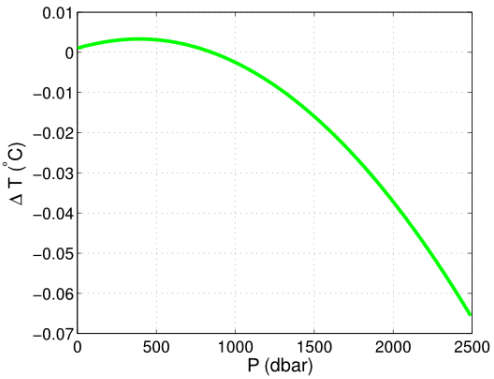

Figure 1.7: The difference between linearised and non-linearised freezing temperature (TEOS-10; IOC and SCOR and IAPSO, 2010) as a function of depth is shown (with salinity constant at 34.4 psu).

Observations and modelling show the temperature profile between the surface and base is dependent on melt rate (Humbert, 2010). Strong melting causes rapid temperature drop to cold internal temperatures over a short length, as ice is being removed before the temperature of the interior can equilibrate. For freezing regions the curve is reversed, with temperatures close to T_B for most of the profile, before it rapidly asymptotes to the surface temperature. To correctly parameterise heat flux into the ice shelf, the gradient of ice shelf temperature (T_I) evaluated at the base of the ice shelf ($z = b$),

$$\left.\frac{\partial T_I}{\partial z}\right|_b \tag{1.1}$$

must be determined. Four approximations for this profile are investigated; Case A, a linear temperature profile, varying from surface to freezing temperature over very small ∂z; Case B, a linear temperature profile, varying from the surface temperature to the freezing temperature, over large ∂z. Both of these are linear profiles; Case C, a more realistic non-linear profile is achieved by assuming constant vertical advection and vertical diffusion (Holland and Jenkins, 1999). The resulting parameterisation is valid when thermal forcing is greater than ~ 0.2 °C and for thick ($\geq$1000 m) ice shelves; and Case D, insulating ice, i.e. the ice is at basal freezing temperature.

The effect of the 4 parameterisations of $\left.\frac{\partial T_I}{\partial z}\right|_b$ on the relationship between melt rate and thermal forcing (T^*; difference between temperature adjacent to the base and the in situ freezing point at the base), is shown in Fig. 1.8. As different rates of heat conduction into the ice shelf will change the heat available for melting at the ice–ocean interface, the ice shelf thermal profile is expected to be important for ice shelf melting. High T^* leads to high melt rates with all parameterisations of ice temperature profile. At high thermal forcing, A, B and D all over-estimate melt rate, because they do not capture the ability of heat to diffuse quickly upwards through the shelf (Holland and Jenkins, 1999). Only C, which includes the vertical velocity of ice, correctly captures the magnitude of the gradient for high melt rates. When ∂z is small, A, switches to a freezing regime at very low but non-zero thermal

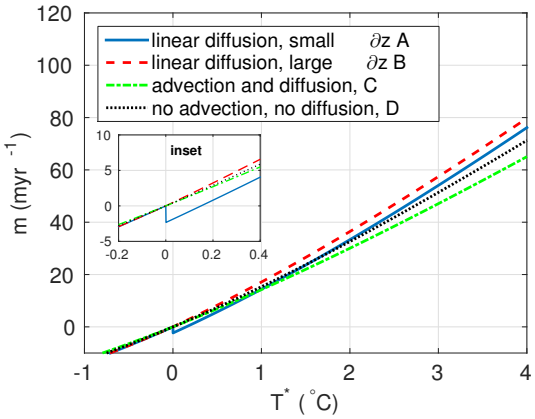

Figure 1.8: Melt rate (m yr^{-1}) is shown as a function of the thermal forcing, for different ice temperature profiles. These profiles are linear diffusion (small ∂z, case A, large ∂z ice case B), advection and diffusion, case C, and the no advection and no diffusion case D.

forcing. This switch to freezing captures the effect of heat conduction upwards into the ice exceeding the supply of heat into the surface layer from the mixed layer. B and D both have shallow temperature gradients, and thus energy is not removed quickly, and melt rates go to zero with the thermal forcing. The profile with advection and diffusion, C, also does not describe the melt-to-freeze flip accurately as approximations were made which do not hold at low melt rates.

Problems exist in all parameterisations of the ice temperature profile. The most advanced description, with constant vertical advection and diffusion, which describes high melting scenarios well, includes approximations which are not applicable at low melt rates or thin ice shelves. Similarly, the other cases here do not describe high melt rate scenarios well. While there are several ice shelves showing high melting at great depth, there are large areas of thinner ice at low thermal forcing values. Consequently, the low ∂z ice, linear temperature profile (which describes low thermal forcing scenarios well) would be suitable for these low melt ice shelves.

1.3.3 Subglacial Freshwater Input

Another potentially important but little understood factor impacting basal melting and freezing is subglacial freshwater flux. Ice melting at the base of the ice sheet and surface melting (an important factor in Greenland, but probably not Antarctica) will drain towards either inland subglacial lakes or to the Antarctic grounding line. These drainage pathways are complicated by the pressure exerted from the ice sheet above. Subglacial freshwater flux across the grounding line has been shown to be an important factor controlling melting of tidewater glaciers in Greenland (Motyka et al., 2013; Kimura et al., 2014). However, in Antarctica where glaciers terminate in ice shelves with deep ocean-filled cavities rather than continually calving at the grounding line (as is the case with tide-water glaciers), subglacial freshwater input

is difficult to study.

The effect of buoyant and cold freshwater input at the grounding line of ice shelves (and tide-water glaciers) is modelled in Jenkins (2011). Using a plume model to simplify the complex ice shelf system, the convective motion that results from subglacial freshwater input is modelled. As the plume rises, it grows through entrainment, the impact on melting along the ice shelf face is modelled. These results show that subglacial freshwater flux has the biggest impact immediately adjacent to the grounding line, where the increased buoyancy increases the plume velocity and hence melting. Further from the grounding line, the impact of subglacial freshwater is lessened, as meltwater input from ice shelf basal melting becomes more important (Jenkins, 2011).

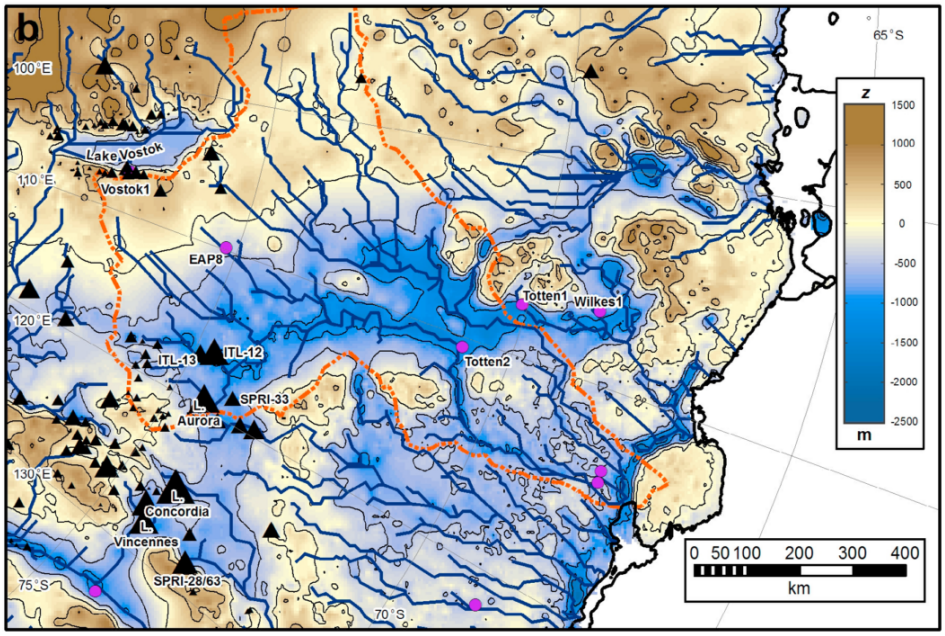

Figure 1.9: Subglacial hydraulic network, lakes and the Totten Glacier catchment plotted over the ICECAP bedrock topography, from Wright et al. (2012). Dashed orange line shows Totten Glacier catchment boundary, black triangles and purple circles are subglacial lakes detected from ice-penetrating radar and satellite-observed elevation change, respectively.

Furthermore, there is evidence for an extensive, channelised subglacial hydrology (see Fig. 1.9) beneath the ASB, part of which drains through the Totten Glacier (Wright et al., 2012). Implications from the airborne ice-penetrating radar study, combined with satellite altimetry observations (Smith et al., 2009), are 1) an extensive hydrological network connecting the ASB to the deep grounding line of the Totten Glacier 2) evidence for shallow subglacial lakes, and 3) history of a subglacial lake drainage event between November 2003 and May 2005 (approximately equivalent volume of 0.58 km^3 drained). The effect of this potentially large and time-varying buoyancy input to the grounding line of the Totten Glacier is unknown.

As the ice shelf basal environment is very difficult to sample in situ, satellite observations of the surface are often used to infer conditions at the base of the ice shelf. Le Brocq et al. (2013) presented evidence for a persistent channelised subglacial freshwater drainage system from airborne ice-penetrating radar observations which are also detectable downstream of the grounding line, as surface features on the ice shelf visible from satellite. From this, Le Brocq et al. (2013) infer that subglacial freshwater input from the channelised hydraulic system flows into the cavity, driving strong convective motion and hence increasing basal melt at the grounding line. This increased melt thins the ice shelf which is visible as a lowering in surface elevation beginning at the grounding line adjacent to the detected subglacial channel.

1.3.4 Basal Roughness

The roughness at the ice–ocean interface is important for dictating the turbulent exchange of heat and salt across and within the boundary layer that separates the ice from the deeper cavity below. As this is a sub-grid scale process in models that employ the Reynolds-averaged Navier-Stokes equations of flow, turbulence resulting from surface stress must be parameterised (see Chapter 2).

In ocean models, the hydraulic roughness of the ice–ocean interface is typically parameterised by a non-dimensional drag coefficient, C_D. In most ocean models, it is assumed constant, even though it is a function of the characteristic roughness scale of the surface, z_0 and the current profile,

$$C_D = \left(\frac{\kappa}{\ln(z/z_0)} \right)^2 \tag{1.2}$$

where $\kappa = 0.41$ is the von Kàrmàn constant.

The parameterisation of C_D was originally developed for atmospheric boundary layers (Paulson, 1970) and was initially applied to turbulence studies under sea ice, but is complicated in this application by the different basal conditions (Craven et al., 2009; Jenkins et al., 2010) beneath deep ice shelves. The roughness scales that exist sub-ice shelves are wide, ranging from $1{\times}10^{-3}$ m, to much larger features such as crevasses and rifting spanning ∼100 m. It is unclear how the drag coefficient will respond to this large range of roughness. In order to quantify basal roughness beneath ice shelves, more extensive observations must be taken. However, the logistical constraints makes studying the physical environment to choose parameters relevant to Eq. 1.2 exceptionally difficult and as a result, will remain elusive until extensive field measurements can be made.

The effect of basal roughness on melting and freezing at the ice shelf base can be investigated by employing the common three-equation parameterisation (Holland and Jenkins, 1999), and calculating melt rates for various thermal forcing and C_D values (see Fig. 1.10). With a small thermal forcing (T^*), the choice of C_D is less important. However, at high T^*, melt rate varies strongly with C_D. Considering that the regions that demonstrate rapid thinning, such as Pine Island Glacier (Pritchard et al., 2009), also exhibit strong in-flow of water well above the in situ

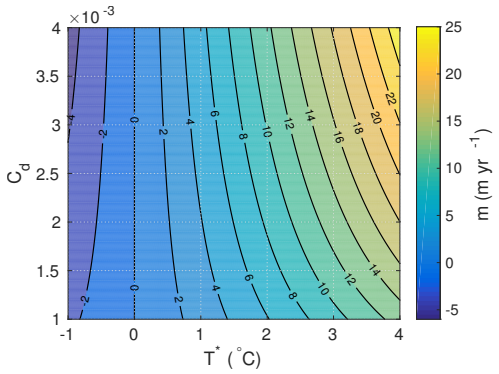

Figure 1.10: The melt rate as determined by the parameterisation of Holland and Jenkins (1999), for a range of thermal forcing (T^*) and C_D. Contours are labled for melt rate.

freezing temperature (i.e. large thermal forcing) then it is expected that the choice of C_D is important for modelling accurate melt rates.

1.4 Thesis Outline

The outline for this thesis is:

Chapter 2 will explain the model used to investigate ice shelf–ocean interaction. The primitive equations of ocean motion, ocean modelling approximations and the time stepping process will be summarised. Key aspects of ROMS will be covered, including vertical and horizontal grids, and modifications for ice shelves. This chapter will provide a brief but concise overview of numerical ocean modelling, and in particular how ROMS solves the ice shelf–ocean interaction problem.

Chapter 3 will describe the effects of basal friction on melt rate and circulation. The most common ice shelf–ocean parameterisation will be described and an idealised application of ROMS will be used to explore how basal friction alters circulation and heat transfer across an ice shelf. Modifications will be made to the ROMS code to allow for a basal friction that can vary spatially and temporally, and the effect of this on melting and freezing at the interface will be tested.

Chapter 4 will investigate the variation in melting and freezing of an idealised ice shelf between different cavity thermal environments. The three-equation parameterisation of ice–ocean thermodynamic interaction will be further explored, and in particular, the application of this parameterisation in the absence of strong buoyancy-driven circulation. A simple parameterisation of tides will test the impact of tides on cold ocean cavity basal melting.

Chapter 5 will apply the understanding of ice shelf–ocean interaction to the Totten Glacier ice shelf region in East Antarctica. ROMS will be used to explore basal melting and freezing, in comparison to glaciological estimates, for the period 1992–2007. The model results explain oceanographic and atmospheric drives for

controlling interaction between the ice shelf and the ocean.

Chapter 6 will further investigate the Totten Glacier ice shelf region with updated bathymetry and topography for the ice shelf cavity. This will enable a comparison study to explain the sensitivity of the regional distribution and magnitude of melting and freezing to cavity geometry. These models will be forced with an average year climatology and updated to 1992–2012 forcing.

Chapter 7 will synthesise these results and conclude this thesis. The major improvements in understanding of ice shelf–ocean modelling will be summarised. An overview of the Totten Glacier ice shelf system will be given and the implications for this system in the face of future climate scenarios will be presented. Lastly, potential future research will be highlighted.

Chapter 3 and Chapter 5 are sourced from peer-reviewed articles published in the literature (Gwyther et al., 2014, 2015), while Chapter 4 has been submitted (Gwyther et al., submitted 2015b). As such, they will appear here as they were published, excepting minor changes for formatting and the removal of the abstract. However, it is important for this thesis to tell a coherent story. This thesis fits together thus: Chapter 1 and Chapter 2 motivate why ice shelf basal melting is important for sea level rise, and how ocean models can help us answer this. Chapter 3 begins to investigate some of the uncertainties (principally, basal drag) inherent in ice shelf–ocean interaction using an idealised geometry model. Chapter 4 applies the same idealised geometry model, where now the focus is on the effect of tides and cavity thermal environment on basal melting. Chapter 5 shifts to a realistic domain (the Totten Glacier ice shelf) and investigates processes driving interannual variation in basal melting. Chapter 6 provides a more detailed investigation of variation in basal melting for the same realistic application. Chapter 7 concludes the main outcomes of this thesis. Together, Chapters 3-6 investigate uncertainties in ice shelf–ocean interaction through idealised and realistic applications.

Chapter 2

METHODS & ROMS

Numerical ocean models are a powerful tool for investigating the sub-ice shelf environment. This chapter outlines the mathematical basis for solving for fluid flow, common approximations employed, and introduces the model used throughout this study.

Ocean circulation models are an appropriate tool to study the sub-ice shelf environment as they represent realistic physics and can use observations to determine initial and boundary conditions and geometry, resulting in accurate, repeatable and relevant experiments. One such model is the Regional Ocean Modeling System (ROMS; Shchepetkin and McWilliams, 2005), a three-dimensional, free-surface (for example, to allow surface waves and tides), terrain-following vertical coordinate (the vertical discretisation of cells varies with ocean depth) numerical ocean model, that solves the primitive equations (Reynolds-averaged Navier Stokes equations) using both the Boussinesq and hydrostatic assumptions. ROMS uses split timesteps to solve the barotropic and baroclinic modes. The vertical discretisation allows increased resolution in the surface and bottom layers, and lower resolution in the middle layers, making this model well suited for coastal processes studies. The configuration details of the models used in each chapter of this thesis are shown in Appendix C.

There are modifications for ROMS that simulate the thermodynamic interaction between the ice and ocean. The influence of ice shelves are represented by heat exchange between ice and ocean, as well as an increase in water pressure due to the height of ice floating above (Dinniman et al., 2007; Galton-Fenzi et al., 2012). Frazil are small ice crystals suspended in the water column and are important as they refreeze onto the shelf base. They are simulated using an implementation of the equations that govern the growth and accretion rate of frazil crystals (Galton-Fenzi et al., 2012). Furthermore, the seawater equation of state utilised by ROMS is only valid above $-2°C$, which is insufficient for studies of the polar regions, and particularly at the deep grounding lines, where the water can be colder than $-2°C$. Consequently, ROMS has been modified to include an equation of state accurate for temperatures down to $-6°C$ (Galton-fenzi, 2009).

Using ROMS modified for ice-ocean interaction as described above, this thesis will

shed light on the processes involved in the melting and freezing of Antarctic ice shelves.

2.1 Solving the equations of motion

To simulate ocean flow, ROMS solves the primitive equations. The primitive equations are derived from the Navier-Stokes equations, which together with conservation of heat and mass and an equation of state, describe large-scale motion of momentum and tracers within the ocean (Pedlosky, 1982).

The momentum equations are typically split into zonal/meridional components of momentum and a vertical component. The zonal and meridonal equations are

$$\frac{\partial u}{\partial t} + u\frac{\partial u}{\partial x} + v\frac{\partial u}{\partial y} + w\frac{\partial u}{\partial z} - fv = -\frac{1}{\rho}\frac{\partial p}{\partial x} + A_H\frac{\partial^2 u}{\partial x^2} + A_H\frac{\partial^2 u}{\partial y^2} + A_V\frac{\partial^2 u}{\partial z^2} \quad (2.1)$$

$$\frac{\partial v}{\partial t} + u\frac{\partial v}{\partial x} + v\frac{\partial v}{\partial y} + w\frac{\partial v}{\partial z} - fu = -\frac{1}{\rho}\frac{\partial p}{\partial x} + A_H\frac{\partial^2 v}{\partial x^2} + A_H\frac{\partial^2 v}{\partial y^2} + A_V\frac{\partial^2 v}{\partial z^2}, \quad (2.2)$$

respectively, while the vertical momentum equation is

$$\frac{\partial w}{\partial t} + u\frac{\partial w}{\partial x} + v\frac{\partial w}{\partial y} + w\frac{\partial w}{\partial z} = -\frac{1}{\rho}\frac{\partial p}{\partial z} - g + A_H\frac{\partial^2 w}{\partial x^2} + A_H\frac{\partial^2 w}{\partial y^2} + A_V\frac{\partial^2 w}{\partial z^2}. \quad (2.3)$$

In these equations, u, v and w are the zonal, meridonal and vertical velocities, respectively, and x, y and z are the unit vectors of the same directions, respectively. The pressure is p, time is t, the Coriolis parameter is f, ρ is the density, g is the acceleration due to gravity, while A_H and A_V are the horizontal and vertical eddy viscosities, respectively (Pedlosky, 1982).

The first term in Eqs. 2.1-2.3 is the fluid acceleration in the respective direction. The terms of form

$$u\frac{\partial u}{\partial x} + v\frac{\partial u}{\partial y} + w\frac{\partial u}{\partial z} = \vec{v}\cdot\nabla u,$$

represents how the flow transports properties, and represent advection. Advection requires a gradient in the property (whether that property is velocity or a tracer such as temperature) in order to change the local value of the property, as reflected by the presence of the gradient derivative, ∇u. Together, the first four terms on the left hand side (LHS) are the 'material derivative', which describes the rate of change in time of a physical quality subject to a velocity field which varies in space and time. The last term on the LHS accounts for the Coriolis force. The Coriolis parameters, varies with latitude, ϕ, as $f = 2\Omega sin\phi$ where $\Omega = \frac{2\pi}{24\text{hours}}$ is the rotation rate of the Earth. Thus, a typical value for the Coriolis parameter in the Antarctic coastal seas is $f = -1.3 \times 10^{-4}$ s^{-1}.

The first term on the right hand side (RHS) of Eqs. 2.1-2.3 is the horizontal pressure gradient force, which accounts for the force due to differences in pressure. In the vertical momentum equation (Eq. 2.3), the acceleration due to gravity is accounted

for through including $-g$. The final three terms on the RHS of Eqs. 2.1-2.3 represent frictional forces which redistribute momentum and decelerate the flow. For example, frictional stress, τ originating from the vertical difference in velocity can be described by,

$$\tau^z \propto \mu \frac{\partial u}{\partial z}.$$

where μ is the dynamic fluid viscosity (which is related to the kinematic viscosity, ν by $\nu = \frac{\mu}{\rho}$). The variation of this frictional stresses in space leads to a flow acceleration,

$$\frac{\partial \tau^z}{\partial z} \propto \nu \frac{\partial^2 u}{\partial z^2}.$$

It is common practice to treat the fluid viscosity as including the effect of turbulence, $A_{H/Z}$, as both molecular viscosity and turbulence result in the same macro scale redistribution of momentum.

It is also common to add a term to account for effects of external forcing through a horizontal dissipation, $\mathcal{F}_u + \mathcal{D}_u$ and $\mathcal{F}_v + \mathcal{D}_v$ to Eq. 2.1 and Eq. 2.2, respectively.

Furthermore, there are three additional equations which must be obeyed. Conservation of mass is

$$\frac{\partial \rho}{\partial t} + \frac{\partial \rho u}{\partial x} + \frac{\partial \rho v}{\partial y} + \frac{\partial \rho w}{\partial z} = 0, \tag{2.4}$$

which states that a convergence of mass will change density (Pedlosky, 1982). The second continuity equation is conservation of heat,

$$\frac{\partial \theta}{\partial t} + u\frac{\partial \theta}{\partial x} + v\frac{\partial \theta}{\partial y} + w\frac{\partial \theta}{\partial z} = K_H \frac{\partial^2 \theta}{\partial x^2} + K_H \frac{\partial^2 \theta}{\partial y^2} + K_V \frac{\partial^2 \theta}{\partial z^2}, \tag{2.5}$$

where θ is a tracer, in this case, temperature, and K_H and K_V are horizontal and vertical molecular diffusivities (which include turbulent effects as above), respectively. Eq. 2.5 describes the change in temperature (first term on LHS) resulting from advection ($\vec{v}\cdot\nabla\theta$) and diffusion of heat (the RHS). There will be a similar equation for conservation of salt. In general form (where θ represents a scalar tracer), Eq. 2.5 describes the time evolution of a scalar concentration field under advection and diffusion. Lastly, there is the equation of state of seawater, which describes the density of ocean water,

$$\rho = \rho(T, S, p) \tag{2.6}$$

where T, S and p are in situ temperature, salinity and pressure, respectively.

2.1.1 Approximations

The primitive equations are derived from the Navier-Stokes equations, which together with conservation of heat and mass and an equation of state, describe real fluid flow. However, in order to implement these governing equations in a finite difference setting involving large spatial and temporal scales, a series of approximations must be made. These simplify the Navier-Stokes and continuity equations into the primitive equations.

The Boussinesq/incompressibility approximation

The density can be described as the sum of the time mean and fluctuating components of density, $\rho(x,y,z,t) = \overline{\rho(x,y,z)} + \rho'(x,y,z,t)$. Then, the Boussinesq approximation assumes that any dynamic density perturbations, ρ', are small in relation to the mean, $\overline{\rho}$,

$$\rho' \ll \overline{\rho}. \tag{2.7}$$

This assumption of incompressibility is used to neglect density variations in Eq. 2.1-2.2 and linearise the momentum equations. With this approximation, conservation of mass (Eq. 2.4) becomes conservation of volume for an incompressible fluid, $\frac{\partial u}{\partial x} + \frac{\partial v}{\partial y} + \frac{\partial w}{\partial z} = 0$ (Pedlosky, 1982). This approximation is implicitly included in order to derive the standard form of the primitive equations, hence these forms of equations (and models that utilise them) cannot be used to solve for sound wave propagation.

The hydrostatic approximation

It follows from the aspect ratio for ocean geometry (depth/horizontal length $\ll 1$) that in general, vertical velocities must be much smaller in magnitude than horizontal velocities. This scaling argument is often used to neglect vertical acceleration and friction, and hence the vertical pressure gradient. Applying the approximation, most terms vanish from Eq. 2.3, leaving only the dominant terms in hydrostatic balance,

$$-\frac{1}{\rho}\frac{\partial p}{\partial z} - g = 0. \tag{2.8}$$

The hydrostatic approximation assumes a balance between the vertical pressure gradient and the buoyancy/gravitational force, i.e. the pressure at depth, z, results from the weight of the water from the surface (η) down to that depth, $p = \int_z^\eta g\rho dz$ (Pedlosky, 1982).

2.2 Grid configuration and boundary conditions

In order to use finite difference methods to solve the primitive equations, the equations must be solved on a discrete framework.

In the horizontal, the primitive equations are discretised over the model grid, which uses orthogonal curvilinear coordinates (options include cartesian, polar and spherical coordinate systems). The type of model grid is called a staggered Arakawa C-grid (Arakawa and Lamb, 1977). This grid locates tracers, density and the free-surface at the centre of the cell (the 'rho-points'), and the horizontal velocities, u and v, on the west/east and north/south cell edges, respectively (Fig. 2.1(a)).

In the vertical, the equations of motion are discretised over topography with a stretched, terrain-following ('sigma' or σ) vertical coordinate. The vertical coordinate thins and stretches between the top of the ocean (which may be below mean sea

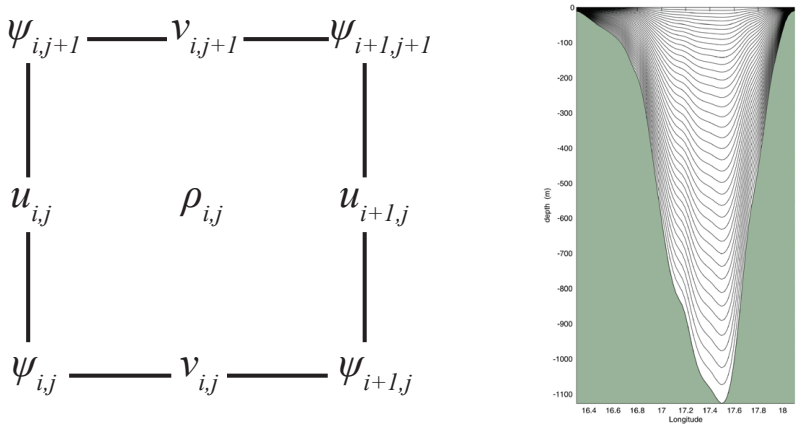

Figure 2.1: (a) ROMS employs the Arakawa-C grid (Arakawa and Lamb, 1977), which evaluates density and tracers in the middle of each cell (marked as ρ), east/west transport on the right/left sides of each cell (marked as u), north/south transport on the north/south faces (marked as v), respectively. The corners of the cell are called the ψ points. (b) An example vertical transect showing spacing of terrain-following vertical layers of the Vieste-Dubrovnik transect. Figure courtesy of ROMS (http://myroms.org).

level due to ice draft) and the bottom topography, and the water column is discretised into the same number of vertical levels for each horizontal location (Fig. 2.1(b)). Terrain-following stretching allows regions of shallow water column to be resolved at high resolution while ensuring regions of deep topography are resolved at computably affordable resolution. Furthermore, the vertical stretching function can be configured to increase resolution at the surface and bottom. This vertical discretisation is thus ideally suited for continental shelf and ice shelf cavity process studies. The vertical staggering of model variables is such that horizontal momentum (u,v,ρ) and tracers are evaluated in the centre of the cell, while the vertical velocity and vertical mixing variables are evaluated at the top and bottom faces of each cell.

2.3 Time-stepping in ROMS

Different types of waves propagate at different speeds, in the open ocean; sound waves are the fastest, $c_s \sim 1500\text{m s}^{-1}$, where c_s is the speed of sound in water, followed by gravity waves which propagate at $\sqrt{gh} \sim 100\text{m s}^{-1}$, where g is the acceleration due to gravity and h is the water depth, internal waves driven by density and buoyancy which propagate at $Nh \sim 5 - 10\text{m s}^{-1}$, where N is the Brunt-Väisälä frequency. The slowest waves are internal currents which typically have velocities $\sim 0.1 - 1\text{m s}^{-1}$. Numerically modelling the full spectrum of ocean waves is difficult due to the large range of characteristic time scales, necessitating a computationally-intensive rapid time step for the fastest waves.

ROMS is a boussinesq model (does not include water compressibility) and so sound waves can not propagate. Therefore, two types of wave propagation with different

characteristic time scales exist - fast gravity waves or barotropic currents, and slow internal waves or baroclinic flow driven by an unstable density-depth gradient.

The solution to the equations of motion can be expressed as the sum of normal modes of oscillation; the zeroth order mode is the depth-averaged solution (barotropic mode), while higher order modes are the baroclinic modes (Gill, 1982). To solve these modes of propagation economically, ROMS uses a 'split-explicit' time-stepping scheme, which splits the numerical solution for the fast (barotropic) and slow (baroclinic) modes of the equations of motion.

This is implemented by solving the depth-integrated equations of motion for the surface elevation an integral number of times (the 'fast or barotropic' time step) for each solution of the full 3-D equations (the 'slow or baroclinic' time step) (Cushman-Roisin and Beckers, 2009). The details of how the timestepping occurs vary between flavours of ROMS, but typically involve standard finite difference techniques (see Shchepetkin and McWilliams, 2009a). For example, Rutgers ROMS employs a predictor-corrector technique to solve the barotropic mode, consisting of a leapfrog method to approximately predict a finite difference solution, followed by a third-order Adams-Moulton corrector to refine the initial prediction and produce an accurate solution (Shchepetkin and McWilliams, 2009b). This algorithm is designed to be robust and stable.

2.4 Parameterisation of ice–ocean thermodynamic interaction

ROMS does not include the influence of ice shelves or ice–ocean interaction by default. Instead, it must be implemented following others (Dinniman et al., 2007; Galton-Fenzi et al., 2012), by assuming an ice shelf in steady state (i.e. melting does not thin the ice shelf), floating in the ocean.

The first adaptation of the ROMS code to account for use with ice shelves is to apply the mechanical pressure exerted by the ice shelf on the water below. By assuming that the ice is in hydrostatic equilibrium, the pressure exerted on the water column below is calculated (for details see Dinniman et al., 2007).

Surface forcing beneath the ice shelf must be adapted. Atmospheric contributions of wind (momentum), evaporation and precipitation (buoyancy) must be removed beneath the ice shelf, while the frictional stress resulting from the ice interface must be included.

We use a quadratic relationship between velocity (U_M; mean velocity within the log layer, where water velocity is described by a simple 'law of the wall') and shear stress at the interface, τ_0, as given by

$$\tau_0 = \rho C_D U_M^2, \tag{2.9}$$

where ρ is the water density and C_D is a non-dimensional quadratic drag coefficient that characterises the roughness of the interface. The shear stress can then be

rewritten in terms of a velocity, defined as the friction velocity, $u_* = \sqrt{\tau_0/\rho}$. The resulting relationship,

$$u_*^2 = C_D U_M^2 \tag{2.10}$$

recasts Eq. 2.9 in terms of the friction velocity and U_M.

Drag at the ice–ocean interface affects boundary layer dynamics, which in turn affects melting, freezing and ocean circulation. In our implementation of ROMS, Eq. 2.10 is used to calculate the surface stress (taking the log layer velocity U_M from the middle of the top model cell), which is then applied to three different model components; melting and freezing is captured in the "3-equation parameterisation" (see below and Appendix A) which are a function of the surface stress (u_* to be precise); the surface stress affects the calculation of vertical mixing across the boundary layer (see Section 3.1.2 where the vertical mixing scheme of Large et al. (1994) is described); and lastly, the surface stress is included when solving the momentum equations (see Section 2.1).

The interaction between the ice shelf and the ocean is also thermodynamic. Water above the in situ freezing point in contact with ice will transfer energy to cause melting, and then become fresher. Alternatively, if the water temperature drops below the in situ freezing point, refreezing can occur. Both of these situations are accounted for with the '3-equation parameterisation' (Holland and Jenkins, 1999). This parameterisation assumes the upper layer of the ocean relaxes towards the in situ freezing point, and the transferral of energy between ice and ocean leads to melting or freezing. The rate at which this energy is transferred is governed firstly, by the rate of diffusion of heat and salt through the oceanic boundary layer (from the ocean interior up to the ice interface), and secondly, by the rate of diffusion of heat through the ice (from the ice interface upwards). The two contributions that have the greatest control on the rate of melting and freezing, are the strength of flow past the interface (the friction velocity, u_*) and the amount of heat available for melting. The heat availability can be described by the thermal forcing, the difference in temperature between the ocean and the in situ freezing point. However, in this thesis, we calculate the thermal driving,

$$T_* = T_M - T_B - a(S_M - S_B), \tag{2.11}$$

as the difference in temperature and salinity between the top model cell (T_M and S_M, respectively) and the interface (T_B and S_B, respectively). Including the difference in salinity accounts for the salt diffusion required in order to bring the interface to the freezing point (Holland and Jenkins, 1999). The details of the three equations that describe the ice–ocean interaction and the implementation of it in ROMS are described in more detail in Appendix A.

Water can become supercooled relative to the in situ freezing point. This can occur, for example, when water is moved to a shallower depth where it is colder than in situ freezing point. In this case, water will directly freeze on to the base of the ice shelf (direct basal refreezing) and, as the water is supercooled, ice crystals (frazil) will form within the water column itself. These crystals will then rise under their own buoyancy until they accrete on the underside of the ice shelf. It is thought

that formation of frazil is a more effective process for quenching/removing supercooling than direct basal refreezing, due to the large difference in surface area over which heat can be transferred (Jenkins and Bombosch, 1995). Studies of marine accreted ice cores show that frazil accretion is often the dominant process of refreezing (Treverrow et al., 2010). Furthermore, frazil formation within the water column will increase plume buoyancy and alter circulation (Jenkins and Bombosch, 1995).

Frazil formation and distribution is implemented as a modification to ROMS (Galton-fenzi, 2009; Galton-Fenzi et al., 2012) by treating frazil concentration as a scalar tracer. Thus, water containing frazil will consist of a homogeneous mixture of ice and seawater with concentration, $\mathcal{C}$. The time evolution of the frazil concentration tracer follows a similar form to Eq. 2.5, but the material derivative is now balanced by a term describing buoyant rising of frazil ($-w\frac{\partial \mathcal{C}}{\partial z}$), a mixing term ($\nabla \cdot (K_{H/V} \nabla \mathcal{C})$) and a source/sink term ($\mathcal{S}$). The source/sink terms, which describe the formation/melting of frazil, are calculated in a similar method to the direct melting and refreezing parameterisation (Galton-Fenzi et al., 2012), but now several crystal size classes (and their respective formation rates) must be accounted for. The seeding of frazil crystals will occur at any model cell which is supercooled, and crystals will rise under their own buoyancy until it reaches the ice shelf base, at which point it contributes to the refreeze rate in that cell.

2.5 Limitations of ROMS for ice shelf cavity modelling

There are some issues which must be considered when applying ROMS to ice shelf cavity modelling.

There must be a rescaling of the vertical coordinate, to stretch between the bottom of the ice shelf (the ice draft) and bathymetry. This will affect the distribution of the terrain-following coordinate, and can lead to a pressure gradient error. This error originates from the coordinate transformation of the horizontal pressure gradient from a vertical coordinate in depth to sigma layers in depth. In regions where the sigma layers vary rapidly horizontally (such as in regions of steep topography), errors may arise in the evaluation of the horizontal pressure gradient and hence artificial flow may arise.

However, pressure gradient algorithms have been designed for ROMS to minimise the influence of this error (Shchepetkin, 2003) and have been shown to be effective at minimising pressure gradient error (Galton-fenzi, 2009). Other methods can be employed to minimise the impact of pressure gradient error, such as reducing the change in ice thickness at the ice front.

Other numerical artefacts can be recognised as not being due to pressure gradient errors, but present as scattered grid cell-scale noise in the computed fields of velocity and hence melt rate (see Section 3.4 and Section 4.3). When the horizontal grid resolution does not adequately resolve the Rossby radius, the numerical solution incorrectly calculates the group velocity of short-scale waves, exciting small-scale perturbations (Adcroft et al., 1999; Losch, 2008). The viscosity scheme employed

will act to dampen this noise, but not completely remove it (which might also remove some of the actual signal). Nevertheless, the presence of this noise is not significant to the main conclusions presented in this thesis.

2.6 Concluding remarks

This chapter has presented a brief overview of numerical ocean models, in particular ROMS, and the equations of motion for fluid flow and the approximations made in order to reduce complexity. The vertical and horizontal discretisation process and the time stepping scheme employed by ROMS are explained. Lastly, the modifications employed to enable ROMS to simulate interaction between ice shelves and the ocean are described.

Chapter 3

BASAL ROUGHNESS CONTROLS MELTING AND FREEZING

Chapter 1 discusses uncertainties in how ice shelves influence the ocean. One such uncertainty is how the roughness on the underside of an ice shelf influences momentum transfer (via turbulence) across the boundary layer, and hence heat supplied to drive melting. To date, a vast majority of ice shelf models employ a quadratic drag coefficient (C_D) to parameterise shear stress across the ice–ocean boundary layer. However, since the choice of C_D will effect melting and freezing, and there is little observational data to constrain the choice of C_D, it remains a significant uncertainty in modelling ice–ocean interaction.

In this chapter, we use an idealised numerical ocean model to explore the effect of the basal friction on melting and freezing beneath ice shelves and sub-ice circulation. These results present a concise summary of how basal friction affects turbulent heat transfer across the boundary layer as well as informing ocean modellers on the effect of the choice of C_D on ice shelf–ocean interaction. These results also motivate the appropriate choice of C_D for refreeze regions (which are likely to be rougher than melting regions), as a higher, more realistic C_D will alter circulation and melting across much of the ice shelf.

The following chapter is sourced from the peer-reviewed article: Gwyther, D. E., Galton-Fenzi, B. K., Dinniman, M. S., Roberts, J. L., and Hunter, J. R. The effect of basal friction on melting and freezing in ice shelf–ocean models. *Ocean Modelling*, 95: 38–52, 2015. doi: 10.1016/j.ocemod.2015.09.004. It has been edited for formatting and the abstract has been removed; the content remains unaltered.

3.1 Ice shelf basal roughness

Ice shelves form around the Antarctic coastline where the ice sheet flows into the ocean. Hydrostatic pressure from the ocean lifts the ice off the bedrock at the 'grounding line', forming an ice shelf and ocean-filled cavity beneath (see Fig. 3.1(a-

b)). The flow of the ice sheet into the ocean is controlled in part by the buttressing effect of ice shelves (Paterson, 2002; Dupont and Alley, 2005). Understanding the dynamics and mass loss from ice shelves is important for projecting future ice sheet flow and Antarctic mass balance (Pritchard et al., 2012).

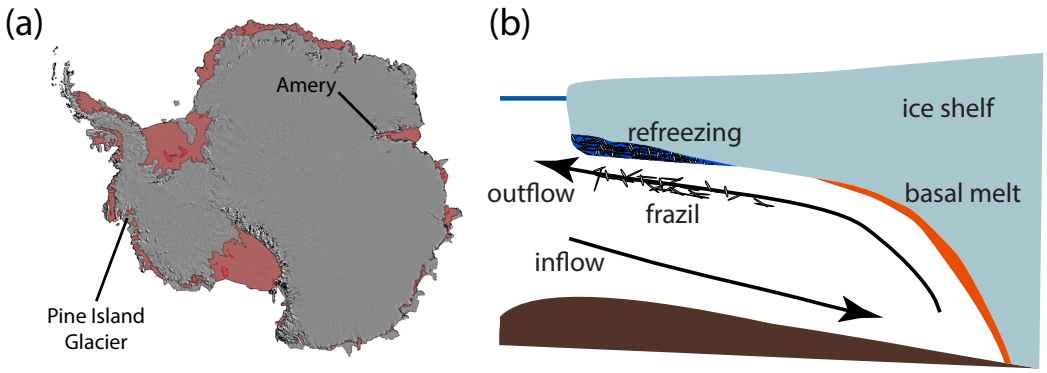

Figure 3.1: (a) Antarctic ice shelves, including Pine Island Glacier Ice Shelf and Amery Ice Shelf, are marked in red on a MODIS MOA basemap (Scambos et al., 2007; Greene et al., 2013). (b) The ice shelf environment is illustrated, showing the grounding line, ocean inflow and outflow, basal melting and refreezing.

Approximately half of the mass loss from the Antarctic Ice Sheet is from basal melting (1454±174 Gt yr^{-1}; Depoorter et al., 2013), where warm (relative to the local pressure freezing point) ocean temperatures drive melting at the base of ice shelves. Increases in the rate of thinning of Antarctic ice shelves attributed to increased basal melting (Pritchard et al., 2012) suggests increased heat delivery to sub-ice shelf cavities. There are several different mechanisms hypothesised to be increasing the delivery of warmer water to ice shelf cavities, including changing wind regimes (Dinniman et al., 2012), polynya and sea ice interactions (Holland et al., 2010; Cougnon et al., 2013; Gwyther et al., 2014), thermocline shoaling (Hattermann et al., 2014) and coastal current redirection (Jacobs et al., 2011; Hellmer et al., 2012). The plethora of different driving mechanisms suggests regionally-varying factors are important for controlling delivery of oceanic heat.

Basal melting at the ice-ocean interface is a function of the ocean circulation and amount of heat within the boundary layer, which can be subdivided into three layers. Direct interaction between the flow and the surface roughness occurs in the viscous sublayer, where molecular viscous forces are dominant ($\mathcal{O}(1)$ cm thick; Soulsby, 1983). This lies within the logarithmic layer (log layer; $\mathcal{O}(1)$ m), where the vertical velocity profile can generally be described with a simple logarithmic relationship or 'law of the wall' (Soulsby, 1983). Together with the outer layer (extending out to $\mathcal{O}(10)$ m; Soulsby, 1983), which is most influenced by the free-stream flow, these comprise the boundary layer. Heat and salt enter the boundary layer from the ocean below and mixing carries heat and salt to the ice interface. Basal roughness controls the turbulent exchange of heat to the ice–ocean interface and changes the thickness of the boundary layer (which affects entrainment and delivery of heat

from below). Basal melting is also a function of hydrostatic pressure (through the pressure dependence of the freezing point temperature), ice shelf basal slope (through the velocity and thickness of the buoyant boundary layer) and driving temperature (Holland et al., 2008).

Using observations of the boundary layer shear profile to determine the coefficient of drag (C_D) has only been accomplished beneath relatively thin sea ice (McPhee et al., 1987; McPhee, 1992) but it is likely that this environment is different from the sub-ice shelf environment. Nevertheless, values of C_D used for the ice shelf–ocean interface in various numerical studies typically range between $C_D = 0.0015$ (e.g. Millgate et al., 2013), $C_D = 0.0025$ (e.g. Hunter, 2006; De Rydt et al., 2014) or $C_D = 0.003$ (e.g. Timmermann, 2002; Dinniman et al., 2007; Klinck and Dinniman, 2010). As C_D is the least observed parameter, it is often tuned to reduce the mismatch between the simulated and observed melt rates (e.g. Jenkins et al., 2010). However, all ice shelf–ocean models to date have used a single C_D for the entire ice–ocean interface, where in reality C_D will vary both spatially and temporally. It is likely that C_D would vary between zones of melting (where ablation of ice would lead to a hydraulically smoother interface and low C_D) and refreezing (high C_D due to the porous and flaky nature of marine-accreted ice (Craven et al., 2009)).

The roughness of the ice shelf-ocean interface affects melting at two different levels; by affecting turbulent flux of heat across the ice shelf-ocean interface (Section 3.1.1), and by changing the shear profile, boundary layer thickness and consequently entrainment of heat into the boundary layer (Section 3.1.2).

3.1.1 Ice–ocean heat flux

The roughness of the ice shelf interface affects basal melting by influencing the transfer of heat (and salt) via turbulence, across the ice shelf-ocean interface, as in Fig. 3.2. Most ocean models use a simple '3-equation parameterisation' of the ice-ocean interface (Hellmer and Olbers, 1989; Scheduikat and Olbers, 1990; Holland and Jenkins, 1999). See Appendix A for details.

In the Holland and Jenkins (1999) parameterisation, T_M and S_M refer to the mixed layer temperature and salinity. Defining a mixed layer of a single density class below the ice shelf interface is appropriate in an isopycnal coordinate model (e.g. Holland and Jenkins, 2001). However, we define the ice shelf–ocean interface in terms of the momentum boundary layer, which is critical for transferring the temperature and salinity properties from the interior cavity to the ice shelf. To implement the parameterisation, it is standard practice to use the values of T and S in the top model cell (e.g. Dansereau et al., 2014). However, as we are able to resolve the outer layer explicitly, T_M and S_M taken from the upper-most model cells are within the log layer, rather than from the outer layer. Therefore models that resolve $\leq \mathcal{O}(1)$ m at the ice shelf–ocean interface may provide different estimates of the gradients of temperature and salinity across the boundary layer and hence, different melt rates. However, a large proportion of the temperature and salinity changes occur over the viscous sublayer, which can lead to relatively well-mixed conditions through the rest

of the boundary layer (Steele et al., 1989). In such cases, the standard practice for implementing the Holland and Jenkins (1999) parameterisation will produce results approximately consistent with observations (Jenkins et al., 2010). The standard practice for implementation of T_M and S_M utilised here is useful for the comparative nature of this study, but does warrant future investigation, particularly as model vertical resolution increases and the top model cell reduces in thickness. Note that we maintain the M subscript for consistency.

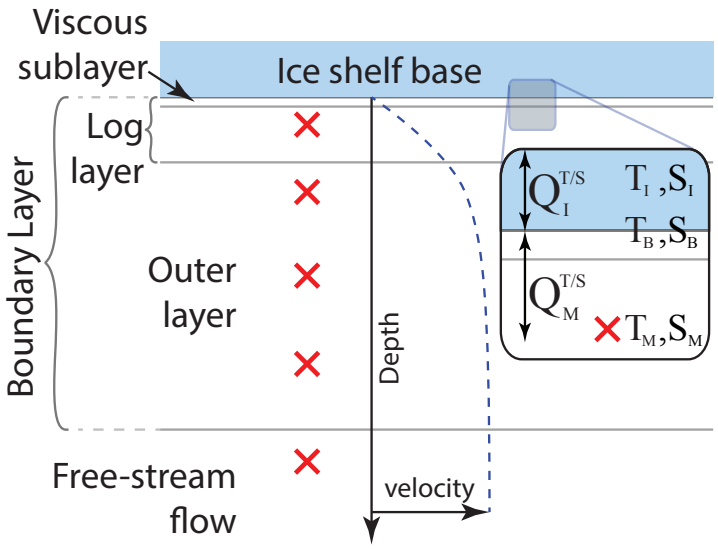

Figure 3.2: The ice shelf–ocean interface is illustrated, with a vertical velocity profile (blue dashed line) and example model grid points (red crosses). Inset shows the ice shelf–ocean interface with temperature (T), salinity (S), heat flux (Q^T) and salt flux (Q^S) shown. Subscripts I, B and M refer to the ice shelf, ice shelf base and ocean model top cell, respectively.

Turbulence is generated by velocity shear through the boundary layer. It is convenient to define the shear stress at the interface in terms of the friction velocity, $\tau_0 = \rho u_*^2$, where ρ is density and u_* is the friction velocity. In these experiments, there is a lower limit on friction velocity, $u_{*,min} = 2 \times 10^{-5}$ m s^{-1}, which is chosen to represent heat transfer by molecular diffusion alone. The presence of turbulence inhibits the direct description of the shear stress and mean flow relationship, and hence we must introduce a parameterisation. We assume a quadratic relationship between shear stress and mean flow, $\tau_0 = \rho C_D U_M^2$, where U_M is the mean flow in the boundary layer, yielding a relationship between the mean boundary layer flow and the friction velocity,

$$u_* = \sqrt{C_D}|U_M|, \tag{3.1}$$

where C_D is a nondimensional drag coefficient. Note that since this is a parameterisation of the non-resolved layers between the top model grid point and the interface, it is understood to have an implicit depth dependence. It follows that changes in vertical resolution will impact the choice of C_D in ocean models.

The three coupled thermodynamic equations (Eqs. A.1-A.3) govern the thermal regime of the boundary layer and can be simultaneously solved, yielding the melt rate at the ice shelf base, m, and the temperature and salinity of the seawater in contact with the base of the ice, T_B and S_B, respectively. An expression for m is given by rearranging Eq. A.2 and substituting the expression for the latent heat flux and heat conduction into the ice,

$$m = -\frac{c_{p,M}}{L_f}\gamma_T(T_B - T_M) + \frac{\rho_I}{\rho_M L_f}\alpha_I^T \left.\frac{\partial T_I}{\partial z}\right|_B . \tag{3.2}$$

The first term on the right hand side of Eq. 3.2 is the melting due to the thermal forcing (difference between the interface temperature, T_B and the log layer temperature, T_M) and the thermal exchange velocity γ_T (which is a function of u_*), where $c_{p,M}$ is the log layer specific heat capacity, and L_f is the latent heat of fusion. The second term on the RHS is a reduction of melting due to heat conduction into the ice shelf, where ρ_I is the mean ice density, ρ_M is the log layer density, α_I^T is the thermal diffusivity of ice and $\left.\frac{\partial T_I}{\partial z}\right|_B$ is the ice shelf vertical temperature gradient evaluated at the base of the ice shelf. There is an analogous equation for melt rate derived from the salt balance at the ice–ocean interface, which depends on the salt exchange velocity (γ_S; also a function of u_*) and the salinity difference at the interface, obtained by rearranging Eq. A.3. Note that throughout this thesis, the exchange velocities, γ_T and γ_S are referred to as $\gamma_{T/S}$ for brevity.

In the implementation of the three equation parameterisation, both of these equations are utilised to solve for m, and as such, it is a function of both the temperature and salinity difference from the interface to the log layer (defined as the thermal driving, T_*). As the heat conduction term of Eq. 3.2 is small compared to the melting, then we see that m is primarily dependent on the exchange velocities (which are a function of circulation and roughness) and the thermal driving. In the model, heat conduction into the ice is captured with a vertical diffusion and advection scheme (see Holland and Jenkins, 1999) which modifies melting and freezing at the ice shelf–ocean interface.

3.1.2 Friction-driven turbulent mixing

Turbulent mixing of interior waters into the boundary layer is controlled by the friction velocity, u_*, which impacts both the mixing and entrainment rate of heat and salt and thickness of the boundary layer (see Fig. 3.2). Consequently, C_D (see Eq. 3.1) affects the mixing of heat into the boundary layer, and thus changes the thermal driving of the melting and freezing.

Vertical mixing in this study is simulated using the scheme outlined in Large et al. (1994), hereinafter referred to as LMD94. LMD94 splits mixing into interior oceanic mixing (comprised of vertical diffusivities resulting from shear instability, internal wave mixing and double diffusivity) and boundary layer mixing. LMD94 parameterise boundary layer mixing with a vertical profile of eddy diffusivity, K_x (where x represents momentum, salinity or temperature). The eddy diffusivity is used to

calculate the kinematic flux (transport of a variable per unit time), $-K_x \frac{\partial X}{\partial z}$, where z is the upward vertical coordinate, and X is the time average of property x. Importantly, the eddy diffusivity and thus vertical flux, scales with the thickness of the boundary layer, h, via $K_x(\sigma) = hw_x(\sigma)G(\sigma)$, where $\sigma = d/h$ is a dimensionless vertical coordinate (varying from 0 to 1) indicating fractional position in the boundary layer, $G(\sigma)$ is a nondimensional cubic polynomial 'shape function', $w_x(\sigma)$ is the turbulent velocity scale and d is the distance coordinate from the ice-ocean boundary.

Boundary layer thickness in LMD94 depends on the surface forcing (beneath an ice shelf the forcing is due to momentum stress from basal roughness and a buoyancy flux of salt and heat due to melting or freezing) and is estimated with a bulk Richardson number ($Ri_b(d)$) describing the ratio of the stabilising effect of buoyant stratification (buoyancy profile is $B(d)$) to the destabilising effect of velocity shear (shear profile is $\vec{v}(d)$),

$$Ri_b(d) = \frac{(B_r - B(d))d}{|\vec{V}_r - \vec{V}(d)|^2 + \vec{V}_t^2(d)}. \tag{3.3}$$

Here, $\vec{V}_r$ and B_r are the average velocity and buoyancy where Monin-Obukhov similarity theory applies (assumed to be ~ 0.1 of the boundary layer thickness), while $\vec{V}_t(d)$ is the turbulent velocity profile. The boundary layer thickness is equated to the smallest value of d such that $Ri_b(d) = Ri_c$, where $Ri_c = 0.3$ is a critical Richardson number. Physically, eddies (with buoyancy and velocity corresponding to conditions at the viscous sublayer) will only be able to intrude to a depth of h, at which point they will become stable relative to the local buoyancy and velocity. As a result, a thicker boundary layer will be able to contain larger eddies and hence more energetic eddy mixing. Consequently, as basal roughness (and circulation) controls the velocity shear profile across the boundary layer, so the boundary layer thickness will increase with increasing C_D.

3.1.3 Geophysical considerations

The ice shelf cavity environment commonly falls into one of two classifications; 'cold cavity' and 'hot cavity', referring to the relative characteristics of the inflow water (Joughin et al., 2012). A 'cold cavity' scenario occurs where relatively cold water, often produced during sea ice formation (for example High Salinity Shelf Water (HSSW) with a temperature of ~ -1.9°C and salinity of 34.7 on the Practical Salinity Scale), enters the ice shelf cavity, resulting in low melt rates (typically an area average below ~ 1 m yr^{-1}). A typical example is the Amery Ice Shelf cavity, thought to be dominated primarily by HSSW (Galton-Fenzi et al., 2012) and Ice Shelf Water below the surface freezing point (Herraiz-Borreguero et al., 2013). In this environment, melting is weak (typically 0.74 m ice yr^{-1}; Galton-Fenzi et al., 2012). As the sub-ice shelf water temperature in these environments is relatively cold, the injection of cold meltwater can result in supercooling below the in situ freezing point and frazil crystal formation with significant refreezing regions. Furthermore, the 'ice pump' mechanism, whereby deep melting leads to a buoyant

meltwater plume rising along the ice shelf base and (due to the pressure dependence of the freezing point of seawater) refreezing at a shallower point along the base (Lewis and Perkin, 1986), is strong in this situation. In contrast, the 'hot cavity' has relatively warm and saline inflow waters and higher melting such as for Pine Island Glacier Ice Shelf. In this example, Circumpolar Deep Water (at temperatures $> 0.5°$C and salinity of 34.6; $> 3.5°$C above the in situ freezing point) enters the ice shelf cavity, leading to strong melting. Hydrography-based estimates of melt rate are $22 - 33$ m yr^{-1}(Jacobs et al., 2011), while glaciological estimates are 47 m yr^{-1} over the inner 1005 km^2 of the ice shelf and 84 m yr^{-1} closer to the grounding line (Warner and Roberts, 2013). In this situation, the warm environment diminishes the role of refreezing in the 'ice pump', but strengthens the buoyancy-driven circulation. The importance of these cavity environments for driving melt rate, the regional differences, and the generally unexplored nature of the fundamentals of ice shelf–ocean interaction motivate the study of the details of both environments.

3.1.4 Study scope

This study comprises numerical simulations investigating:

- the effect of C_D on the melt/freeze rate, circulation and oceanic boundary layer properties,
- the relative importance of C_D on driving heat flux into the ice interface and on mixing heat into the boundary layer,
- the effect of spatially- and temporally-varying C_D on melt/freeze, circulation and oceanic boundary layer properties, compared to a commonly chosen constant basal roughness value.

We provide an overview of the role of basal roughness in modifying and controlling melting and freezing in an ice shelf–ocean model containing either hot or cold cavities and inform the choice of C_D in the parameterisation of the ice–ocean interface and boundary layer environment. We show the need to include a realistic, spatially-varying basal roughness parameter in future ice shelf–ocean models.

3.2 Model setup

A modified version of the Regional Ocean Modeling System (ROMS; Shchepetkin and McWilliams, 2005), a 3-D primitive equation finite difference ocean model, was used to simulate ice shelf–ocean interaction. The modifications include the addition of thermodynamic interaction between ocean and the ice shelf (see Dinniman et al., 2007; Galton-Fenzi et al., 2012). ROMS has been shown to be able to handle the steep change in water column thickness at the ice shelf front through many ice shelf–ocean modelling studies (Dinniman et al., 2007; Galton-fenzi, 2009; Galton-Fenzi et al., 2012; Mueller et al., 2012; Cougnon et al., 2013; St-Laurent et al., 2013; Gwyther et al., 2014, and others).

The model domain is designed to simulate an ice shelf and extends from 0°E to 15°E, 70°S to 80°S, with a linearly southward downsloping ice draft (starting at 200 m at 76°S and deepening to 700 m at 80°S), and a flat bathymetry (900 m). The geometry shown in Fig. 3.3 is the Ice Shelf–Ocean Model Intercomparison Project (ISOMIP) geometry 2 (Hunter, 2006). We chose a linearly sloping ice draft as it is the standard geometry for investigating idealised ice shelf–ocean interaction. Using this ice shelf geometry allows intercomparison with recent studies that also employ the same ice shelf geometry (Dansereau et al., 2014). Furthermore, Holland et al. (2008) found a non-linear ice shelf shape produces weaker melting on average, but has the same quadratic relationship between melting and thermal driving as a linearly sloping ice shelf draft. While Little et al. (2009) found a departure from this quadratic dependence of melt rate on thermal driving with different ice shelf geometries, all of their geometries showed a common super-linear response to increasing ocean temperature. As we are more interested in the melt relationships rather than the magnitude of melting, the results of this study should be applicable across more complex geometries.

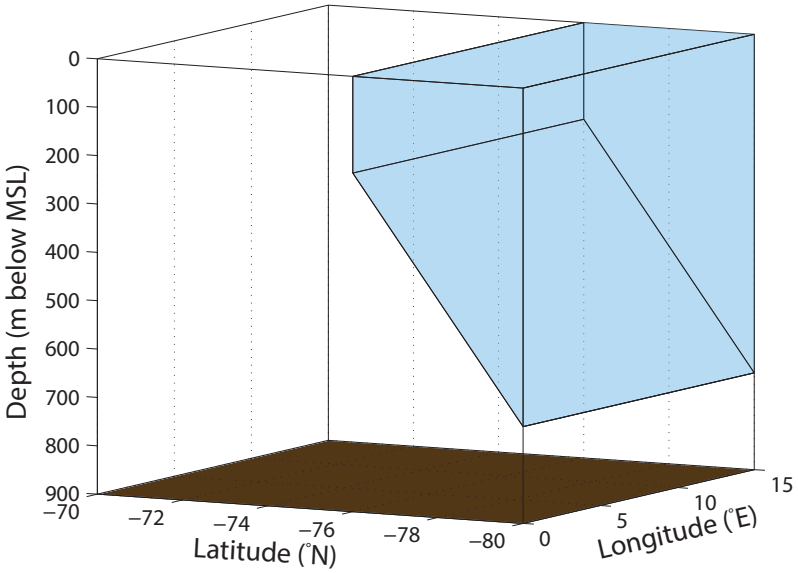

Figure 3.3: Model geometry is shown from an oblique perspective, indicating the bottom bathymetry (brown) at 900 m below the surface, and ice surface (pale blue) linearly sloping down to 700 m with a 200 m thick ice front at 76°S.

The model is initialised with water of temperature -1.9°C and salinity of 34.4, following ISOMIP. The model has horizontal grid resolution of approximately 0.3° in the zonal direction and 0.1° in the meridional direction. ROMS uses a terrain-following vertical coordinate and the 24 vertical levels have an approximately sigmoidal distribution of vertical position, enhancing vertical resolution near the upper and lower surfaces. Cell thicknesses for the upper and lowest cell are $\sim$ 0.007 and $\sim$ 0.02 of the water column thickness respectively, and ~ 0.078 of the water column thickness at mid-column depth. Thus, the centre of the top cell is ~ 2 m from the bottom of

the ice at the ice front, and ~ 0.7 m from the bottom of the ice at the back of the cavity. The model is run for 30 years to approximate steady state, and the last year of output is averaged and used for analysis.

This experiment is designed to investigate ice shelf–ocean interaction in an idealised scenario by removing the obfuscating interaction of winds and inflowing ocean currents with sub-cavity water. As a result, circulation is controlled by the buoyancy forcing resulting from ice–ocean thermodynamics and the difference in buoyancy of the open ocean and sub-ice shelf environments. This is similar to previous ISOMIP-like experiments (Holland et al., 2008; Losch, 2008), where there are no forced inflow currents.

The lateral boundaries are treated as closed, leading to no heat or salt flow into the domain across any lateral boundary. Oceanic conditions within the model domain are restored through daily relaxation of the open ocean surface to constant temperature and salinity values. The surface forcing conditions are chosen to produce oceanic conditions within the ice shelf cavity similar to physical examples. For the cold cavity scenario, similar to Amery Ice Shelf, the open ocean surface is relaxed to -1.9°C and salinity of 34.5. The hot cavity scenario, similar to the Pine Island Glacier ice shelf cavity, is simulated by relaxing the open ocean surface temperature to 0.5°C and salinity to 34.6. Note that melt rates simulated in this environment will not be as high as if there was flow across the lateral boundaries.

Melting and freezing at the ice shelf–ocean interface (within the viscous sublayer) is simulated with the above mentioned three-equation parameterisation (Holland and Jenkins, 1999). Excepting the velocity-independent sensitivity studies (see Section 3.4.2), we employ velocity-dependent turbulent transfer velocities, which is important for capturing fluctuations in turbulence resulting from changes in flow (Jenkins et al., 2010). Mixing of heat and salt into the boundary layer from the ocean below is simulated with an eddy diffusivity parameterisation (Large et al., 1994). Both of these parameterisations have dependence on the drag coefficient, C_D.

3.3 Experiments

This study is split up into three sets of experiments as follows, 1) spatially constant drag, 2) investigating the role of friction-driven turbulent mixing, and 3) spatially and temporally variable drag, which are discussed in turn.

3.3.1 Spatially constant drag

The first set of experiments investigate approximate steady state melting/freezing at the ice interface for a spatially constant C_D. The result is a suite of simulations over the range from smooth ice ($C_D = 0.0005$) through to rough ice ($C_D = 0.1$). Ten different values of C_D (Table 3.1) are repeated for two different forcing conditions; a cold cavity and hot cavity environment.

	C_D		FDTM	$\gamma_{T/S}(u_*)$	Simulation name
Section 3.3.1	0.0005		✓	✓	case a
	0.00075		✓	✓	
	0.001		✓	✓	
	0.003		✓	✓	
	0.005		✓	✓	
	0.006		✓	✓	
	0.009		✓	✓	
	0.01		✓	✓	
	0.05		✓	✓	case a (hot)
	0.1		✓	✓	case a (cold)
Section 3.3.2	0.0005		×	✓	case b
	0.0005		✓	×	case c
	0.0005		×	×	case d
	0.1 (cold), 0.05 (hot)		×	✓	case b
	0.05		✓	×	case c
	0.05		×	×	case d
Sec. 3.3.3	$C_{D,melt}$	$C_{D,freeze}$	FDTM	$\gamma_{T/S}(u_*)$	
	0.003	0.01	✓	✓	
	0.003	0.1	✓	✓	

Table 3.1: Summary of experiments showing the range of drag values and experiment conditions tested, such as whether $\gamma_{T/S}$ was a function of u_* (signified by a ✓) or was constant (×) and whether friction-driven turbulent mixing (FDTM) into the boundary layer was included (✓) or switched-off (×). Experiments in Section 3.3.1 are run with velocity-dependent $\gamma_{T/S}$ and with friction-driven turbulent mixing. Experiments in Section 3.3.1 and Section 3.3.2 are repeated for both hot and cold cavity conditions, while Section 3.3.3 is run only under a cold cavity environment. The names of the control simulation run in Section 3.3.1 and the sensitivity simulations run in Section 3.3.2 are shown in the last column. Note the different C_D chosen for the cold and hot cavity sensitivity experiments in Section 3.3.2, and the control cases the results are compared against in Section 3.3.1.

3.3.2 Velocity dependence/independence and friction-driven turbulence

Melting and freezing is dependent not only on u_* driving heat flow across the ice interface, but also the heat supply into the boundary layer. The friction-driven turbulent mixing of heat (a function of u_*) into the boundary layer drives the boundary layer temperature and salinity and therefore, thermal driving. This set of experiments will examine the melt dependence due to each contribution by examining four melt/freeze and boundary layer parametrisation cases, as follows,

(a) with velocity-dependent melting and friction-driven turbulent mixing

(b) with velocity-dependent melting and without friction-driven turbulent mixing

(c) without velocity-dependent melting and with friction-driven turbulent mixing

(d) without velocity-dependent melting and without friction-driven turbulent mixing

The control run (case a) has both friction-driven turbulent mixing simulated through the boundary layer parameterisation; and turbulent heat and salt exchange velocities, $\gamma_{T/S}$, that vary as a function of C_D and u_*. Case (a) are those experiments done for Section 3.3.1. The first sensitivity study (case b) has the friction-driven mixing into the boundary layer switched-off, while $\gamma_{T/S}$ still varies as a function of u_*. The second sensitivity study (case c) has friction-driven mixing into the boundary layer simulated, but $\gamma_{T/S}$ are set to spatially constant values and not allowed to vary as a function of u_*, hence simulating velocity-independent melting. This is a similar experiment to that performed by Dansereau et al. (2014). The third sensitivity study (case d) has constant $\gamma_{T/S}$ and no friction-driven turbulent mixing.

Friction-driven turbulent mixing is nullified by turning off the u_* dependence in the LMD scheme, while the velocity-dependence in the calculation of melting and freezing is controlled by setting transfer coefficients $\gamma_{T/S}$ to constant values within the ice shelf thermodynamics code. The velocity-independent $\gamma_{T/S}$ values used in the case (c) experiments are determined by calculating the area-average $\gamma_{T/S}$ for the case (b) scenario with the same C_D. In this way, the exchange coefficients in the case (a) and case (b) simulations will be broadly similar, allowing exploration of the effect on the melt rate due to removing friction-driven turbulent mixing or spatial variation in $\gamma_{T/S}$.

We will then repeat these 3 cases for a low drag and high drag interface, and for a cold cavity and hot cavity scenario, leading to 12 model runs in total (Table 3.1).

3.3.3 Spatially- and temporally-varying drag

This set of experiments test the effect of spatially- and temporally-varying drag. This is achieved using a dynamic drag that varies spatially and temporally, depending on whether there is melting or freezing at the ice shelf–ocean interface

(Table 3.1). For a cell that is melting, $C_D = 0.003$, to simulate the smooth ice interface while for a cell that is freezing, C_D is set to 0.01 or 0.1 to simulate rough marine ice. This 'dynamic drag' will be tested by running a simulation with melt/freeze dependent C_D until pseudo-steady state is achieved (30 years). The resultant melt rates at pseudo-steady state are compared to simulations with a spatially-constant drag appropriate for melting ($C_D = 0.003$), as in Section 3.3.1.

3.4 Results

3.4.1 Constant drag

In this section, we investigate the effect that the basal roughness parameter has on melting and oceanic boundary layer properties through the most common parameterisation of ice shelf–ocean interaction (Holland and Jenkins, 1999). Strong westwards flow and melting exists along the ice shelf front. For Fig. 3.5-3.8, the averaged value is calculated with (red) and without (black) the line of cells along the ice front. For this investigation, the dynamics over the majority of the ice shelf area are more important than that along the thin ice shelf front. Consequently, the reader should refer to the black markers, however the results including the ice front are included for completeness.

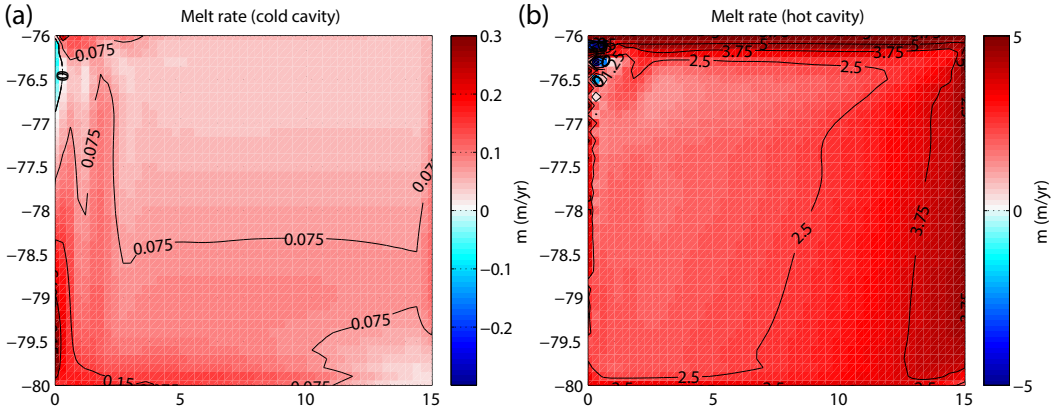

Figure 3.4: Melt rate (positive for melting; negative for freezing) shown for (a) cold cavity, and (b) hot cavity environments. Both model runs use a commonly-used $C_D = 0.003$. Both ice shelves display melting over much of the ice shelf–ocean interface, while the refreezing area is much larger in the cold cavity.

In a hot cavity with a commonly-used coefficient of drag ($C_D = 0.003$), melting occurs over the vast majority of the ice shelf area (Fig. 3.4); the eastern region of the ice shelf supports high melt rates as ocean water enters rapidly; melting is present but weaker for the rest of the ice shelf; excepting the deep south-eastern region where melting is driven by a large temperature differential (between inflowing water and the pressure melting point). The presence of melting over most of the ice shelf area results in large quantities of cold meltwater production which flows north-

westwards under Coriolis and buoyancy forces. The north-western boundary is a refreeze zone, created by cold meltwater ascending to where it is below the pressure dependent in situ freezing point and thus refreezing. The outflow region is also characterised by strong buoyancy-driven velocities enhancing rates of freezing. The pattern of refreezing along the western side of the ice shelf, where cold meltwater outflow is concentrated, has been observed on Antarctic ice shelves (e.g. Fricker et al., 2001). While refreezing occurs in the hot cavity simulations, we note that it occurs over a very small area. Furthermore, in the idealised hot cavity simulations, the buoyant melt water plume has a long distance over which to lose heat to the ice shelf. In reality, hot cavity ice shelves, which are smaller than that simulated here, may not exhibit refreezing.

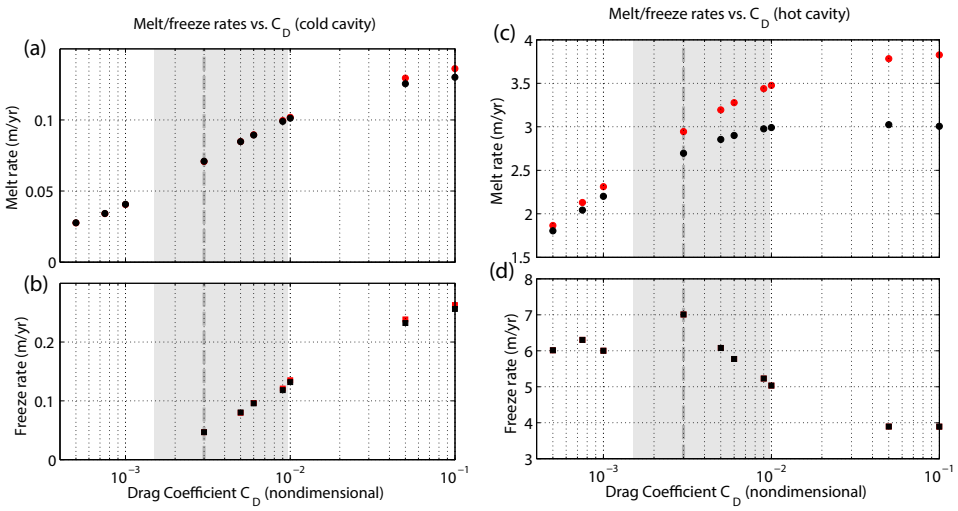

Figure 3.5: Area averaged (a) melting and (b) freezing for the cold cavity environment and area averaged (c) melting and (d) freezing in the hot cavity environment are shown plotted against the drag coefficient beneath the ice shelf. The average melt and freeze rates are calculated only over the regions of melting and freezing, respectively. Black markers represent averages with the ice shelf front neglected from the average, while red markers include the ice front. Included is a shaded band indicating the range of C_D from literature and a commonly used value $C_D = 0.003$.

In Fig. 3.5, the area-averaged melt/freeze rate, calculated from a temporal average of the last year of the model run, is shown as a function of the ice shelf–ocean interface drag coefficient. The area-average melt/freeze rate (positive for melting; negative for freezing) is calculated only across the area experiencing melting and freezing respectively. This allows properties of the ice shelf–ocean interaction to be investigated for both the melting and freezing areas separately, which is more important for the cold cavity scenario, where the area of refreezing is significant (Fig. 3.4(a)).

As expected, the cold cavity scenario, with colder and less saline surface forcing, leads to lower area averaged melt rates than the hot cavity environment (compare Fig. 3.5(a) to Fig. 3.5(c)). Melt increases monotonically with C_D, and begins to

flatten as C_D increases to high values. Refreezing, which only occurs at moderate to high C_D, increases in magnitude as C_D increases in Fig. 3.5(b).

Results from the hot cavity scenario, where surface forcing is warmer and more saline, are shown in Fig. 3.5(c - d). Melt rates are much higher than the cold cavity scenario; there is more melting at the ice front; and, melting reaches a peak value at lower C_D. Melting is weak for the lowest drag ($C_D < 1 \times 10^{-3}$), increases to a local maximum at moderate to high drag ($C_D = 1 \times 10^{-2}$), then plateaus above $C_D = 5 \times 10^{-2}$. Melting decreases marginally between $C_D = 5 \times 10^{-2}$ and $C_D = 1 \times 10^{-1}$.

Refreezing in the hot cavity scenario is present in these idealised simulations, as shown in Fig. 3.5(d). The freezing in these scenarios is higher in magnitude than in the cold cavity scenario, but shows a tendency to fluctuate in magnitude between different C_D. This is likely due to refreezing occurring over a small proportion of ice shelf area (0.2% for the lowest C_D tested increasing to 0.45% at the highest C_D tested; 4 to 8 model cells), making it more susceptible to noise as cells switch from freezing to melting. In the cold cavity, refreezing occurs over a larger area and hence monotonically increases in magnitude.

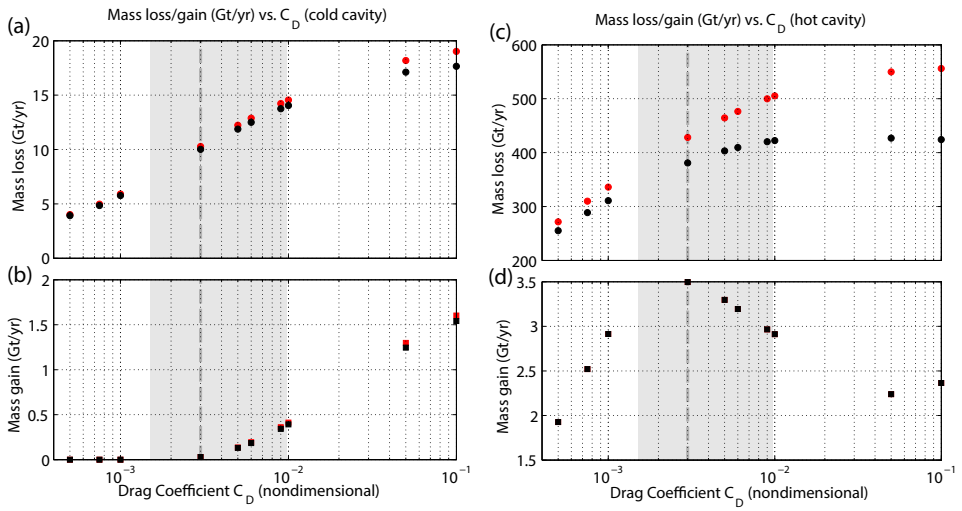

Figure 3.6: The annual (a and c) mass loss and (b and d) mass gain are calculated for the areas displaying melting and freezing, respectively. This is calculated for both the (a and b) cold cavity conditions and (c and d) hot cavity conditions. Black markers represent averages with the ice shelf front neglected from the average, while red markers include the ice front. Shaded band indicates range of C_D from literature and vertical line is $C_D = 0.003$.

The melting and freezing weighted by the area of each process is shown by considering the integrated mass loss, calculated as $\Delta M = \rho_{ice} \int m(A) \cdot \, dA$, where m is the melt rate, A is the area of melting/freezing, ρ_{ice} is the density of ice, shown plotted for different C_D in Fig. 3.6. In each case, the trend in mass loss/gain is the same as the melt/freeze rate but the scaling by the area of each process weights the processes and allows them to be compared.

In the cold cavity scenario, Fig. 3.6(a - b), mass loss increases with increasing C_D. Mass gain through refreezing is a low proportion of mass loss ($1-10\%$), though it increases for increasing C_D. The mass loss in the hot cavity scenario (Fig. 3.6(c)) follows the same trend as the hot cavity melt rate, increasing with increasing C_D before plateauing for moderate to high C_D. The mass gain through freezing is a tiny fraction of the mass loss ($< 1\%$), showing that the high average freeze rate in Fig. 3.5(d) should be treated as a small contribution to the thermodynamic interaction in the hot cavity environment. Furthermore, the cold cavity mass loss is approximately $1-4\%$ of the hot cavity mass loss while the cold cavity mass gain is approximately $7-17\%$ of the hot cavity mass gain for moderate drag, increasing to $55-63\%$ for high drag.

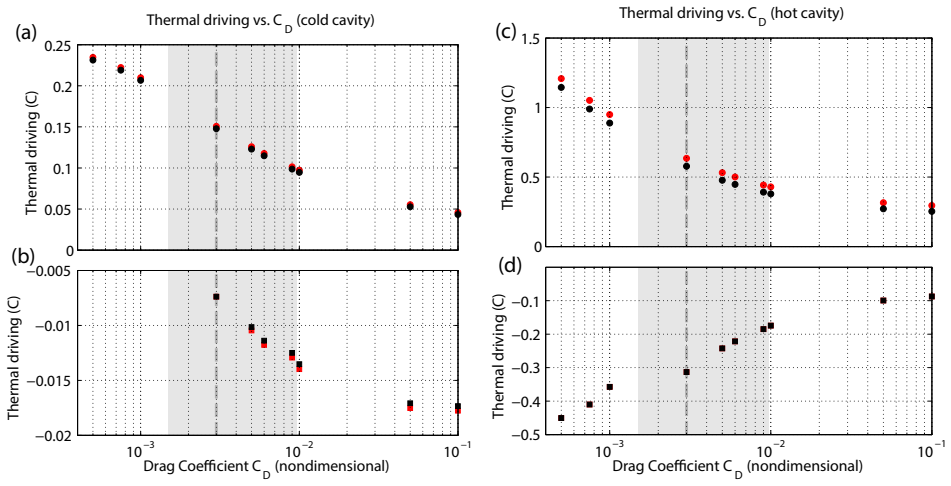

Figure 3.7: The area-averaged thermal driving, $T_* = T_M - T_B - a(S_M - S_B)$ for the (a and c) melting and (b and d) freezing regions, for different basal roughness. This is shown for both the (a and b) cold cavity and (c and d) hot cavity conditions. Black markers represent averages with the ice shelf front neglected from the average, while red markers include the ice front. Shaded band indicates range of C_D from literature and vertical line is $C_D = 0.003$.

The thermal driving across the ice shelf–ocean interface is calculated as $T_* = T_M - T_B - a(S_M - S_B)$, which accounts for a temperature and salinity difference from the top model cell to the interface. Here, a is the salinity coefficient of the linearised freezing equation (see Eq. A.1). A positive thermal driving indicates heat available for melting, while a negative thermal driving indicates supercooling and the potential for refreezing.

For the cold cavity, thermal driving is low for the melting region, and decreasing for increasing C_D (Fig. 3.7(a)). In the refreeze zone, the thermal driving is negative and is increasing in magnitude as C_D is increased as (Fig. 3.7(b)). The thermal driving in the hot cavity is significantly stronger than the cold cavity ($T_* \approx 1°$C for low drag) and decreases with increasing C_D. In the refreeze zone, thermal driving is negative, and in contrast to the cold cavity refreeze zone, decreases with increasing C_D. The

maximum magnitude of negative thermal driving in the refreeze zone is much higher ($T_* = -0.45°\text{C}$) and occurs at the lowest C_D, compared to the maximum magnitude of thermal driving in the cold cavity scenario ($T_* = -0.0018°\text{C}$), which occurs at the highest C_D. Note that in reality, the degree of supercooling observed in the hot cavity at low drag would be quenched by the formation of frazil crystals within the water column, which is an effect not included in these model runs. The behaviour of T_* with C_D for the refreezing areas, is increasing in magnitude for the cold cavity and decreasing in magnitude for the hot cavity. This inversion, visible in the freeze rate behaviour of the refreezing zones, is discussed in Section 3.5.1.

Velocity near the ice shelf–ocean interface is investigated with top layer velocity magnitude $|U_M|$ and friction velocity u_* (Fig. 3.8). These have complementary but different uses for diagnosing how velocity affects melting; u_* feeds directly into the three equation parameterisation, so understanding this is important for understanding the thermodynamics of the three-equation parameterisation; and, $|U_M|$ is the physical realisation of flow across the ice face and as a result shows the effect of drag.

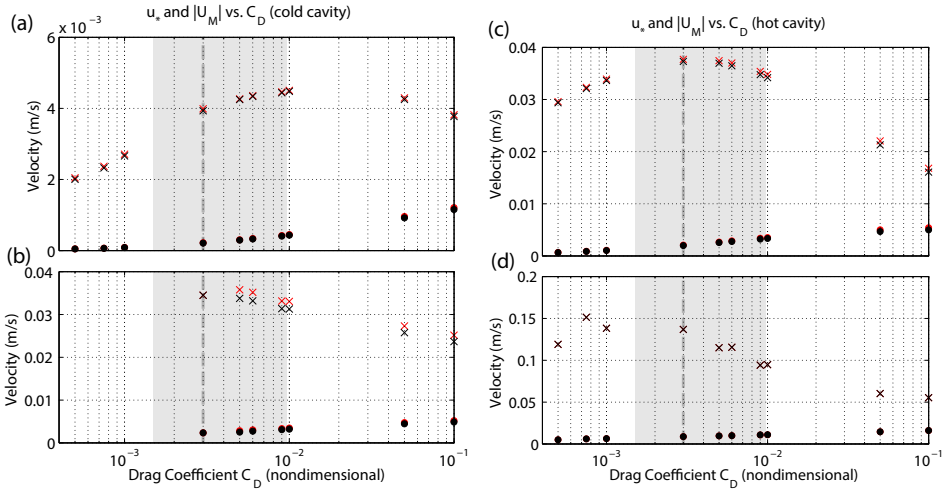

Figure 3.8: The area-average boundary layer velocity magnitude ($|U_M|$; crosses) and the area-average friction velocity (u_*; circles) are plotted. The area-average velocity magnitude is calculated from the model layers which fall within the surface boundary layer as calculated by the surface mixing parameterisation. This is shown for the (a and c) melt regions and the (b and d) freeze regions and was calculated for (a and b) cold cavity and (c and d) hot cavity conditions. Black markers represent averages with the ice shelf front neglected from the average, while red markers include the ice front. Shaded band indicates range of C_D from literature and vertical line is $C_D = 0.003$.

For a cold cavity, the boundary layer velocity magnitude ($|U_M|$; Fig. 3.8(a)) increases for increasing C_D, except at high C_D, where there is a decrease in $|U_M|$ for the melt region after peaking at $C_D \sim 2 \times 10^{-2}$. The area-averaged friction velocity, u_* displays increasing magnitude with increasing C_D for both the melting and freezing

regions.

The hot cavity scenario displays similar behaviour to the cold cavity scenario, but u_* and $|U_M|$ are now an order of magnitude higher. The maximum $|U_M|$ occurs in the hot cavity scenario at lower drag ($C_D = 0.003$) than in the cold cavity scenario ($C_D \approx 0.01$).

3.4.2 Friction-driven turbulence and velocity dependent/independent melting

Here, the contribution to the melt rate from the impact of C_D on both the heat flux into the ice and by driving mixing into the boundary layer is investigated by selectively turning off these effects. Note that since holding $\gamma_{T/S}$ constant is a much larger effect than removing friction-driven turbulent mixing, results of case (c) and case (d) are similar and thus we do not show the results of case (d). We also found the hot environment, high drag simulations run without friction-driven turbulent mixing were subject to instabilities above $C_D = 0.05$. Hence, the high drag sensitivity studies use $C_D = 0.1$ for the cold cavity and $C_D = 0.05$ for the hot cavity.

Fig. 3.9 shows results of the first sensitivity study (case b), which investigated the effect of removing friction-driven turbulent mixing. Fig. 3.9(a, c, e, g) show the spatial distribution of melting and freezing (m yr^{-1}), while Fig. 3.9(b, d, f, h) show the melt quotient (melt rate of the sensitivity study divided by the melt rate of the control run; nondimensional). Fig. 3.9(a - d) show the low drag interface ($C_D = 0.0005$), while Fig. 3.9(e - h) show the results of the high drag interface ($C_D = 0.1$ for Fig. 3.9(e and f); $C_D = 0.05$ for Fig. 3.9(g and h)). The first two rows (Fig. 3.9(a, b, e, f) are for the cold cavity, and the third and fourth rows (Fig. 3.9(c, d, g, h) are for the hot cavity.

For the low drag ($C_D = 0.0005$), cold cavity runs (Fig. 3.9(a and b)), the effect of no frictional mixing is a minor ($< 5\%$) decrease in melt across the front half of the ice shelf except along the shallow ice front region where melting is marginally increased ($< 5\%$).

In the high drag ($C_D = 0.1$), cold cavity runs (Fig. 3.9(e and f)), ignoring frictional mixing leads to strengthened refreezing, increased melting in the vicinity of the edge of the refreeze zone, and a widespread marginal decrease in melting.

In the low drag ($C_D = 0.0005$), hot cavity runs (Fig. 3.9(c and d)), the effect of the increased thermal driving is visible as relatively high melt rates (note the different colour scale between plotted melt rates), and a contracted refreeze zone, which consists of only a small number of cells. The effect of no frictional mixing is a widespread but weak decrease in melting.

In the high drag ($C_D = 0.05$), hot cavity sensitivity runs (Fig. 3.9(g and h)), the effect of no frictional mixing is strongly reduced melting along the western boundary, an adjacent band of strengthened melting and a widespread but weak decrease in melting.

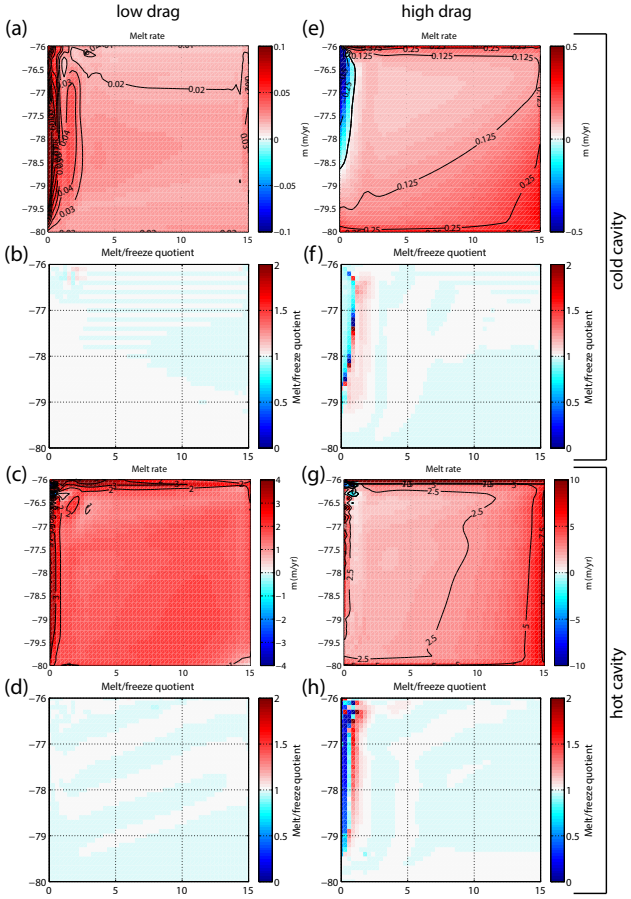

Figure 3.9: Melt rate (a, c, e and g; m) plotted for the control run (with friction-driven turbulent mixing), and fractional change in melt rate (b, d, f and h; $m_{noFDTM}/m_{withFDTM}$) plotted for the sensitivity studies without friction-driven turbulent mixing. (a - d) are low drag ($C_D = 0.0005$) and (e - h) are high drag ($C_D = 0.1$ for (e and f); $C_D = 0.05$ for (g and h)). Panels (a and b) and (e and f) are cold cavity environments, while (c and d) and (g and h) are hot cavity environments. Changes in sign (e.g. freezing changing to melting) will saturate the colour scale of $m_{noFDTM}/m_{withFDTM}$, which is not shown as the number of cells which change from melting to freezing is small.

The second sensitivity study (case c) tested the effect of velocity-independence in the melting parameterisation compared to the velocity-dependent control run (Fig. 3.10). This sensitivity study was conducted for the four driving conditions (cold cavity/low drag, cold cavity/high drag, hot cavity/low drag and hot cavity/high drag). However, results are presented only for the hot cavity/low drag study as it is representative of the results of the other studies. The thermal driving (top row) and friction velocity (bottom row) are plotted as colour maps with melt rate contours, where the first column is the velocity-dependent control run and the second column is the velocity-independent (i.e. constant $\gamma_{T/S}$) run.

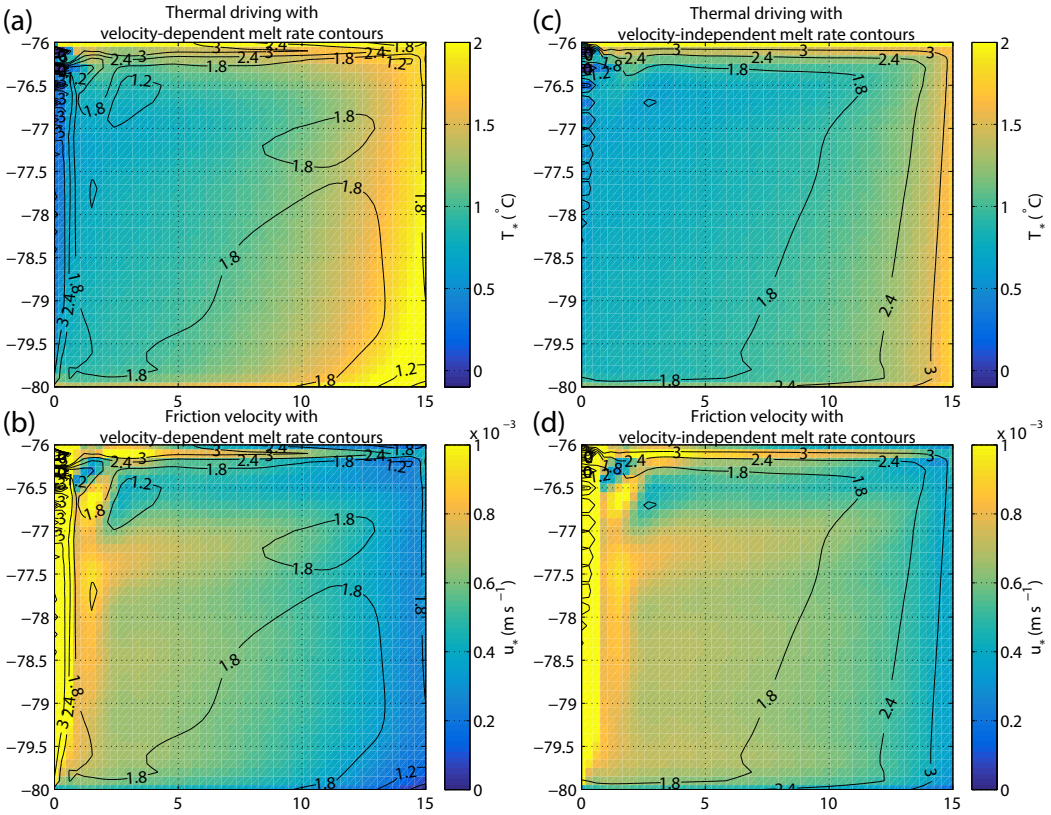

Figure 3.10: Thermal driving (a and c) and Friction velocity (b and d) plotted for the velocity-dependent control simulation (a and b) and the velocity-independent sensitivity study (c and d), with melt rate contours from the respective model run. These results are for the hot cavity environment with low drag ($C_D = 0.0005$).

Similar to Dansereau et al. (2014), we show the thermal driving and friction velocity for velocity-dependent and velocity-independent melting. In the case of velocity-dependent melting (Fig. 3.10(a and b)) there is strong correlation between m and u_* (Fig. 3.10(b)). Melting is between 1.2 m yr^{-1} and 1.8 m yr^{-1} for most of the ice shelf, including the eastern boundary where strong thermal driving exists ($\sim 2°$C), indicating that melting is limited by turbulent exchange and u_*. The strongest melting (above 3 m yr^{-1}) exists along the western boundary, where strong outflow currents drive high u_*, despite the weak thermal driving ($\sim 0.5°$C).

The velocity-independent melting study (Fig. 3.10(c and d)) shows melt rate contours aligned with thermal driving (Fig. 3.10(c)). Melting is strongest at the eastern boundary where T_* is $\sim 2°$C, and weakens towards zero at the western boundary. Friction velocity peaks along the western boundary (Fig. 3.10(d)), but as this sensitivity study enforces constant turbulent exchange velocities (independent of water velocity), melting does not increase along the western boundary.

3.4.3 Spatially- and temporally-varying drag

To test the effect of a dynamic (spatially- and temporally-varying) C_D field, two cases were run using a different C_D for melting and freezing cells. Since the freeze/melt boundary evolves with time, the C_D field is also temporally-varying.

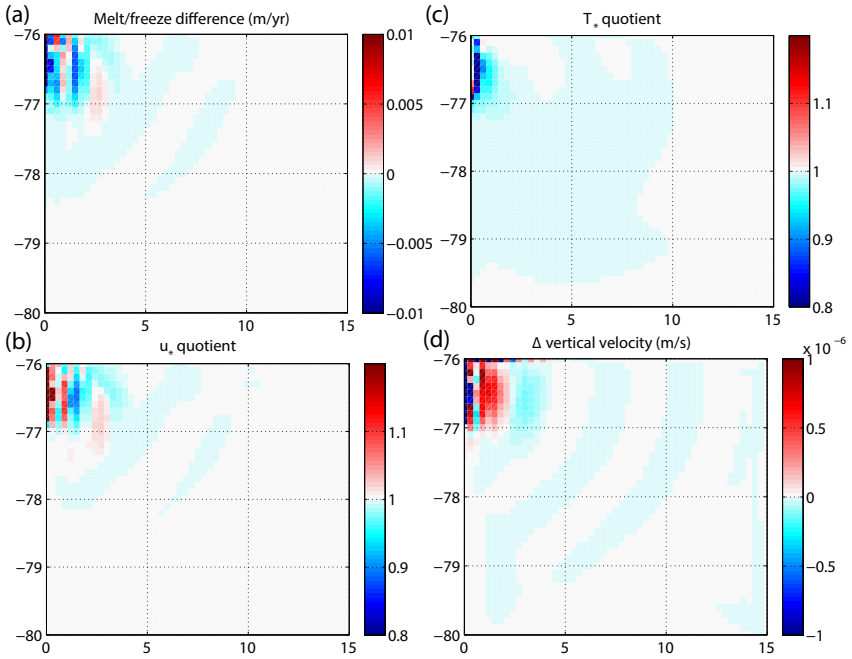

Figure 3.11: The effect of spatially- and temporally-varying drag, with $C_{D,freeze} = 0.1$. (a) The difference in melt rate between the spatially-varying drag simulation and the spatially-constant drag simulation. A positive difference indicates stronger melting or weaker refreezing, and vice versa. (b) The quotient of u_* for the dynamic drag run divided by the spatially-constant drag run. A value greater than 1 indicates increased u_*. (c) The thermal driving (T_*) quotient, calculated as T_* for the dynamic drag run divided by T_* for the spatially-constant drag run. (d) The difference in vertical velocity into the top model layer between the dynamic drag and control run. A positive difference indicates increased vertical motion/upwelling.

To determine the effect of spatially- and temporally-varying C_D, the two runs with dynamic drag are compared against a control run with spatially-constant drag. The drag coefficients for the melt zones of the sensitivity studies and the control run are chosen to be the same ($C_D = 0.003$) to allow comparison. Furthermore, this $C_{D,melt} = 0.003$ is chosen as it represents a moderate drag coefficient commonly used in the literature and thought to be physically representative for an ice interface not experiencing marine ice accretion. The cavity environment is chosen to be cold, in order to form a refreezing zone. The two dynamic drag models are similar but the results from the model with smoother refreeze zone $C_{D,freeze}$ are attenuated. As such, we report the results from the model with $C_{D,freeze} = 0.1$ and $C_{D,melt} = 0.003$ as it shows the largest difference in circulation and melt properties.

Comparing the melt/freeze distribution and magnitude between the control run (Fig. 3.4(a)) and the sensitivity studies (Fig. 3.11(a)), we see an increase in the rate of refreezing by 0.01 m yr^{-1} ($\sim$ 20%), while melting over the outflow region of the ice shelf decreased by 0.005-0.01 m yr^{-1} ($\sim$ 10%). There are two small zones of increased melting between the freeze zone and the ice shelf interior and at the ice shelf front. The area of refreezing increases by 25% (not shown).

The two contributing components to melt/freeze rates, u_* and T_*, also differ between the control runs and the dynamic drag runs. The friction velocity, Fig. 3.11(b), is generally similar across the ice shelf interior, but increases in the north-west of the ice shelf and adjacent to the freeze zone. Increased u_* is due to increased C_D over the freeze zone, but in the neighbouring melt region, where C_D is identical between the control and sensitivity runs, it indicates strengthened circulation. Thermal driving, T_*, is less for a majority of the ice shelf area as in Fig. 3.11(c). The strongest change in T_* is in the melt region adjacent to the refreeze zone where T_* is reduced by over 25%.

The difference in vertical flow into and out of the top model level displays significant changes, as in Fig. 3.11(d). There is increased downwards flow in the refreeze zone and a large adjacent area of upwards flow. From this area, a series of alternating downward then upward flow bands radiate south-east across the domain.

The spinup time for the constant drag and spatially-varying C_D simulations is approximately the same, meaning that temporal variation in C_D is of lesser importance. However, we expect that under non-steady-state forcing conditions (such as a seasonal cycle driving periodic refreezing), the temporal variation in C_D will be an important factor for changing melt dynamics.

3.5 Discussion

3.5.1 Thermal Driving

Thermal driving, T_*, is calculated as the difference in temperature and salinity between the interface (at the in situ freezing point) and the top model cell, and so signifies the potential for ice shelf melting or freezing.

For the melt regions of both cold (Fig. 3.7(a)) and hot cavities (Fig. 3.7(c)), the greatest T_* occurs for lowest C_D and as C_D increases, T_* decreases. This behaviour at low to moderate C_D is explained by the more efficient transfer of heat from the ocean to the ice shelf base as C_D is increased. Increased heat transfer removes more heat from the boundary layer while strengthened melting produces more meltwater; both of which reduce T_*.

This behaviour continues with increasing C_D but begins to plateau at high drag, which can be explained because melting increases as C_D is increased. The increased meltwater production cools and freshens the boundary layer and reduces T_*, while at the same time, increasing C_D increases the efficiency with which heat is transferred to the ice shelf base (as parameterised by γ_T). If this increases faster than

heat is transferred from the interior ocean to the boundary layer, then T_* will also decrease. This demonstrates that at high C_D, turbulent mixing is less important than meltwater input and heat transfer to the ice shelf base, for the heat balance of the boundary layer.

The cold and hot cavity refreeze zones display inverted behaviour (Fig. 3.7(b) and Fig. 3.7(d), respectively). The magnitude of T_* increases with C_D in the cold cavity, while in the hot cavity, the magnitude of T_* decreases with increasing C_D. In the cold cavity, the production of meltwater below the surface freezing point can produce freezing along the the western boundary where strong outflow exists (Fig. 3.4(a)). Increasing C_D increases meltwater production and hence negative thermal driving in the outflow zone, despite the increased vertical mixing of cool interior waters. This is in contrast to the hot cavity where increasing C_D leads to more mixing of hot interior water into the boundary layer (through turbulent and divergent entrainment). In the hot cavity, the thermal effect of mixing relatively hot interior waters (decreasing $|T_*|$ in the freeze zone) is greater than the effect of increased meltwater production (increasing $|T_*|$ in the freeze zone), leading to an overall decrease in $|T_*|$ with increasing C_D.

Comparing the refreezing between the two cavity environments (while considering the small area of refreezing in the hot cavity), the inverted behaviour suggests that thermal conditions of the interior cavity water are important for determining whether refreezing increases or decreases with C_D. In a hot cavity, higher melting leads to buoyancy driven currents, strong entrainment and vertical diffusion of relatively hot interior waters, and weakened refreezing at higher drag. In a cold cavity, weaker melting and buoyancy driven circulation reduces the importance of entrainment and diffusion of interior waters, which furthermore are cooler and less able to reduce refreezing at high drag.

3.5.2 Top layer velocities

For low to moderate drag, $|U_M|$ increases with C_D, showing the strengthening of the buoyancy-driven circulation. However, at high drag, $|U_M|$ decreases with increasing C_D, as the increasing surface roughness decelerates the water in the boundary layer (Fig. 3.8).

Despite u_* being a function of the boundary layer velocity through $u_* = \sqrt{C_D}|U_M|$, the effect of the decreasing $|U_M|$ is overcome by the increasing C_D. As a result, the friction velocity increases with increasing C_D. It is noteworthy that for high C_D in the hot cavity, u_* begins to plateau, because the high drag is significantly decelerating the boundary layer flow.

The presence of a maximum $|U_M|$ in both the cold and hot cavity environments indicates that deceleration of circulation due to increasing drag is stronger than the increased buoyancy-driven circulation at higher melt. The local maximum in $|U_M|$ occurs at a lower drag for the warmer cavity environment. This is possibly due to the relative contributions from the positive effect of increasing buoyancy driven circulation and the negative effect of deceleration from the rougher interface. In a

hot cavity environment where melting is very strong even at low drag, melting will become less sensitive to increasing drag (see the change of slope of the melt rate with increasing drag in Fig. 3.5(c) vs. Fig. 3.5(a)) and hence the buoyancy driven circulation will no longer increase in strength with C_D, reaching an upper bound. In the hot cavity, the increase in buoyancy driven circulation is not as strong at low to moderate C_D, allowing the deceleration from increasing drag to decrease $|U_M|$. This is in contrast to the cold cavity, where buoyancy driven circulation is still strongly increasing until moderate to high C_D where the frictional effects become apparent. Assuming that the location of the local maximum in $|U_M|$ is due to the strength of the increase in buoyancy driven circulation, it follows that in a very hot cavity environment (i.e. warmer inflow waters than are simulated here), where buoyancy driven circulation is at a maximum at low drag, frictional effects will dominate and $|U_M|$ will begin to decrease at low C_D.

3.5.3 Melt rate

The increasing area-averaged melt rate with C_D for low to moderate C_D (Fig. 3.5) is consistent with heat flux which is proportional to the drag coefficient. While the lower interface friction should lead to fast boundary layer flow, the lower drag decreases the turbulent mixing of heat (and salt) at the ice shelf–ocean boundary necessary to increase melt rates. This behaviour is similar for both hot and cold cavity scenarios. As C_D is increased, turbulent mixing increases, driving stronger melting.

Theoretically, this is explained by m increasing with increasing turbulent exchange (Eq. 3.2). Since the turbulent exchange velocities, $\gamma_{T/S}$ increase with increasing u_* (Eq. A.4), and u_* increases with $\sqrt{C_D}$ (Eq. 3.1; assuming the decrease in $|U_M|$ is less than the increase in $\sqrt{C_D}$), so we might expect m to increase with increasing C_D.

As C_D reaches moderate to high values, the behaviour of m changes. This is most noticeable in the hot cavity as a plateauing in m for $C_D > 0.01$. While it is tempting to attribute this to the decreasing top layer velocity magnitude (due to increased drag), u_* is still increasing with C_D. Consequently, the maximum in m must be attributed to the low T_* at high C_D. Therefore, the local maximum in the m–C_D relationship indicates a transition from velocity driven-melting to heat limited-melting. In a cavity environment hotter than that simulated here, buoyant circulation would be strong at low C_D and the effect of increasing drag would occur at lower C_D. As a result, u_* would plateau at lower C_D and m would peak at lower C_D.

The range of choices for C_D, as quoted in the literature, falls on the flank of the local maximum of melting in both the hot and cold cavity scenarios. This indicates higher sensitivity of m to C_D than if the range of C_D choices had fallen on the local melt maxima. Assuming that the range of C_D represents an estimate of uncertainty in C_D, these results suggest a 25% (in the hot cavity) to 70% (in the cold cavity) change in melt rates across the range of uncertainty. In a cavity environment warmer than simulated here, the local melt maximum could fall within the range of commonly

chosen C_D, leading to increased robustness to uncertainty in C_D.

Dansereau et al. (2014) investigated the difference in melt rate distribution between velocity-independent and velocity-dependent exchange coefficients, $\gamma_{T/S}$, for a situation similar to our hot cavity scenario and over approximately the same range of C_D. They found melting was controlled primarily by thermal driving in the velocity-independent case and by the strength of the boundary layer current in the velocity-dependent case. Their results agree with the relationship between melt rate and the low to moderate values of C_D used in this study (Section 3.4.1-3.4.2). However, at high values of C_D, we encounter a decrease in m with increasing C_D, that occurs when the thermal driving continues to decrease while u plateaus. Dansereau et al. (2014) do not encounter a maximum C_D beyond which m decreases. The Dansereau et al. (2014) simulations are forced with hot inflowing water, which leads to stronger currents and higher melt rates than those produced in this study (Section 3.4.1). It may be that Dansereau et al. (2014) cannot separate the frictional deceleration due to the strength of the forced inflow. It is also unknown to what extent the vertical diffusion parameterisation (constant coefficients) of Dansereau et al. (2014) is limiting the simulation of a C_D-m maximum.

3.5.4 Frictional-driven turbulent mixing and velocity-dependent melting

The most pronounced effect of removing friction-driven turbulent mixing is the strengthening of melting along the edges of the refreeze zones and the subsequent contraction of the area of refreeze (Fig. 3.9). This is present in the high drag simulations for both cavity environments, but is not present in either of the low drag simulations (which display zero or limited refreezing). It is likely that this constricted refreezing process occurs at any drag, as long as there is sufficient outflow and negative thermal driving to cause refreezing.

Other noticeable effects are decreased refreezing (in the models that display refreezing) of approximately 5%, and a widespread but weak decrease in melting.

These effects can be explained by the role that friction-driven turbulence has on mixing of heat and salt into the boundary layer. Turbulence created by basal roughness increases mixing of interior water into the boundary layer. In these experiments, the interior water is warmer and saltier than water close to the ice shelf, due to cold, fresh meltwater production. By removing the mixing of warmer interior waters into the boundary layer, melting is reduced. The reduction in freeze rates along the western boundary for both high drag scenarios can be explained by reduced meltwater production; and, reduced turbulent mixing leading to a thinner boundary layer. The contracting freeze zone is due to a strong increase in melting directly adjacent to the refreeze zone pushing westwards the negative thermal driving necessary for freezing. This zone of increased melt can be traced to strengthening of the sub-ice shelf recirculation, particularly along the western boundary.

The spatial pattern of melting and refreezing is shown to be strongly dependent on whether or not boundary layer velocity is included in the melting parameterisation.

Model runs which use velocity-independent constant exchange coefficients ($\gamma_{T/S}$) display a melt distribution that is spatially correlated with the degree of thermal driving (see Losch, 2008). Model runs which implement exchange velocities that vary as a function of the currents (u_*) show a melt rate distribution which is principally correlated with the current field and the thermal driving to a lesser degree.

Dansereau et al. (2014) investigated the difference in melt rate distribution between velocity-independent and velocity-dependent exchange coefficients, $\gamma_{T/S}$, for a situation similar to our hot cavity scenario and over approximately the same range of C_D. They found melting was controlled primarily by thermal driving in the velocity-independent case and by the strength of the boundary layer current in the velocity-dependent case. Our study further supports results suggesting that melting will not necessarily be focussed where T_* is high (such as deep ice shelf grounding lines) but likely to be shifted to regions where strong flow past the ice shelf interface exists (Mueller et al., 2012; Dansereau et al., 2014), which motivates the inclusion of velocity-dependent turbulent exchange velocities (Jenkins et al., 2010). The similarity in our results to those of Dansereau et al. (2014), in spite of different lateral boundary forcing (closed lateral boundaries versus boundary inflow in Dansereau et al. (2014)) supports our choice of closed lateral boundaries and further reinforces the robustness of melting aligning with regions of strong flow.

3.5.5 Impact of spatially and temporally varying drag

The results from the dynamic drag experiment (Section 3.3.3) showed variation in the distribution and magnitude of melt rate (Fig. 3.11). The most important aspects are differences in melt rate distribution and magnitude, circulation and thermal driving which occur outside of the refreeze zone. Since the sensitivity and control studies use the same C_D for melt zones, any differences in the melt regions are a result of altered circulation and heat transport beneath the ice shelf. These differences have implications for ice shelf–ocean models which simulate substantial refreeze zones with the same C_D for both freezing and melting regions.

Freezing is increased in both magnitude and extent, in agreement with the results shown in Section 3.4.1 and discussed in Section 3.5.3. Changes to refreezing are due to increased drag leading to increased turbulent exchange velocities and increased flux across the ice shelf–ocean interface. However, the area of higher C_D is not large enough to significantly decelerate the general sub-ice shelf circulation.

Broad changes to U_M across the melt zone are a result of the increased refreezing driving stronger brine rejection, densification and overturning circulation. Increased densification in the refreeze zone changes horizontal pressure gradients and causes changes in horizontal circulation. Convergence and divergence resulting from the altered horizontal circulation then leads to downwelling and upwelling, respectively. A series of altered upwelling and downwelling bands form, radiating from this outflow region across the ice shelf. These bands of altered vertical velocity lead to a reorganisation of circulation along the ice shelf interface and drive stronger melting in two localised regions. The most important region of altered melting is the deeper

band of increased melting (strongest at 77°S, 2.5°E), which produces more meltwater. The freshening and cooling effect of the increased melting leads to a swath of decreased T_* as the general circulation directs the meltwater to the north-west.

These results have important implications for ice shelf–ocean models and particularly those that utilise a single C_D for the entire ice shelf interface. Refreezing can be systematically underestimated, if C_D is spatially unchanging and chosen to best fit smooth, melt-dominant environments, as is often the case. Incorporating a C_D which is rougher for zones of refreezing will more realistically capture the sub-ice shelf environment in the presence of refreezing, leading to increased freeze rates. Furthermore, the effect of altered refreezing is not confined to the refreeze zone. Circulation patterns alter and reconfigure across the rest of the ice shelf, leading to significantly changed melting magnitude and distribution, motivating the importance of including distinct $C_{D,melt}$ and $C_{D,freeze}$.

Furthermore, these results provide strong motivation and support for the development of wide-scale geophysical observation techniques for basal roughness, similar to that demonstrated for detecting and quantifying surface-roughness elements from an airborne radar platform (e.g. Grima et al., 2014). Hydrographic measurements of turbulence beneath ice shelves will also be required to calibrate wide-scale roughness observations (e.g. Robinson et al., 2010; Stanton et al., 2013; Stevens et al., 2014).

3.6 Conclusions

Ice shelf basal melting is an important control on mass loss from Antarctica and hence the rate of sea level rise. Observations of basal melting and ocean state are difficult to achieve in situ, but can be readily simulated in numerical ocean models which capture the thermodynamic interaction of the ocean and ice shelves. We have run idealised ice shelf–ocean simulations, based on ROMS, with a commonly used parameterisation of ice–ocean thermodynamic interaction to investigate the effect of basal roughness on melting and freezing.

Melt rate increases with increasing C_D. However, we found that for a hot cavity environment, the rate of increase of melting plateaus for high C_D. It follows that for a very hot cavity scenario, melting will not increase and may even decrease with C_D. Friction velocity increases with increasing drag, even though water in the boundary layer is experiencing increasing deceleration from basal roughness. Increased friction velocity leads to increased exchange across the ice–ocean interface, and increased melting (and freezing). Increased melting produces more meltwater, and together with more efficient heat transfer from the boundary layer to the ice, thermal driving decreases with increased C_D. Beneath refreeze zones, the situation is more complicated. In the cold cavity, buoyancy driven circulation, entrainment and diffusion of cool interior waters into the boundary layer are a weaker effect than the increased meltwater production, leading to stronger negative thermal driving at high drag; in the hot cavity, buoyancy driven circulation is strong, entraining more warm interior water into the boundary layer and reducing the negative thermal driving from meltwater.

Sensitivity studies showed that the effect of a vertical mixing scheme transporting heat into the boundary layer as a result of roughness at the ice–ocean interface is particularly important for capturing the magnitude and area of refreezing. Neglecting this effect, possibly through a poor or unresolved boundary layer scheme, can lead to underestimation of refreezing. Melting can be more dependent on the distribution of currents (u_*) rather than the distribution of thermal driving. This suggests that melting can be focussed in areas of strong flow rather than areas of solely strong thermal driving, so that melting may not be strongest at the deep grounding zones.

A drag coefficient that was larger for areas of refreezing and smaller for areas of melting led to variations in refreezing and melting across the entire ice shelf interface. Strengthened refreezing due to a rougher and more realistic C_D has implications for ice shelf–ocean models that simulate colder cavity ice shelves with substantial areas of refreezing. However, changes to melting across the entire ice shelf as a result of a spatially-varying C_D prompts the inclusion of a more realistic treatment of C_D for all ice shelf–ocean models. Ultimately, this would entail including a spatial distribution of basal roughness from observations, further motivating the continued development of wide-scale geophysical observations of basal roughness.

Future ice shelf–ocean model intercomparison projects and models may benefit from a standardised geometry and forcing that is modified to increase realism, such as with tidal forcing, different bathymetry or non-linearly sloped ice shelf draft. Furthermore, understanding of the role of large-scale roughness features, such as crevasses and inverted melt channels which act to constrain and modify melting (Dutrieux et al., 2014), would benefit through further investigation with idealised models (e.g. Gladish et al., 2012).

Lastly, we conclude that as model vertical resolution improves, it may be necessary to reformulate the standard practice for implementing the Holland and Jenkins (1999) ice–ocean thermodynamic parameterisation.

Chapter 4

MODELLING ICE SHELF BASAL MELTING IN A CHANGING OCEAN CAVITY ENVIRONMENT

In Chapter 1, key uncertainties in ice shelf–ocean interaction were introduced. These uncertainties affect our ability to realistically simulate Antarctica in a changing climate. In Chapter 3, we explored the parameterisation of turbulent heat transfer that partly governs ice shelf–ocean interaction, and how basal roughness affects melting and freezing. However, there also exist uncertainties in the fundamental response of melting and freezing to different forcing conditions. One such condition is the thermal environment of the ocean cavities beneath ice shelves.

In this chapter, we use a numerical model that simulates interaction between an idealised ice shelf and the ocean, to investigate the response of basal melting and freezing to different ocean temperatures. These ocean temperatures are chosen such that the results represent both cold and hot ice shelf cavities, and the transition between these states. Furthermore, we investigate the response of basal melting in a cold ice shelf cavity to a simple parameterisation of tides.

The following chapter is sourced from the article currently submitted: Gwyther, D. E., Cougnon, E. A., Galton-Fenzi, B. K., Roberts, J. L., Hunter, J. R., and Dinniman, M. S. Modelling ice shelf melting in a changing ocean cavity environment. *Annals of Glaciology*, submitted 2015b. It has been edited for formatting and the abstract has been removed; the content remains unaltered.

4.1 Introduction

Accurate estimates of the mass balance of Antarctic ice grounded above flotation are important for constraining projections of global sea level rise. Accumulation of snow provides positive input to the mass balance, while Antarctica loses mass through wind-driven ablation, sublimation and discharge across the grounding line.

The largest loss of ice is due to ice flowing across the grounding line into the floating ice shelves. These ice shelves provide an important buttressing back stress (Dupont and Alley, 2005) on the fast-flowing ice streams and glaciers, and their removal can lead to rapid ice stream acceleration (Scambos et al., 2004) and sea level rise.

The removal of mass from ice shelves occurs through calving of icebergs from the terminus and melting at the ice shelf base. The ratio of basal melting to calving has a strong regional variability (Depoorter et al., 2013), but for the whole of Antarctica is approximately 2:1 (1516±106 Gt yr^{-1} basal melt versus 755±24 Gt yr^{-1} calving; Liu et al., 2015). Iceberg calving can be observed from satellites and so its contribution to the Antarctic mass budget can be quantified (Liu et al., 2015). Access to the ocean-filled cavity beneath ice shelves and measuring basal melting in situ is logistically difficult; sea ice impedes access from the open ocean; and, surface access through borehole drilling leads to sparse observations. As a result, estimates of basal melting are derived from modelling studies (e.g. Gwyther et al., 2014), surface elevation (Moholdt et al., 2014), surface velocity field (Warner and Roberts, 2013) or phase-sensitive radar echo sounding arrays (Jenkins et al., 2006).

Basal melting is driven by ocean water above the in situ freezing point, being mixed to the ice–ocean interface. The traditional description of basal melting is as an 'ice pump' (Lewis and Perkin, 1986). In this scenario, ocean water melts ice at depth, the buoyant meltwater plume ascends along the ice shelf base until it is cooler than the in situ freezing point, whereby it freezes directly on to the ice shelf base and via accretion of frazil crystals. The refreezing and associated brine rejection causes densification; the divergent flow further reinforces the buoyant upwelling of meltwater. The currently accepted view on melting takes into account the availability of heat and the magnitude of currents which turbulently mix warmer ocean water to the ice–ocean interface (Holland and Jenkins, 1999). This description suggests strong melting will be located where there are warm ocean temperatures and strong flow, which is typically thought to be adjacent to the deep grounding line.

Here, the sub-ice shelf oceanic environment can be divided into two broad classifications of 'cold cavity' or 'hot cavity' by the relative temperature of the inflowing water, following Joughin et al. (2012). Hot ocean cavity environments are roughly defined by water well above the in situ freezing point flowing beneath the ice shelf and driving strong melting with an area-averaged melt of $\mathcal{O}(10)$ m yr^{-1}. The archetypical hot ice shelf cavity is the Pine Island Ice Shelf, where strong melting is driven by Circumpolar Deep Water nearly 4°C above the in situ freezing point (Jacobs et al., 2011). Cold ocean cavity environments are characterised by water having a temperature close to the surface freezing point entering the ice shelf cavity and driving weaker basal melting with an area-averaged melt of $\mathcal{O}(0.1-1)$ m yr^{-1}. In the cold cavity environment, ascending buoyant meltwater can produce supercooling, frazil formation and significant marine ice accretion. Ice shelves that fit this classification include the Larsen C ice shelf and the three largest ice shelves, the Ross, Ronne-Filchner, and Amery ice shelves.

Due to the logistical constraints that makes observing the sub-ice shelf environment difficult, improved understanding of ice shelf–ocean interaction is often gained

through modelling studies. Three-dimensional idealised ice shelf studies have investigated basics of cavity circulation and melting (Grosfeld et al., 1997), cold cavity melting (Losch, 2008), the effect of geometry on controlling melting (Holland et al., 2008; Little et al., 2009), coupled ice stream-ocean interaction (Goldberg et al., 2012), hot cavity melting (Dansereau et al., 2014), and the effect of drag on melting (see Gwyther et al., 2014, and Chapter 5). These studies have all differed in the parameters they explored; hot or cold cavity interaction, varying basal roughness, geometry, and, velocity-dependent or independent melting. Yet, many aspects of the parameter space remain unexplored, such as tidal forcing of an idealised ice shelf. Many simulations have investigated ice–ocean interaction beneath realistic ice shelf geometries, but realistic tidal forcing is not always used. Tides have been shown to have a large impact on the magnitude of melting and freezing (Makinson et al., 2011), as well as on the distribution of melting (Mueller et al., 2012). The effect of tides on cold cavity ice shelves, such as the Larsen C (Mueller et al., 2012), Ronne-Filchner (Makinson et al., 2011), Ross (Arzeno et al., 2014) and Amery (Galton-Fenzi et al., 2012) ice shelves have been investigated, as well as the effect of modelling tides beneath hot cavity ice shelves, such as Pine Island Glacier ice shelf (Robertson, 2013).

This study uses numerical models to investigate melting and freezing under different ocean cavity environments and the impact of tidal mixing and how melting and freezing respond. Unlike previous realistic geometry simulations, this study uses an idealised geometry which simplifies ice shelf–ocean interactions. A range of different ocean cavity temperatures will be simulated, allowing for a more general understanding of the role of ocean cavity temperature on melting. The effect of simple analytical tidal forcing on melting will be investigated in an idealised environment. These results will also explore the use of explicit tidal forcing as opposed to implicit tidal RMS forcing (e.g. Losch, 2008), and further motivate the inclusion of tidal forcing in simulations of realistic ice shelves.

4.2 Methods

4.2.1 Model Setup

This study employs an adapted version of the Regional Ocean Modeling System (ROMS; Shchepetkin and McWilliams, 2005) to simulate ice shelf–ocean interaction. ROMS solves the three-dimensional primitive equations of fluid flow using finite difference methods with a terrain-following vertical coordinate system. This vertical coordinate system stretches the distribution of vertical cells to the water column thickness, thereby allowing high vertical resolution in shallow coastal environments and ice shelf cavities. ROMS is modified to include ice shelf mechanical pressure following others (Dinniman et al., 2007; Galton-Fenzi et al., 2012). Vertical momentum and tracer mixing through the ocean interior and the surface boundary layer are simulated with the K-Profile Parameterisation (KPP) mixing scheme (Large et al., 1994). Ice shelf basal drag is parameterised with a quadratic drag

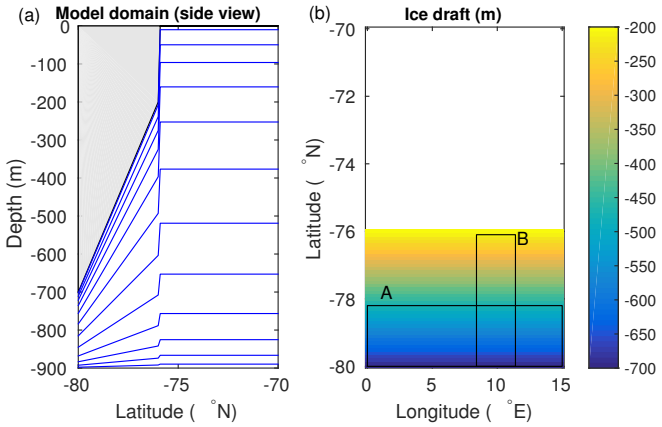

Figure 4.1: Model geometry from (a) side view, with bathymetry at 900 m below the surface and ice shelf shown in grey, and every second sigma level shown in blue. (b) Ice shelf linearly slopes down to 700 m with a 200 m thick ice front at 76°S. Location of zones averaged for Figure 4.3 are marked A and B.

formulation, relating top layer velocity and friction velocity via a spatially-constant drag coefficient, $C_D = 0.003$. Ice shelf–ocean thermodynamics are captured with the three-equation parameterisation (Hellmer and Olbers, 1989; Holland and Jenkins, 1999; Scheduikat and Olbers, 1990), which assumes thermodynamic equilibrium at the ice shelf–ocean interface to solve for the basal temperature and salinity and hence determine melting and freezing rates. The turbulent exchange of heat and salt across the boundary layer is captured with the use of exchange velocities for heat and salt, γ_T and γ_S, respectively. In this application, the exchange velocities are a function of the friction velocity (described under section "Ice Shelf–Ocean Thermodynamics").

The design of the model geometry (see Figure 4.1) is based on the Ice Shelf–Ocean Model Intercomparison Project (ISOMIP) Model 2 series of experiments (Hunter, 2006) with a modified geometry that is based on Grosfeld et al. (1997). A linearly sloping ice shelf covers the southern portion of the domain; it is 700 m at its deepest and 200 m at the ice front. The bathymetry is a constant 900 m depth. The horizontal grid resolution is about 10 km and the 24 vertical levels have a sigmoidal distribution, enhancing vertical resolution near both the upper and lower surfaces. For example, thicknesses of the upper, mid and lower cells are approximately 0.007, 0.078 and 0.02 times the water column thickness, respectively. The model is initialised with a uniform temperature of -1.9°C and salinity of 34.4 (all salinities quoted are on the Practical Salinity Scale and are dimensionless). The model lateral boundaries are closed. The open ocean surface boundary is restored towards constant temperature and salinity values over a daily timescale, designed to force the model to exhibit realistic oceanic conditions. Cold cavity conditions are simulated by restoring the open ocean surface to -1.9°C and salinity of 34.5, while the hot cavity environment is simulated by relaxing the open ocean surface to 0.5°C and salinity of 34.6. The surface forcing conditions chosen for all model runs are

approximately the same density.

Terrain-following vertical coordinate models, such as ROMS, are susceptible to pressure gradient errors where there is steep changes in water column thickness. However, numerical algorithms employed in ROMS are designed to minimise the effect of pressure gradient errors (Shchepetkin, 2003; Galton-fenzi, 2009). We have run a zero forcing test (results not shown) to determine the magnitude of pressure gradient errors; spurious currents are largest along the ice front, but are minimal (below 6×10^{-4}m s^{-1}) in comparison to the flow rate in the forced experiments. Furthermore, the change in ice thickness at the ice front occurs over one cell width, with a slope of $\sim 1/50$.

4.2.2 Ice Shelf–Ocean Thermodynamics

Melting and freezing depends on the difference between the rate of ocean heat supplied to the ice–ocean interface and the rate of heat conducted into the ice shelf above. As the ocean flows past the ice interface, a boundary layer forms where the basal friction modifies the flow. The typical bottom boundary layer thickness is $\sim \mathcal{O}(10)$ m (Soulsby, 1983), but will likely be somewhat different in the case of the ice–ocean boundary, due to the melting or freezing and the associated effects on stratification. Within the ice–ocean boundary layer (composed of an outer layer, log layer and viscous sublayer), velocity shear between the ice interface (at zero velocity) and the edge of the boundary layer (at the free-stream flow) generates turbulence. Heat and salt is then transported via turbulent exchange across the boundary layer, driving melting or freezing, which occurs at the thin liquid water layer adjacent to the interface (McDougall et al., 2014). Modern numerical ocean models will typically have at least one cell in the boundary layer (the number will likely vary between models with different vertical coordinate systems and resolutions), and may or may not resolve the boundary layer–free-stream flow interface. Dynamics within the boundary layer, for example vertical turbulent diffusivity of heat and salt, will not be resolved and hence must be parameterised.

Most current ice shelf–ocean models (e.g. Cougnon et al., 2013; Dansereau et al., 2014; Galton-Fenzi et al., 2012; Gladish et al., 2012; Gwyther et al., 2014) simulate ice–ocean thermodynamic interaction using the three-equation parameterisation of Holland and Jenkins (1999), which assumes the ice shelf–ocean interface to be the local freezing point temperature. For more parameterisation details, see Appendix A or Holland and Jenkins (1999).

The heat flux across the boundary layer to the interface is given by $Q_M^T = \rho_M c_{p,M} \gamma_T (T_B - T_M)$, where ρ_M and $c_{p,M}$ are the ocean density and heat capacity, respectively, and T_B and T_M are the temperatures at the ice shelf base and boundary layer, respectively. An analogous expression exists for Q_M^S. Turbulent mixing to the ice–ocean interface is captured through turbulent exchange velocities,

$$\gamma_{T/S} = \frac{u_*}{\Gamma_{Turb} + \Gamma_{Mole}^{T/S}} \tag{4.1}$$

where T and S represent equations for heat and salt transfer respectively. The

shear stress through the boundary layer, which creates turbulence, is described by the friction velocity, u_*. A quadratic drag formulation is commonly used to relate the friction velocity to the free-stream flow via a drag coefficient, C_D. Molecular diffusion through the thin, viscous sublayer $\mathcal{O}(0.01)$ m thick (Soulsby, 1983) immediately adjacent to the ice interface is accounted for through $\Gamma_{Mole}^{T/S}$, while turbulent exchange across the boundary layer is parameterised with Γ_{Turb}, following McPhee et al. (1987) as,

$$\Gamma_{Turb} = \frac{1}{\kappa} \ln \left(\frac{u_* \xi_N \eta_*^2}{f h_\nu} \right) + \frac{1}{2 \xi_N \eta_*} - \frac{1}{\kappa}, \tag{4.2}$$

where the von Kármán constant $\kappa = 0.40$, $\xi_N = 0.052$ is a dimensionless stability constant, η_* is the stability parameter (McPhee, 1981), h_ν is the viscous sublayer thickness and f is the Coriolis parameter. We assume a destabilising buoyancy flux and set $\eta_* = 1$, following others (Dansereau et al., 2014). Since Γ_{Turb} is undefined for $u_* = 0$, we introduce a special condition as $u_* \to 0$, as discussed in Section 4.2.3.

4.2.3 Low-circulation limit

The turbulent transfer coefficients introduced in the three-equation parameterisation (Holland and Jenkins, 1999) were developed based on sea ice and laboratory studies (Kader and Yaglom, 1972; McPhee et al., 1987; McPhee, 1994). The sea ice–ocean interface may be a relatively different environment to the ice shelf–ocean interface. For example, unless there are strong buoyant plumes present, the relative velocity between the ocean and the sea ice will often be greater than that between the ocean and an ice shelf, negating the need to consider a limit as $u_* \to 0$ under sea ice. Furthermore, investigations have shown that the transfer coefficient scheme introduced in McPhee et al. (1987) and Holland and Jenkins (1999) may not be necessary to match observations (Jenkins et al., 2010), and will not correctly parameterise a water column with complex stratification (Kimura et al., 2015). There is motivation to further investigate ice shelf–ocean thermodynamic parameterisations, particularly as model vertical resolution improves (see Gwyther et al., 2015, and Chapter 3). However, we wish to employ the melt parameterisation most often used by modellers, so as to make these results generally applicable or useful. As such, we apply a correction that accounts for the case of very weak flow with negligible turbulence.

The implementation of a lower limit on u_* in the three-equation parameterisation is necessary to ensure the melt rate does not become undefined. The turbulent transfer coefficient (Γ_{turb}; Equation (4.2)) contains the natural logarithm of u_*, which is undefined for stationary water[1] ($u_* = 0$), and approaches negative infinity as $u_* \to 0$. It follows that the calculation of $\gamma_{T/S}$ must be implemented with a conditional statement to set the turbulent transfer coefficient to zero if boundary layer flow reaches a minimum threshold, $u_{*,min}$. This is achieved by setting $\Gamma_{turb} = 0$

[1]Note: Γ_{turb} is also undefined for $f = 0$, i.e. at the equator.

and enforcing $u_* = u_{*,min}$, in which case Equation (4.1) will simplify to $\gamma_{T/S,min} = \frac{u_{*,min}}{\Gamma^{T/S}_{Mole}}$.

The justification for implementing a minimum friction velocity is the case where flow along the ice–ocean interface is laminar, and heat transfer can occur through diffusion alone. The rate of heat transfer across the unresolved portion of the log layer (from the centre of the top model cell to the interface) will result only from the molecular diffusion of heat in seawater ($\kappa_T = 1.4{\times}10^{-7}\mathrm{m\,s^{-1}}$). From Equations (4.1) and (4.2), a value of $u_{*,min} = 2 \times 10^{-5}$ m s^{-1} leads to $\gamma_{T/S,min}$ being approximately equivalent to heat transfer by molecular thermal diffusion (κ_T), to within an order of magnitude.

In reality, the presence of tidal currents will likely ensure currents are larger than the $u_{*,min}$ limit. However, at the shallow water column near grounding zones (Holland, 2008) or at slack water, tidal currents may be weak enough that they fall below the $u_{*,min}$ limit. In these cases, it is necessary to ensure that a lower limit is placed on u_*.

4.2.4 Experimental Design

Experiment 1: Melt relationship with cavity temperature

Recently, the spatial distribution of melting and freezing in an idealised hot cavity was explored (Dansereau et al., 2014). This experiment will investigate the changes in melt rate distribution and magnitude for four different thermal environments, from a cold to hot ocean cavity. For each run, the surface forcing is achieved by restoring the open ocean surface to a different set of salinity and temperature values (see Table 4.1) on a daily timescale. All simulations are run for 30 years, at which point they are in a pseudo steady state. A zero forcing run (no surface or lateral forcing, tides or ice shelf thermodynamics) is conducted to test for spurious flow resulting from pressure gradient errors.

Experiment 2: Tidal forcing

In a cold cavity environment, we expect low thermal driving will decrease melting and buoyant circulation and as a result circulation within the ice shelf cavity will be weak, as shown by many modelling studies (e.g. Holland et al., 2003). However, as mentioned previously, it is likely that tidal currents are important for maintaining a significant background flow, will likely change the circulation within the cavity (Makinson et al., 2011; Mueller et al., 2012; Arzeno et al., 2014), and are often used to motivate the choice of constant $\gamma_{T/S}$.

This study investigates how circulation and melting in a hot and cold ocean cavity are altered by the addition of a simple analogue of tides. Furthermore, we assess the friction velocity generated by tides in the absence of buoyancy-driven circulation by removing ice shelf thermodynamics and surface forcing (zero forcing + tide,

	Run	Surface forcing Temperature	Salinity
Exp. 1	Zero forcing	-	-
	1	-1.9°C	34.500
	2	-1.5°C	34.513
	3	-0.5°C	34.565
	4	0.5°C	34.600
Exp. 2	Zero forcing + tide	-	-
	1 + tide	-1.9°C	34.500
	4 + tide	0.5°C	34.600

Table 4.1: Summary of experiments showing the surface forcing conditions that drive variation in oceanic environment.

Table 4.1)

There are several possibilities for incorporating the influence of tides. A commonly used option is to set constant turbulent exchange coefficients, $\Gamma_{T/S}$, chosen such that they parameterise a constant background current representative of tidal flow (see Losch, 2008). However, this will not allow spatial or temporal variation in turbulent exchanges due to buoyancy-driven flow. Another option is to add an offset in the calculation of the friction velocity, equivalent to a root-mean-square (RMS) tidal current, for example, $u = u' + |u|_{tide}$, where u' is the circulation without tides, and $|u|_{tide}$ is constant value equal to the root-mean-square tidal currents. The offset will impose a lower threshold on currents, equivalent to the mean tidal flow (as suggested by Jenkins et al., 2010). However, this approach does not capture other effects associated with tides, such as mixing.

We directly include tides by clamping the north-south vertically-integrated velocity on the northern boundary to be a sinusoid with amplitude 0.1 m s^{-1}, and period of 12 hours. This approach generates an idealised tidal wave with period approximately equivalent to the M_2 tidal constituent. The critical latitude (where the tidal frequency equals the Coriolis or inertial frequency) for this modified M_2 tide is ∼85.8°S, which is well south of the southern boundary of the model domain and therefore unlikely to cause more complex tidal dynamics as have been found in ice shelf cavities where the critical latitude is closer to the ice shelf (e.g. Makinson et al., 2006).

The boundary remains closed to temperature and salinity, as in Experiment 1, and the surface forcing is identical to the respective run of Experiment 1 (see Table 4.1). Note that the model surface (including under the ice shelf) is free to move up and down. This approach will allow for tidal mixing as well as allow for spatial and temporal variation in turbulent exchange, and has been employed by various realistic applications (e.g. Mueller et al., 2012; Galton-Fenzi et al., 2012).

The time step and output frequency were chosen to be multiples of the tidal period

to minimise tidal aliasing. The model is spun up for 29 years, and analysis is conducted on the temporal average of the 30^{th} year of model output.

4.3 Results

4.3.1 Experiment 1: Melt relationship with cavity temperature

Run	m (m yr^{-1})	u_* (m s^{-1})	T_* (°C)
Zero forcing	0.00	1.02×10^{-6}	0.32
1	0.07	2.27×10^{-4}	0.15
2	0.31	5.58×10^{-4}	0.26
3	1.36	1.36×10^{-3}	0.46
4	2.89	2.08×10^{-3}	0.63
Zero forcing + tide	0.00	2.9×10^{-3}	0.32
1 + tide	0.14	2.68×10^{-3}	0.02
4 + tide	3.35	3.30×10^{-3}	0.43

Table 4.2: Summary of area averaged melt rate, friction velocity and thermal driving for each experiment.

Between run 1 and run 4, the area-averaged melt rate increases $\sim$ 41 times, the area-averaged u_* increases $\sim$ 9 times and the area-averaged T_* increases $\sim$ 4 times (see Table 4.2). While the relationship of u_* versus m and T_* versus m each vary above-linear, the relationship of T_*u_* versus m, given by $m = \alpha u_* T_*$ is linear, with $\alpha = 7\times10^{-5}$ °C^{-1} (plot not shown). The spatial distribution of steady-state melting (positive) and freezing (negative) is shown in the first column of Figure 4.2.

The coldest cavity environment (run 1) displays melting centred along the western boundary towards the grounding line. Weak melting is present across the rest of the ice shelf with a weak melt gradient oriented south-north (stronger-to-weaker melting). Freezing occurs along the western boundary, adjacent to the ice front. For marginally warmer conditions (run 2), high melt rates still occur at the south-western corner of the cavity, while the refreezing zone is smaller than in run 1. Melting across the cavity increases in magnitude and begins to form a melt gradient, oriented southeast-northwest (stronger-to-weaker melting). However, for this cavity environment at the extrema of the south-eastern corner, melting is still weaker than the southern and eastern boundaries. For a cavity environment warmer still (run 3), the average magnitude of melt increases. The orientation of the spatial melt gradient rotates counterclockwise, with strong melting present along the eastern boundary. There is also strong melting present along the ice front. For the hottest cavity environment (run 4), melting is an order of magnitude higher than the coldest cavity environment (run 1). The gradient in melting has now rotated further counterclockwise, and is almost oriented east-west (strong-to-weak melting). The

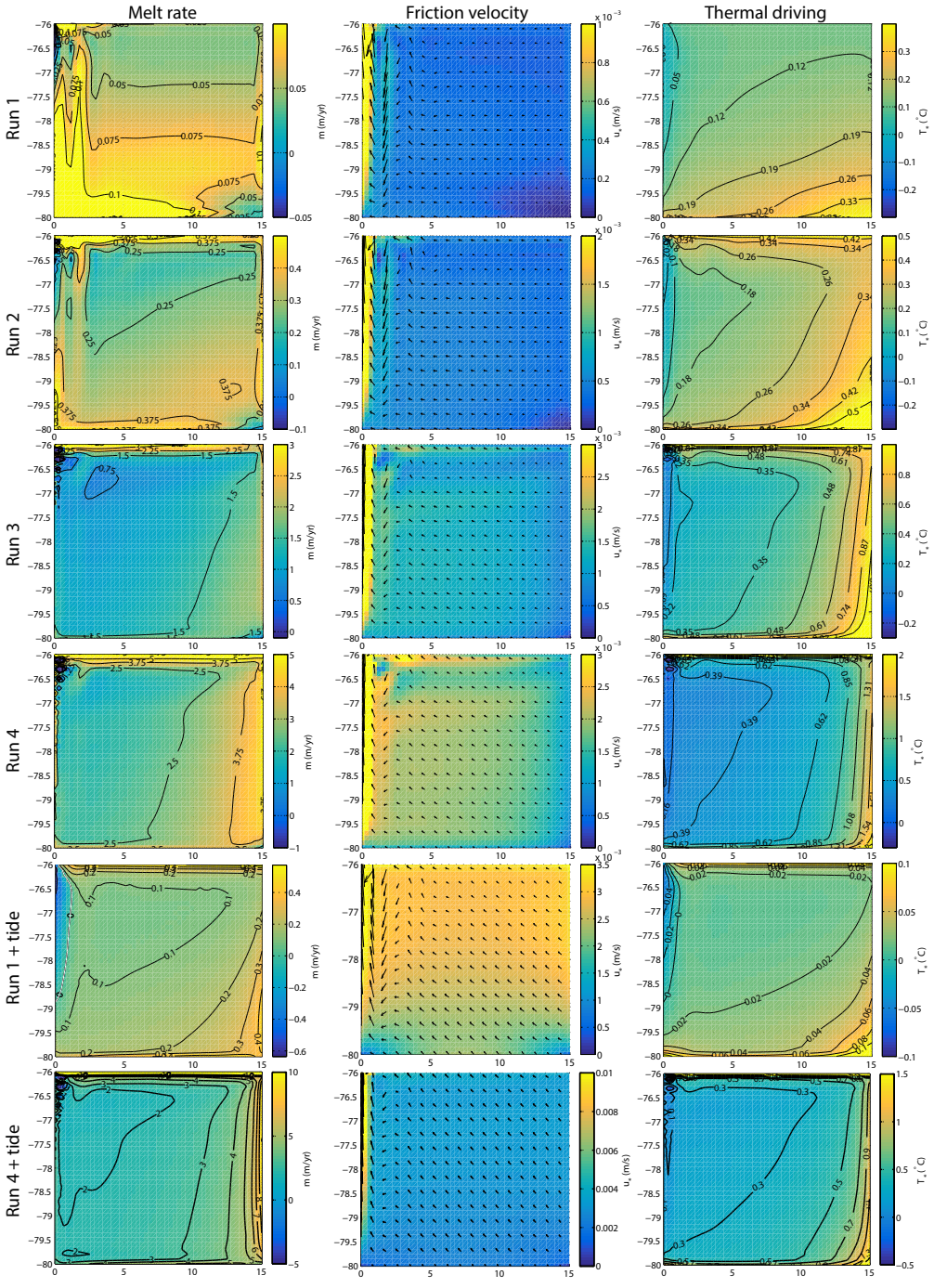

Figure 4.2: Temporally-averaged melt rate (melting for $m > 0$; column 1), friction velocity (column 2) and thermal driving (column 3) are shown for each model run. Vectors in the friction velocity plot represent the temporally-averaged flow direction and are scaled to the maximum magnitude of u_* for each plot. Run 1 represents the coldest conditions, and run 4 the warmest conditions. The fifth row (run 1 + tide) is identical to run 1 except for the addition of an analytic tide on the northern boundary. The sixth row (run 4 + tide) is identical to run 4 except for the addition of an analytic tide on the northern boundary. Note the changes in colour scale between some plots.

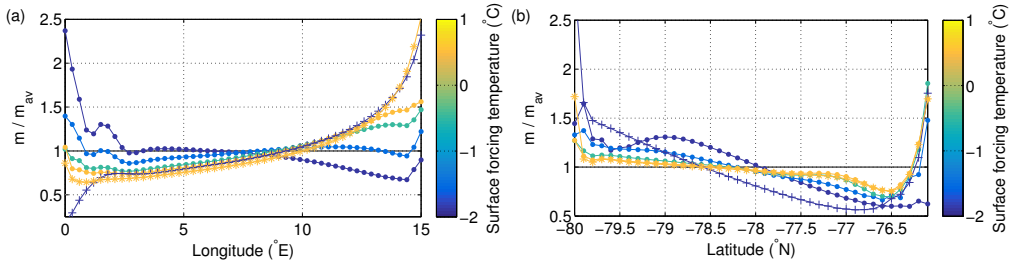

Figure 4.3: (a) Melt/freeze rate along transect A as a proportion of the area averaged melt rate for the same transect. Melting along the transect is calculated as the meridional average within the area of A (see Figure 4.1) for each point along the transect. (b) Melt/freeze rate along transect B as a proportion of the area averaged melt rate for the same transect. Melting along the transect is calculated as the zonal average within the area of B (see Figure 4.1) for each point along the transect. Transects are coloured for the temperature of surface forcing. Runs 1 through to 4 are represented with solid dots, while run 1 + tide is represented with + and run 4 + tide is represented with $*$. The horizontal black line at $\frac{m}{m_{av}} = 1$ represents where melting along the transect is equal to the transect-average melt rate.

south-west corner of the ice shelf displays weaker melting compared to the eastern boundary.

The spatial variation in melting for different cavity environments is further investigated with melt rate transects. These transects are calculated as the melt rate along each line of longitude/latitude within the bounds of the area A/B, as a proportion of the average melt rate over the total area of A/B. The areas of transects A and B are shown in Figure 4.1.

The deviation from the mean melt rate along an east-west transect near to the grounding line shifts as the surface forcing warms the ocean cavity (Figure 4.3(a)). As the cavity warms, melting at the western edge of the cavity decreases relative to the mean, while melting along the eastern edge increases relative to the mean.

The deviation from the mean melt rate along a north-south transect through the center of the cavity also displays a shift in distribution (Figure 4.3(b)). For the cold cavity, melting is strongest at the southern end of the cavity. As the cavity warms, melting close to the ice front increases, while melting in the southern half of the cavity decreases relative to the mean.

The friction velocity, u_*, is shown in the second column of Figure 4.2, and is calculated as the top layer speed multiplied by $\sqrt{C_D}$. In general, cavity circulation in the top model cells is from east to west, with strong acceleration as the flow intercepts the western boundary. At the western boundary, flow turns and increases to the north. In the coldest cavity environment (run 1), circulation in the south-eastern region is almost stationary. For the slightly warmer cavity environments (run 2), circulation increases across the ice shelf, excepting the southeast corner, which remains stagnant. However, the circulation pattern remains similar to run 1, with strong flow across the ice shelf from east to west, peaking along the western

boundary. Three interesting features appear: 1) stronger flow adjacent to the ice shelf front, 2) weaker flow approximately along the 76.5°S line of latitude, and, 3) a southward deviation in flow before flowing north along the western boundary (at approximately the 2°E meridian). These three features can be explained as follows: the buoyancy-driven circulation exiting the cavity forms a strong jet along the ice front; a small recirculation feature forming immediately southwards of the ice front at 76.5°S; the reorganisation of the flow field which occurs as a result of the recirculation feature at 76.5°S. For the warmest cavity environments (runs 3 and 4), the magnitude of circulation continues to increase; except for a band of weaker flow along the 76.5°S line of latitude, flow strengthens towards the west.

The thermal driving, T_*, shown in the third column of Figure 4.2, is calculated as the difference between the temperature and salinity at the interface and at the top model cell. For the coldest cavity environment (run 1), the spatial gradient in thermal driving is approximately aligned southeast-northwest (hotter-to-colder thermal driving), which is roughly proportional to the increasing pressure at the ice shelf base. Thermal driving is maximum in the southeast corner and minimum in the northwest. For the warmer cavity environments (run 2), the southeast-northwest thermal gradient is maintained but also superimposed with warmer waters at the ice front. For the warmest cavity environments we tested (runs 3 and 4), the thermal gradient across the ice shelf has now rotated counterclockwise to be oriented approximately west-east (warmer-to-colder thermal driving), with the strongest thermal driving being present at the eastern boundary (for the hottest cavity environment this is $T_* \approx 1.5$°C, see run 4). The increased thermal driving present on the eastern boundary is the result of stronger overturning circulation delivering hotter cavity water to the ice shelf base.

4.3.2 Experiment 2: Tidal forcing

The effects of idealised tidal forcing on the temporally averaged melt rate, friction velocity and thermal driving are shown in the fifth and sixth row of Figure 4.2. Distribution and magnitude of melting are dramatically altered, compared to the simulation with the same thermal forcing but without tidal forcing (compare run 1 against run 1 + tide and run 4 against run 4 + tide); melting is strong ($m \sim 0.5$ m yr^{-1} for the cold cavity, $m \sim 1.5$ m yr^{-1} for the hot cavity) at the deep grounding line in the southeast corner of the ice shelf and decreases in magnitude moving northwest. Melting is also strengthened along the ice shelf front. A significant patch of refreezing now forms along the western boundary of run 1 + tide. Compared to the run without tides, melting is below average in the southwest and above average in the southeast for both cold and hot cavities (Figure 4.3(a)). The north-south transect in melting for the cold cavity displays stronger than average melting adjacent to the ice shelf front and towards the grounding line, compared to the run without tides (Figure 4.3(b)). The proportional change in melting along the north-south transect for the hot cavity run with tides is very small ($\frac{m}{m_{av}}$ for run 4 and run 4 + tide are hard to distinguish).

Between run 1 + tide and run 4 + tide, the area-averaged melt rate increases ~ 24

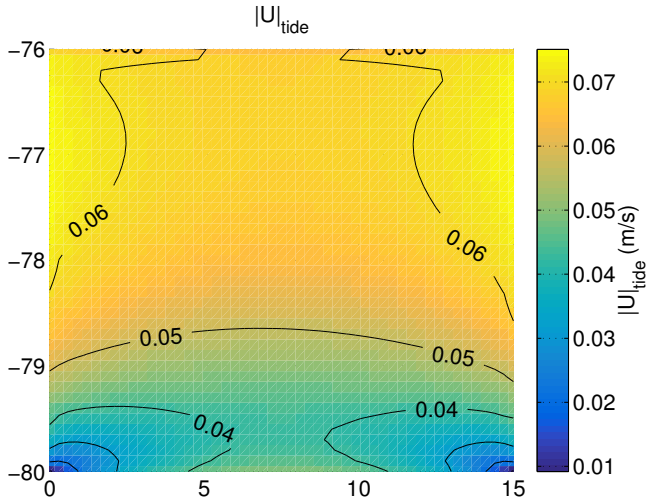

Figure 4.4: The depth-averaged RMS tidal velocity for the zero forcing + tide run, showing strongest currents across the middle of the ice shelf. The currents are temporally-averaged across an integer number of tidal cycles.

times, the area-averaged u_* increases ~ 1.2 times and the area-averaged T_* increases ~ 22 times (see Table 4.2). The run 1 + tide and run 4 + tide data, fit with a linear relationship given by $m_{tide} = \alpha_{tide} u_{*,tide} T_{*,tide}$, has a slope of $\alpha_{tide} = 7.5 \times 10^{-5}$ °C^{-1} (plot not shown). The slope of this fit is greater than that without tides (where $\alpha = 7 \times 10^{-5}$ °C^{-1}), indicating that while a hotter cavity environment will lead to higher melting, the presence of tides will further increase melting. However, adding tides leads to a larger relative increase in melting for the cold cavity (2 times as much melting) than for the hot cavity (1.2 times as much melting).

The temporal evolution of the area average melt rate (not shown) reaches a maximum every 6 hours, with a minimum between each peak. The double peak in melting results from the strongest flow between the high and low tides, while the minima in melting occur during slack water at high and low tide. This relationship repeats every 12 hours, as expected from tidal forcing with a 12-hour period.

The magnitude of friction velocity is increased for the entire domain. u_* decreases towards the grounding line, with minima located in the southwest and southeast corners of the ice shelf.

For both the experiments, the thermal driving is reduced across the entire ice shelf, compared to the runs without tides. The maximum of T_* still occurs in the southeast corner of the ice shelf, while the region along the western boundary which displays negative T_* in run 1 + tide is now increased in areal extent and magnitude.

The effect of tidal forcing on the hot cavity is less pronounced than the effect on the cold cavity. Hot cavity melting with tidal forcing increases in magnitude (see Table 4.2), but varies little in distribution (compare run 4 with run 4 + tide; Figure 4.2).

To investigate the impact that tides have on circulation, separate from the buoyancy-driven circulation, we have run a simulation with tides but without ice–ocean thermodynamics (zero forcing + tide; Table 4.1). The results of this simulation show how tidal currents are distributed. The magnitude of depth-averaged tidal currents ($|U|_{tide}$) is shown in Figure 4.4. Strongest tidal currents exist across the front half of the shelf (76°S to 78°S), and at the northwest and northeast boundaries. The southern region of the ice shelf experiences weakest tides, with the southwest and southeast corners of the ice shelf experiencing almost negligible tides. The effective friction velocity is $u_{*,tide} = 3 \times 10^{-3}$ m s^{-1}, as calculated from the area-average $|U|_{tide}$ (see Table 4.1).

4.4 Discussion

For all but the coldest cavity environments, melting along the ice shelf front (i.e. between 76°S and $\sim$ 76.25°S) is strong. This is controlled by the strong buoyancy-driven circulation influencing u_* and deflecting under the Coriolis effect as it exits the cavity. It is further magnified by the presence of hot open ocean water. The distribution of melting over the rest of the ice shelf changes as the cavity temperature warms, from a melt rate maximum along the western boundary, to a melt rate maximum along southern boundary, and eventually to a melt rate maximum along the eastern boundary.

In the coldest cavity, T_* is approximately proportional to depth, meaning that the sub-ice water is relatively constant in temperature with only the change in freezing point temperature with pressure causing T_* to increase with pressure. However, melt rate shows the strongest relationship to u_*, rather than T_*. Melting is maximum along the western boundary, where currents are strong. Concentration of supercooled meltwater along this boundary decreases T_*, and northward of 77°S, strong circulation and negative T_* drive refreezing.

The availability of heat in the hot cavity environment increases melting, leading to increased circulation and further strengthened melting, due to the extra buoyancy added to the water from the meltwater. However, in the hottest cavity environment, the distribution of melt is controlled principally by temperature distribution rather than by the circulation within the cavity.

Heat availability and friction velocity are both important for driving basal melting. However, the transition of behaviour can be summarised as moving from a heat-limited/circulation-controlled regime in a cold cavity to a temperature-controlled regime in a hot cavity. We show that understanding the thermal environment of an ice shelf cavity (and thus where the ice shelf is located in $u_* - T_*$ parameter space) can improve estimates of the principal driver of melting. For example, for a cold ocean cavity, melting is better correlated with u_*, while melting in a hot cavity is better correlated with T_*.

The effect of tidal forcing on the cold cavity environment is to increase melt magnitude and produce a distribution much closer to a warm cavity environment. How-

ever, increased meltwater production and stronger tidal mixing cools the boundary layer and reduces thermal driving, as compared to the simulation without tides (Figure 4.2). The increased melting that results from the inclusion of tides must therefore result from the strengthened currents past the ice shelf base.

The results of the zero forcing + tide show that the effects of tidal currents are strongest from the ice front southwards to approximately 78°S but almost negligible near the southern boundary corners. This result partly explains the redistribution in maximum melting away from the southwest corner for run 1 + tide; weak tidal currents diminish u_* near the southern boundary and amplify u_* closer to the ice front.

While melting is redistributed by tidal currents away from the southern boundary, the magnitude of melting at the southern boundary increases, especially towards the southeastern corner. Tidal currents are weak near to the southern boundary (Figure 4.4) but the additional tidal currents are enough to increase u_*, compared to without tides. The resultant increased u_*, despite the lower thermal driving present at the southern boundary, is enough to increase melting. The stronger circulation also drives strong melting along the ice shelf front, due to increased buoyancy-driven currents exiting the cavity and turning to the left under the influence of the Coriolis force. The change in water column thickness at the ice front likely also excites tidal currents and contributes to melting (similar to Mueller et al., 2012). The increased production of meltwater results in stronger refreezing over a larger area for the cold cavity. Strong tidal currents near the ice front and weak tidal currents near the grounding line have also been shown in realistic simulations (Mueller et al., 2012).

Melting that is controlled by strong flow past the ice shelf interface as well as the availability of heat was suggested by Holland and Jenkins (1999) and agrees with the results of various modelling studies (e.g. Dansereau et al., 2014; Gwyther et al., 2015). This study further illustrates that melting is not driven solely by ocean heat content, but also by the strength of flow along the ice shelf base. The effect on basal melting of including tides is shown to be substantial, in agreement with realistic simulations (e.g. Makinson et al., 2011; Mueller et al., 2012; Robertson, 2013). However, the changes to the distribution of melting due to inclusion of tides is largest when the thermal environment of the cavity is cold.

The spatial distribution of melting in idealised (ISOMIP-like) experiments has been investigated previously. However, these previous studies have typically simulated a different cavity environment (Dansereau et al., 2014), or have included velocity-independent turbulent exchange (Losch, 2008). In these velocity-independent simulations of a cold ocean cavity, melt rate distributions peaked in magnitude in the southeast corner, or equivalently, at the deep ice adjacent to the grounding line on the inflow side of the ice shelf. Melting displayed a decreasing gradient moving in a northwest direction and refreezing was present in the outflow region. These results were obtained by assuming constant rates of turbulent heat and salt exchange (e.g. $\gamma_T = 1 \times 10^{-4}$ and $\gamma_S = 5.05 \times 10^{-7}$; Losch, 2008). Applying a constant γ_T and γ_S in a velocity-independent melt formulation is equivalent to assuming a constant u_* in a velocity-dependent formulation. The values of $\gamma_{T/S}$ chosen in Losch (2008)

lead to an effective $u_* \approx 9 \times 10^{-3}$ m s^{-1}. The magnitude of u_* implicit in Losch (2008) is high (compared to 1×10^{-3} m s^{-1} in a similar cold cavity environment; see Figure 4.2) and equivalent to very strong RMS tidal forcing (stronger than that simulated here; $u_{*,tide} = 3 \times 10^{-3}$ m s^{-1}; Table 4.2). The strong implicit RMS tidal forcing also explains why the melt distribution of Losch (2008) is similar to run 1 + tides in this study.

A more complex parameterisation is to assume the kinematic stress across the boundary layer (which will affect the turbulent exchange of heat and salt) will vary as a function of the upper-ocean velocity. Velocity dependent and velocity independent formulations of basal melting have been compared in idealised and realistic geometry models. Comparing velocity-independent and velocity-dependent melting in a realistic geometry model showed that velocity-dependent turbulent exchange shifted the strongest melting from the deep grounding line to nearer to the outflow region (Mueller et al., 2012; Dansereau et al., 2014). Furthermore, realistic geometry studies have suggested that the melt distribution with velocity-dependent turbulent exchange is more realistic (Mueller et al., 2012; Dansereau et al., 2014). In Gwyther et al. (2015) and Chapter 3, hot and cold cavity modelling results for an idealised ice shelf cavity were presented, supporting the importance of velocity-dependent turbulent exchange for capturing a more complex distribution of melting.

Previous studies have shown an increase in melt as the ocean temperature is increased (Holland et al., 2008; Goldberg et al., 2012), however, we report on how the melt rate distribution is likely to differ depending on the thermal environment of the cavity. The spatial melt patterns and magnitudes of cold and hot scenarios, as presented here, show differences to previous studies. The melt distribution in the cold cavity features a maximum along the outflow boundary not present in other studies (e.g. Losch, 2008), which can be explained by the velocity-dependent melting formulation employed in this study. In the hot cavity, melting features strongly along the inflow boundary, unlike in Dansereau et al. (2014) where melting is strongest along the outflow boundary. This difference can be explained as a result of the velocity field responding to the strong inflow currents which are a feature of the lateral boundary conditions chosen in Dansereau et al. (2014). In this study, there is no forced inflow, and as a result the sub-ice velocity field is due to buoyancy-driven circulation.

Applying an idealised tidal forcing results in a temporally-averaged melt/freeze distribution similar to the velocity-independent melt formulation of Losch (2008). This is because the temporal-average of our idealised tidal forcing is similar to increasing the mean circulation by the root-mean-square tidal current, which in Losch (2008) is implicit by assuming constant exchange rates. The increased melting along the ice shelf front, along with the increase in magnitude of melting and freezing is a similar result to previous realistic studies (e.g. Makinson et al., 2011; Mueller et al., 2012).

This study shows a general distribution of melting for different cavity environments; maximum melting in a cold ice shelf cavity is likely to be distributed near to the outflow region, while in a hot cavity will be distributed nearer to the inflow. This

result can be applied to a real cavity which is subject to temporary incursions of warmer water. As the cavity environment becomes warmer, melt distribution will shift to a maximum near to the eastern boundary of the cavity. This analysis also allows comparison and prediction of steady state melt rate distributions for ice shelves with different cavity environments. The strongest melting may be present in the southwest of a cold cavity and in the east for hot cavity environments. The presence of strong tidal currents will likely shift the strongest melting to the inflow boundary and to the ice shelf front, although this will depend on how a more realistic ice shelf cavity geometry affects the location of strong tidal currents. Strongest melting will not necessarily occur at the deepest ice adjacent to the grounding line. Furthermore, the increase in melt resulting from tidal forcing is likely to be larger for a cold cavity environment than a hot cavity environment.

The results from the tidal simulation suggest that a relatively strong tidal wave propagating under an ice shelf will produce strong currents from the front to the middle of the ice shelf. Furthermore, tidal currents will increase mean circulation enough to shift melting to be strongest near to the inflow of ocean water. However, this may not be true for a weaker tidal regime where currents during the slack water as the tide changes may be very weak. Alternatively, in the thin water column near the grounding zone, a tidal front may protect the ice from inflowing oceanic heat and lead to reduced melting (Holland, 2008). In this case, the melt regime may return to conditions simulated in the cold cavity case with no tides, that is, strongest melting in the southwest of the ice shelf cavity. In the cavity geometry modelled here, this is likely not the case, as the depth at the southern boundary is 200 m.

4.5 Conclusions

We use an adapted version of ROMS with the three-equation parameterisation, velocity-dependent turbulent exchange, and the K-profile parameterisation of vertical mixing to conduct idealised simulations of ice shelf–ocean interaction. These idealised simulations investigate the effect on melt distribution and magnitude as the cavity environment is altered.

Melting is driven by the thermal driving and the flow velocity past the interface. However, this study suggests that a hot or cold cavity ice shelf will be located in a region of the $T_* - u_*$ parameter space where melt rate distribution is correlated more with either thermal driving or flow velocity. For example, in a cold cavity environment, melting is driven most strongly by circulation within the cavity, and so the maximum melt occurs at depth along the outflow boundary. For a hot cavity environment, melt rate distribution is correlated with thermal driving and so the region of largest melt rate migrates to the inflow boundary near to the grounding line. Hence, melting in this environment is driven by availability of heat more so than circulation. These results highlight 1) the importance of velocity-dependent turbulent exchange in the parameterisation of melting, 2) the effect strong sub-ice shelf currents have on melt distribution and 3) the likely location of strongest melting is not necessarily at the deepest ice adjacent to the grounding line, but may

be at the ice shelf side or near to the ice front. These results also suggest how melt distribution may change with a warming ocean.

Idealised tidal forcing acts to increase overall circulation and hence melting. The increased meltwater production decreases thermal driving, but not enough to lower melting. Adding tidal forcing to an ice shelf–ocean model drives stronger currents across the front half of the ice shelf area and leads to an increase and redistribution in melting. However, the effect of tidal forcing on the relative increase in melt rate is greatest for a cold ocean cavity environment. These results further justify the inclusion of velocity-dependent turbulent exchange and tides in the application of an ice shelf–ocean model to a realistic domain.

Chapter 5

TOTTEN ICE SHELF INTERANNUAL MELT RATE

5.1 Chapter Abstract

In Chapters 2-4, we explored uncertainties in the simulation of ice shelf–ocean interaction. The goal of improving the output of numerical models is to improve projections of basal melting and freezing below real ice shelves. The Totten Glacier and associated ice shelf was introduced in Chapter 1 as a dynamic source of potential sea level rise, that is displaying changing elevation and is almost certainly responding to ocean interaction.

In this chapter, we apply a numerical ocean modelling to a realistic setting of the Totten Glacier ice shelf. We use reanalysis products to force the model boundaries with records of wind, heat and salt flux, and ocean currents from the time period 1992–2007. Continental shelf processes and atmosphere-ocean exchange are shown to drive interannual variation in melting beneath the Totten and Dalton ice shelves.

The following chapter is sourced from the peer-reviewed article: Gwyther, D. E., Galton-Fenzi, B. K., Hunter, J. R., and Roberts, J. L. Simulated melt rates for the Totten and Dalton ice shelves. *Ocean Science*, 10(3):267–279, 2014. doi: 10.5194/os-10-267-2014. It has been edited for formatting and the abstract has been removed; the content remains unaltered.

5.2 Introduction

Understanding how changing ocean circulation and properties are causing increased basal melt of Antarctic ice shelves is crucial for predicting future sea level rise. The Totten Glacier (see Fig. 5.1) drains over 570,000 km^2 of East Antarctica (Rignot et al., 2008). Most of the ice sheet that drains through the Totten Glacier is from the Aurora Subglacial Basin (Young et al., 2011) and is marine based (i.e. the ice base is grounded below sea level; Roberts et al., 2011) making the region potentially

vulnerable to rapid ice sheet collapse. Weertman (1974) showed that ice grounded below sea level is inherently unstable, particularly where the bedrock slopes downwards, away from the ocean, as is the case in the Aurora Subglacial Basin (Young et al., 2011). More recent studies have indicated lateral stresses may act to stabilise ice retreat on a reverse bed slope (Jamieson et al., 2012), but the applicability of this on a broad drainage basin, where lateral stresses are lower, is uncertain.

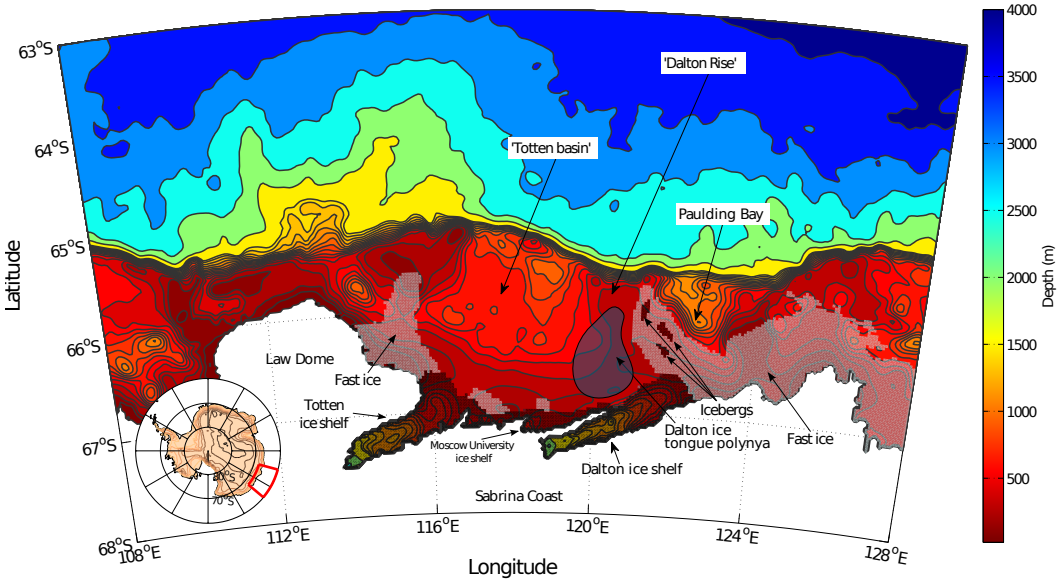

Figure 5.1: Model bathymetry and domain. The contour interval is 100 m up to 1500 m depth and 500 m up to 4000 m depth. Ice shelves and icebergs (dark shading), fast ice (bright shading), polynya (mauve shading with dark outline) and major bathymetric features are indicated. Inset shows model domain location in Antarctica.

The Antarctic ice sheet contains enough ice to raise sea level by over 58 metres (Fretwell et al., 2013). Observations of global mean sea level rise over the period 1993-2008, indicate an average rate of 2.61 ± 0.55 mm/yr, with an Antarctic contribution of 0.43 ± 0.2 mm/yr (Church et al., 2011). Projections of sea level rise have a large uncertainty in the contribution of Antarctica, due to lack of observations of ice discharge rates and surface mass balance (Gregory et al., 2013).

The ice sheet flows towards the ocean through both broad slow ice sheet flow and many fast flowing glaciers. Ice shelves form in coastal regions where the ice thickness of the ice sheet or glacier is insufficient to maintain contact with the bedrock and the ice begins to float on the ocean. An ocean-filled cavity, insulated from the atmosphere, forms beneath. The sub-ice shelf seabed can be found at depths of over 2800m below mean sea level (e.g. the deepest part of the Amery Ice Shelf cavity; Galton-Fenzi et al., 2008). The freezing point of seawater decreases with increasing pressure. Therefore, at the back of deep ice shelf cavities, the decreased freezing point of seawater provides a large potential for thermal driving of melting, leading

to melting at depth and a buoyant melt water plume (Lewis and Perkin, 1986).

Increased melting leads to the localised thinning of an ice shelf, and potentially to the acceleration of the glacier behind it, as the buttressing effect of the shelf is decreased (Dupont and Alley, 2005). An acceleration in flow rate of a glacier causes a mass budget imbalance in the surrounding ice sheet due to the longer response time of the interior ice sheet to flow change; hence the grounded ice sheet thins. For example, observations show surging, acceleration and retreat of tributary glaciers after the collapse of the Larsen A and B Ice Shelves (De Angelis and Skvarca, 2003; Scambos et al., 2004). It is this dynamic coupling between the ice shelf and glacier which makes the grounded ice sheet susceptible to oceanic changes (Dupont and Alley, 2005). The ice shelf-ocean interaction is therefore an important control on the discharge of grounded ice into the oceans and subsequently on sea level. Recent satellite observations have shown rapid and accelerated thinning of glaciers along the coastal margins of Antarctica (Pritchard et al., 2009). For example, Pine Island Glacier thinned at rates up to 6 m/yr while the Totten Glacier displayed thinning rates of 1.9 m/yr for the period 2003-2007 (Pritchard et al., 2009), three times the rate previously reported (Rignot, 2006). The high thinning rates of marine terminating glaciers suggests a common oceanic driving, for example through increased basal melting (Pritchard et al., 2012).

Glaciologically derived estimates of area-averaged basal melt rate for the Totten ice shelf are 20 ± 9 m/yr (Rignot, 2002); 26 ± 8 m/yr (Rignot and Jacobs, 2002); and 10.5 ± 0.7 m/yr (Rignot et al., 2013). These estimates are derived from satellite Interferometric Synthetic Aperture Radar (InSAR) observations of ice surface velocity and the first two are calculated as the difference in flux of ice from the Totten Glacier across the grounding line and across a flux gate 10-30 km downstream, divided by the area of enclosed ice shelf. These measurements should thus be treated as an average melt rate for the grounding line region. The latter estimate was also derived from InSAR observations, but was calculated using the volume flux divergence for the whole ice shelf area. The last estimate is equivalent to a mass loss rate of 63.2 ± 4 Gt/yr (Rignot et al., 2013). Comparatively, the InSAR estimate for the Moscow University Ice Shelf show basal melt of 4.7 ± 0.8 m/yr and a mass loss rate of 27.4 ± 4 Gt/yr (Rignot et al., 2013). It should be noted that this work defines the Dalton ice shelf as being separate to the Moscow University Ice Shelf. We define the Dalton ice shelf as the ice shelf separated from the ocean by the grounded peninsula which runs north-east from 67.2°S, 118.5°E. This is done since the grounded peninsula is likely to protect the Dalton ice shelf from oceanic influences, and will change the mass loss characteristics of the Dalton as compared to the Moscow University Ice Shelf.

These estimates show the Totten and Dalton basal melting and mass loss to be exceptionally high compared to other ice shelves in East Antarctica (Rignot et al., 2013). Other East Antarctic ice shelves that are experiencing similar basal melt rates are typically smaller ice shelves, and thus mass loss rates are smaller than the mass loss of the Totten. For example, the Wilma/Robert/Downer ice shelves have a basal melt rate of 11.7 ± 0.7 m/yr, but with an area of only 858 km^2, mass loss (10.0 ± 0.6 Gt/yr) is only 16% as large as the Totten mass loss. Furthermore, unlike

many other high melt locations, such as the Pine Island ice shelf which is estimated to have an area-averaged mass loss of 101.2 ± 8 Gt/yr (Rignot et al., 2013), no definite causal mechanisms for basal melting of the Totten and Dalton ice shelves are known.

Here we examine the temporal variability and driving mechanisms controlling the basal melt rates of the Totten and Dalton ice shelves using a numerical model. The Totten and Dalton ice shelves are prime candidates for investigation, due to their rapid thinning rates, high estimated basal melt and the limited existing research. Section 5.3 provides an overview of the Totten and Dalton ice shelf-ocean region. Section 5.4 presents different hypotheses for drivers of basal melting, and in Section 5.5 the regional circulation and heat transport model is described. Section 5.6 and Section 5.7 present the results of the modelling and a discussion on cross shelf flow and atmosphere exchange processes.

5.3 Description of region

The Totten ice shelf (centred at 67°S, 116°E) is located on the Sabrina coast in East Antarctica (See Fig. 5.1). The Sabrina coast is characterised by marine terminating glaciers, ice shelves (such as the Totten, Moscow University and Dalton ice shelves), large tracts of year-round ice adjoining the land (fast ice), extensive seasonal sea ice growth and a region of strong sea ice formation (the Dalton ice tongue polynya). The continental shelf seas are approximately 1000m deep, with the shelf break occurring between 65°S to 65.5°S in this region. The Antarctic Circumpolar Current is located in the deep abyssal waters to the north of the continental shelf break (Orsi et al., 1995). The Antarctic Circumpolar Current is composed of several water masses, with Antarctic Surface Water overlying relatively warm and salty Circumpolar Deep Water (CDW). Poleward mixing of CDW with cold and dense Antarctic waters produces 'modified' CDW or MCDW (Orsi et al., 1995), at the southern boundary of the Antarctic Circumpolar Current.

The embayed position of the Totten ice shelf, located on the eastern flank of Law Dome and with a broad continental shelf, makes it relatively isolated from the eastwards flowing Antarctic Circumpolar Current. The two main oceanic currents near to the coastal ice shelves flow westwards. The Antarctic Coastal Current (ACoC) flows within 50km of the coast and is associated with the east wind drift. The Antarctic Slope Current (ASC) is topographically controlled and is an important influence on transport across the continental shelf break (Jacobs, 1991).

A large polynya forms west of the Dalton ice shelf tongue (Massom et al., 1998). Polynyas form when strong gravity-driven katabatic winds flow down the Antarctic ice sheet and turn westwards under Coriolis acceleration, removing freshly formed sea ice. Heat is then lost from the uncovered ocean, leading to more sea ice formation and brine rejection as a latent-heat polynya. These are important as they produce large quantities of HSSW, which contribute to bottom water formation (Rintoul et al., 2001), an important driver of the global climate system (Jacobs, 2004). The easterly katabatic winds are an important controlling factor in polynya strength

(Massom et al., 1998). As the ACoC is also controlled by the strength of the easterly winds, a correlation between the strength of both the polynya and the ACoC is to be expected.

5.4 Overview of drivers of basal melting

The largest process responsible for causing ice shelf thinning is thought to be changes to the steady state distribution and magnitude of basal melting (Pritchard et al., 2012; Rignot et al., 2013; Depoorter et al., 2013). Ice shelf thinning by increased basal melt suggests increased oceanic heat available for melting at the ice shelf cavity (Holland et al., 2008; Jacobs et al., 2013). Proposed hypotheses explaining increased heat supply to ice shelf cavities include; redirected coastal ocean currents leading to increased heat content beneath ice shelves (Hellmer et al., 2012; Jacobs et al., 2011); regional upper-ocean hydrography (Hattermann et al., 2014); dynamic eddy-scale activity (Moffat et al., 2009); a link with sea ice conditions (Holland et al., 2010); polynya activity (Cougnon et al., 2013); wind-driven currents (Dinniman and Klinck, 2004); and changes in the Antarctic Circumpolar Current (Gille, 2008; Böning et al., 2008). This paper investigates the mechanisms that influence the oceanic heat supply that drives basal melting.

5.4.1 Circumpolar Deep Water intrusions

Increased heat supply for ice shelf melting has been suggested to be due to periodic incursions of modified Circumpolar Deep Water (MCDW) onto the continental shelf which can then flow along isopycnals and be delivered to the ice shelf base (Jacobs et al., 1996; Thoma et al., 2008). Observations near and beneath several Antarctic ice shelves show the signature of MCDW. In the case of Pine Island ice shelf, which is showing high melt rates, water measurements taken from an autonomous underwater vehicle show MCDW mixing with cold melt water. This indicates that MCDW is responsible for the high melt rates of Pine Island ice shelf (Jenkins et al., 2010; Jacobs et al., 2011).

In the Totten Glacier region, Conductivity, Temperature and Depth (CTD) measurements have indicated the presence of MCDW on the south side of the continental shelf break, ∼200 km from the Totten ice shelf (Williams et al., 2011). However, no observations yet exist to determine the temporal and spatial variability or causal mechanism of the MCDW incursion. Consequently, it is not yet clear whether MCDW is the water source driving melting of the Totten ice shelf.

5.4.2 Interaction with bathymetric features

Observations suggest that intrusions of warm water onto the continental shelf is highly dependent on bathymetry features (e.g. Martinson and McKee, 2012). Geostrophic eddy interaction with small scale bathymetry features can lead to enhanced oceanic

mixing via internal wave breaking (Nikurashin and Ferrari, 2010). Broad scale bathymetry features such as the shelf break (as opposed to small scale sills and ridges) can also lead to net onshore intrusion. Inertia of the along-slope water flow can carry the water up the slope and onto the shelf, depending on the curvature and orientation of the continental shelf (Dinniman and Klinck, 2004; Klinck and Dinniman, 2010). In the case of Pine Island Glacier, modelling has shown warm waters being channelled through irregular bathymetric features and submarine troughs (Thoma et al., 2008). The bathymetry in front of the Totten ice shelf is suggestive of possible pathways of MCDW intrusion onto the continental shelf. For example, Paulding Bay (see Fig. 5.1) is bordered by a low continental shelf break, possibly allowing bathymetric intrusion. The western side of the Dalton rise is another location where the deepening of the continental shelf break may allow intrusion of MCDW. Current bathymetry products of the continental shelf break and shelf proper in this region are informed by satellite gravity inversions, and have limited ship-based groundtruthing. Consequently, there is a strong need to acquire accurate ship-based and airborne bathymetry data.

5.4.3 Eddies

Eddies may also transport and mix heat across the shelf break. Observations in the western Antarctic Peninsula have characterised eddies as transporting Circumpolar Deep Water onto the continental shelf (see Moffat et al., 2009). The Antarctic Circumpolar Current is recognised as an important generator of eddies, which carry heat poleward (Rintoul et al., 2001). Closer to the continental shelf, interaction of the westwards flowing coastal current with bathymetric features, such as ridges along the shelf break may lead to eddy generation. Numerical models have shown topographic Rossby wave interaction with bathymetry is an important factor for generating eddies, which carry a significant amount of heat across the continental shelf (St-Laurent et al., 2013).

Direct modelling of eddy generation and evolution is limited by model grid resolution and bathymetry detail. Eddy-permitting flow can be simulated with horizontal grid resolutions of approximately 2-3 km (Klinck and Dinniman, 2010), however, a horizontal grid resolution of 1 km is required in order to resolve individual eddies (St-Laurent et al., 2013). The modelling work presented here (with a horizontal grid resolution of 2.5-3.5 km) is eddy-permitting, where the mean flow and associated interactions are resolved.

5.4.4 Atmospheric forcing

In analysing the source of increased heat supply to the Totten ice shelf region, we must also consider the effect of the atmospheric forcing on the ocean. Atmospheric forcing consists of transfers of momentum (surface wind stress) and buoyancy (heat and/or salt fluxes), such brine rejection in sea ice formation and polynya regions.

In some cases, local meteorological conditions favour wind stress patterns that drive

currents over the continental shelf break and onto shelf. For example, modelling of Pine Island ice shelf showed a strong correlation between flow of CDW onto the continental shelf and local temporal variations in synoptic wind stress conditions (Thoma et al., 2008).

The polynya located to the east of the Totten ice shelf produces dense High Salinity Shelf Water (HSSW). HSSW flow may interact in different ways with the local environment, and until observations are taken, modelling presents the only method to understand the implications of the polynya for the oceanography of the region. Kämpf (2005) suggested that dense water cascading down submarine canyons and off the shelf break could induce upwelling of deeper water onto the shelf, which was confirmed in numerical simulations and laboratory experiments (Kämpf, 2007). Alternatively, HSSW produced by polynya activity could be guided by the westwards flowing coastal current, directly towards the mouth of the Totten ice shelf cavity, potentially cooling sub-ice shelf waters and quenching melting.

Ice concentration observations taken by the Special Sensor Microwave Imager are used to infer heat and salt flux out of the ocean (Tamura et al., 2008). The heat flux out of the Dalton ice tongue polynya using the method of Tamura et al. (2008) is shown in Fig. 5.2(a), where a positive value indicates loss of heat to the atmosphere and formation of HSSW, and is considered as a proxy for polynya activity. A peak in polynya activity coincides with the Austral winter, due to strong wind over the region (see Fig. 5.2(a), green line) and low air temperatures. Between approximately mid-February and mid-November the polynya removes heat from the ocean. The persistence and duration of this polynya before the satellite era is unknown.

Long-term polynya activity can be analysed by considering the polynya heat flux anomaly - calculated as the difference between the heat flux and a climatological value for each month, smoothed with a Gaussian filter (the filter standard deviation is $\sigma_{\text{filter}} = 4$), as shown in Fig. 5.2(b). The climatology is calculated over the 1992-2007 period. The heat flux anomaly for the Dalton ice tongue polynya region is derived from the buoyancy flux data (see Tamura et al., 2008) used to force the open ocean surface of the model. A positive heat flux anomaly indicates above average heat loss from the ocean and stronger than average polynya activity and thus, the resulting signal is a proxy for interannual polynya strength.

5.5 Model details

A modified version of Regional Oceanic Modeling System (ROMS; Shchepetkin and McWilliams, 2005), a 3-D primitive equation finite difference model, is used to simulate ice shelf-ocean interaction. ROMS was modified to include realistic tidal forcing, thermodynamic interaction between ocean and the ice shelf (see Galton-Fenzi et al., 2012; Dinniman et al., 2007) and frazil thermodynamics (see Galton-Fenzi et al., 2012). A three-equation formulation parameterises ice-ocean thermodynamics, following Holland and Jenkins (1999).

The model domain (part of which is shown in Fig. 5.1) covers 104.5° E to 130° E

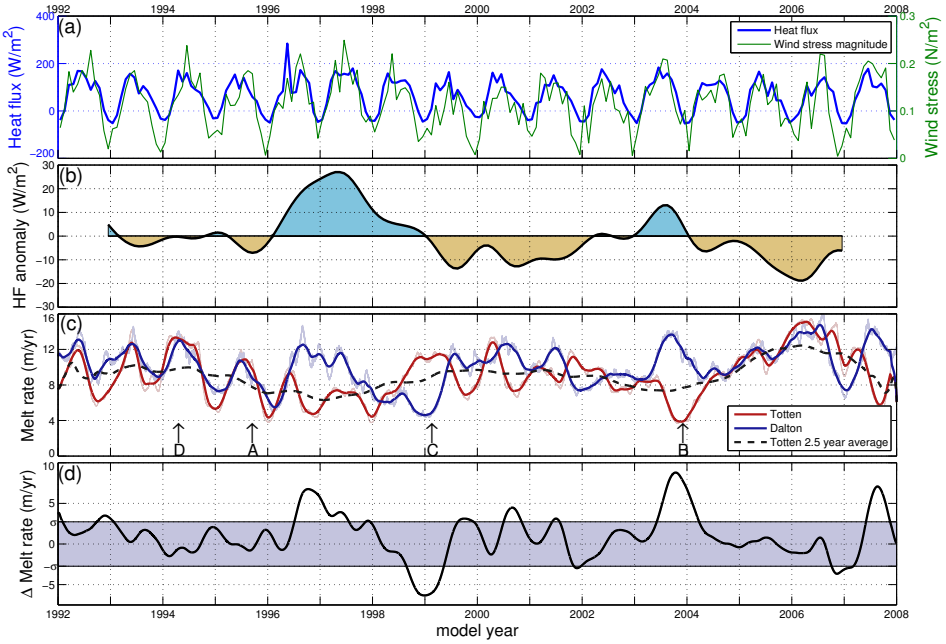

Figure 5.2: (a) Heat flux out of ocean from SSM/I observations (Tamura et al., 2008) and the magnitude of wind stress, for the Dalton ice tongue polynya. (b) Difference between monthly heat flux and climatological heat flux (calculated from 1992-2007 data) for respective months, smoothed with a Gaussian filter ($\sigma_{\text{filter}} = 4$), and referred to as the 'heat flux anomaly'. Heat flux is defined out of the ocean, so positive anomaly periods indicate stronger than average heat loss from the ocean. (c) Model melt rates for the Totten and Dalton ice shelves. The times of the snapshots in Fig. 5.5 are marked A to D. (d) Difference between melt rates of the Totten and Dalton ice shelves. A positive difference indicates Dalton melting that is stronger than Totten melting. Raw melt rates are smoothed with a 2.5-year moving average filter, ± 1 standard deviation (2.3 m/yr) of difference is shaded and years are marked for the 1st of January. In (c), light blue and light red lines are the raw Dalton and Totten melt rates, blue and red lines are the raw melt rates smoothed with a 3-month moving average filter and the dashed black line is Totten melt rate smoothed with a 2.5-year moving average filter.

and 60° S to 68° S, with a grid resolution of 2.5 km to 3.5 km and 31 terrain-following layers in the vertical. Model bathymetry in the open ocean is provided by RTOPO-1 (Timmermann et al., 2010), which in turn is based on S-2004 (Marks and Smith, 2006), a combination of the gravity map of Smith and Sandwell (1997) and the ship-based echo soundings of the General Bathymetry Chart of the Oceans (GEBCO; British Oceanographic Data Centre, 2003). Ice shelf thickness over the Totten, Dalton and Moscow University ice shelves is inferred by hydrostatic inversion of ICESat ice surface elevation measurements. The bathymetry under the ice shelves is unknown, so cavity thickness, T_C, is set to a nominal depth, $T_C = 300$m, representative of the typical thickness of an ice shelf cavity along the cavity centreline (Galton-Fenzi et al., 2008), while along the grounding line, $T_C = 0$. Within

the cavity, T_C is linearly interpolated between the cavity centreline and grounding line, except where the centreline approaches the grounding line. Here, T_C is not set, allowing a smooth interpolation from grounding line to centreline. The choice of T_C along the centreline is justifiable, as uncertainty in this depth should only affect the spatial distribution of melt/freeze regions (Holland et al., 2008) and not open ocean circulation and heat transport into the cavity. Furthermore, the agreement between modelled basal melt rates and glaciological estimates (see Section 5.6.1) attests to the scale of the ocean cavity being of the correct order. Fast ice is included from the maps of Fraser et al. (2012) with a 5 m draft (Massom et al., 2001).

There are several sea ice models available for integration into ROMS (Budgell, 2005). However, sea ice production from coupled sea ice models is sensitive to the representation of grounded icebergs (Kusahara et al., 2010), leading to the possibility of poor representation of polynyas forming in the lee of grounded icebergs (such as the Dalton ice tongue polynya). Consequently, we parameterise sea ice formation from Special Sensor Microwave Imager (SSM/I) observed ice concentration for the period 1992-2007 using the heat and salt flux algorithms of Tamura et al. (2008).

Currents, heat and salt fluxes on the lateral boundaries are relaxed to monthly values from the ECCO2 reanalysis product (Menemenlis et al., 2008). The surface is forced with wind stress from COREv2 (Large and Yeager, 2009) and the buoyancy fluxes of Tamura et al. (2008).

The model was run for 32 years; comprising of 16 years of repeated 1992 forcing, followed by observed forcing for the period 1992-2007. After the 16 year spinup phase, the model was observed to have attained a pseudo-steady state as shown by the total ocean heat content for the spinup phase in Fig. 5.3.

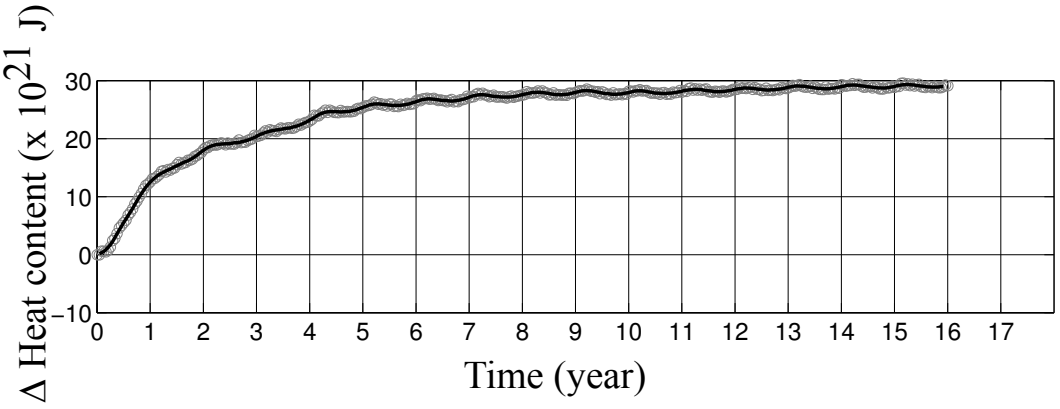

Figure 5.3: The total ocean heat content within the model for the spinup period. In the spinup, the model is run with 1992 forcing repeated for 16 years.

5.6 Results

5.6.1 Computed ice shelf melt rate

Melting and freezing at the ice-ocean interface is calculated for the ice in the domain. Area-averaged melt rates for the Totten and Dalton ice shelves are shown in Fig. 5.2(c), while the spatial melt rate distributions are shown in Fig. 5.4. These are at the same times as the corresponding circulation patterns in Fig. 5.5. In Fig. 5.2(c), the smoothed interannual Totten melt rate is shown by a dashed black line, and is calculated by smoothing the area-averaged Totten melt rate with a 2.5-year moving average filter. The area of the Totten and Dalton ice shelves, which are used for calculating the area-averaged melt rates and mass loss, are defined as 5402 km^2 and 5113 km^2, respectively.

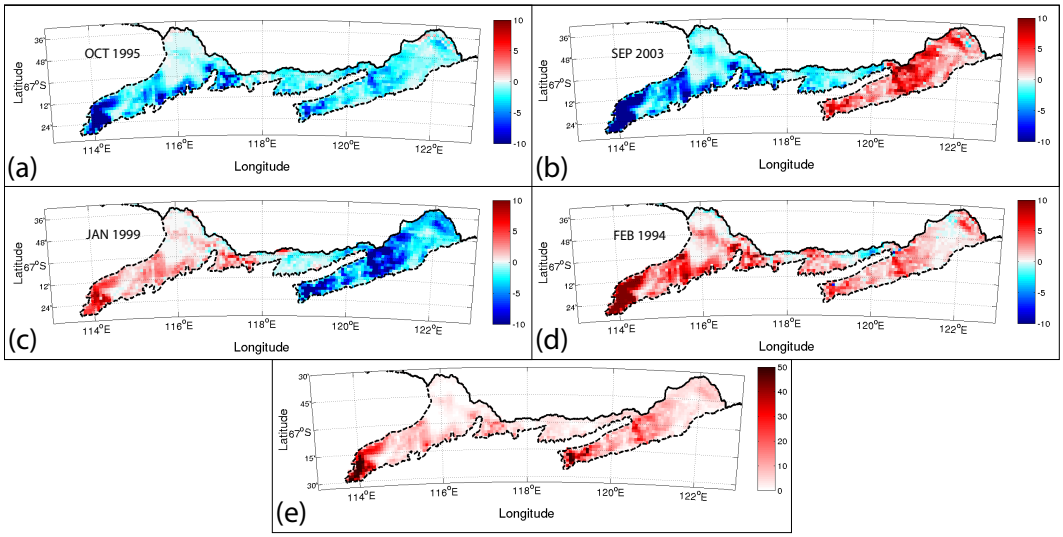

Figure 5.4: The anomaly from the mean melt rate over the period 1992-2007 is shown at (a) October 1995 (b) September 2003 (c) January 1999 (d) February 1994. (e) The mean melt rate over the period 1992-2007. Larger positive numbers indicate higher melting.

For both the Totten and Dalton ice shelves, simulated whole ice shelf area-averaged melt rates range from 4 m ice/yr to 16 m ice/yr. The Totten ice shelf area-averaged melt rate (mass loss) averaged over the period 1992-2007 is modelled as 9.1 m ice/yr (44.5 Gt ice/yr), which compares well to the most recent estimate of area-averaged melt rate of 10.5 ± 0.7 m/yr (Rignot et al., 2013). The interannual variability in the Totten melt rate (shown as the dashed black line in Fig. 5.2(c)) has a mean range of 5.7 m ice/yr (mass loss of 26 Gt ice/yr), while the seasonal variability has a mean range of 3.4 m ice/yr (mass loss of 17 Gt ice/yr). The area-averaged melt rate in the grounding line region is likely to be among the highest rates found under the Totten ice shelf. The model area-averaged melt rate in the Totten grounding line

region ranges from 16 m ice/yr to 45 m ice/yr over the 1992 to 2007 period, with an average value of 28 m ice/yr, in good agreement with the estimates from InSAR (20 ± 9 m/yr; Rignot, 2002; 26 ± 8 m/yr; Rignot and Jacobs, 2002).

While there are no glaciological estimates of melt rate for the Dalton ice shelf, the model area-averaged Dalton melt rate (mass loss) for the 1992-2007 period is 10.1 m ice/yr (46.6 Gt ice/yr). The strength of basal melt of the Dalton ice shelf, similar in magnitude to the Totten ice shelf, suggests that this region is also important for the Antarctic mass balance budget.

5.6.2 Ocean circulation features

Simulated model currents are shown in Fig. 5.5(a-d). We find four different atmospheric and ocean circulation regimes, and subfigures in Fig. 5.5 are chosen at times representing these regimes. The model adequately reproduces the westwards flowing ACoC with maximum transport during periods of strong easterly winds (see Fig. 5.5(a)), and very low transport during weak easterly winds (see Fig. 5.5(d)).

The ASC is also reproduced, flowing westwards along the continental shelf break (see Fig. 5.5(b)). The current is channelled by bathymetric features, such as where the shelf break curves north-west at 116° E, 64.5° S and approximately flows between the 2000 m and 2500 m isobaths. Consequently, the ASC is differentiated from coastal flow associated with the ACoC by both the zonal location and temperature of water within the flow. Currents for the ASC can be as high as 20 cm s^{-1}, but have a mean flow of approximately 5 cm s^{-1}. These model simulated currents agree well with the sparse nearby observations of Bindoff et al. (2000) and Williams et al. (2011), which reported observed currents of approximately 2-15 cm s^{-1} and 2.3-6.4 cm s^{-1}, respectively. Modelling studies of circum-Antarctic ASC transport predict similar velocities (Mathiot et al., 2011).

The bathymetry of the continental shelf break acts to guide flow onto the shelf. The ASC interacts with several barriers as it flows westwards through the model domain. The eastern edge of the rise located at 122° E, 66° S, henceforth named 'Dalton rise' can act to guide water southwards towards the mouth of the Dalton ice shelf. West of the Dalton rise, a large basin with an average depth of 750 m exists, henceforth named the 'Totten basin'. Interaction of the westwards flowing ASC with the the western edge of the Dalton rise generates a southwards flowing jet clockwise around the Totten basin. This interaction, which is dependent on the meridional location of the ASC front, floods the Totten basin with warmer water, supplying heat that is available to drive the melting of the Totten ice shelf.

Observations to support these model results do not exist, as the region is covered by sea ice for much of the year. This makes long term estimation of sea surface currents by satellite observation impossible, and ship-borne observations sparse and difficult to acquire.

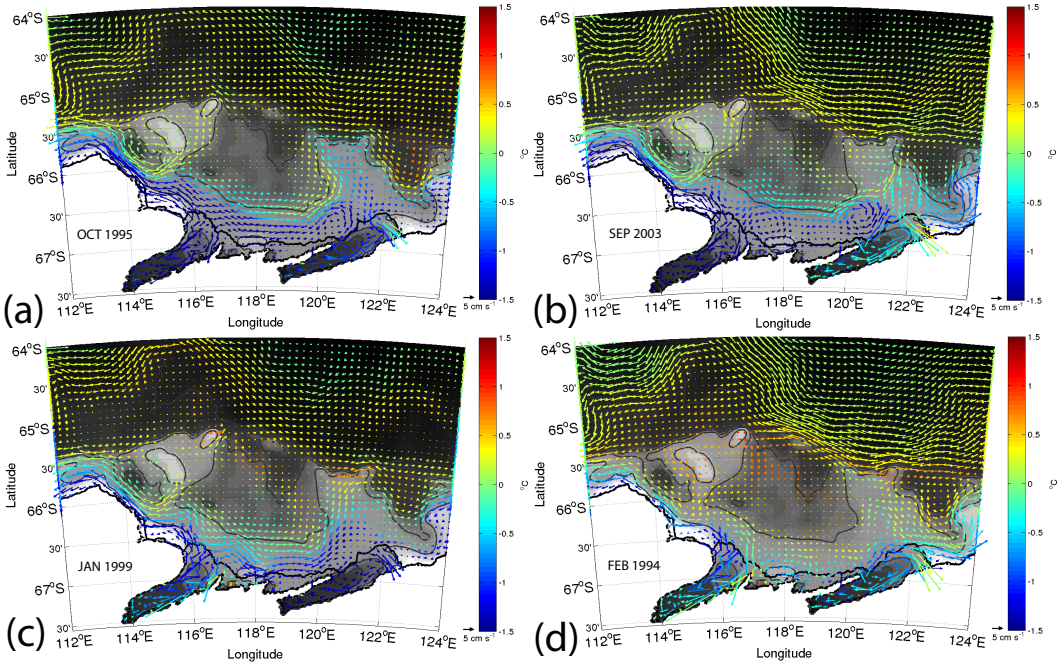

Figure 5.5: Simulated column averaged currents (excluding the surface layer), where the vectors are coloured for mean column temperature, and scaled according to the reference vector. (a) October 1995. Strong winds drive polynya activity and the ACoC, inhibiting heat flow to the Totten ice shelf. There is no flow over the Dalton rise. (b) September 2003. Strong polynya activity increases HSSW production, preventing warm water entry to the Totten ice shelf cavity and decreasing melt rates. Flow over the Dalton rise supplies heat for melting to the Dalton ice shelf. (c) January 1999. Polynya activity and ACoC are weak, allowing heat supply to cause melting of the Totten ice shelf. There is no flow over the Dalton rise, so Dalton ice shelf melt rates drop. (d) February 1994. Polynya activity and ACoC are very weak, allowing warm inflow to Totten ice shelf. Flow over the Dalton rise can increase melting of Dalton ice shelf.

5.6.3 Heat

The temperature at each layer of the model generally decreases polewards. The water that makes up the ASC is typically between 0 °C to 0.4 °C, though at several points during the 1992-2007 time period, the temperature rises to approximately 0.5 °C. The water that makes up the ACoC (-1 °C to -0.5 °C) is cooler than the ASC, as a result of mixing with cold meltwater from glaciers and ice shelves, and heat lost to the atmosphere.

Model output shows vertical water structure at the shelf break generally composed of relatively warm and salty CDW (with temperatures warmer than 1 °C and salinity approximately 34.7) overlayed with fresher and cooler Antarctic Surface Water (temperatures of ∼-2 °C and salinity of 34.2). Flow is mostly barotropic along

the shelf break except for baroclinic bottom-intensified flows at areas of changing bathymetry (such as the Dalton rise).

On the Totten region continental shelf, the water masses include slightly cooler but salty CDW (MCDW formed through mixing with shelf waters); this is overlayed by cold and fresh Antarctic Surface Water; while along the coastline, a seasonally varying cold and salty HSSW (with temperatures of ∼-2 °C or less and salinity of 34.7 or greater) flows westwards. On the shelf, model output shows the westward flow of HSSW is bottom-intensified and can entrain surface waters with it. The flow of the ACoC is generally surface-intensified and carries meltwater from the Dalton ice shelf and ice tongue westwards, however, these two flows can combine to form approximately-barotropic westward flow. A large clockwise recirculation feature forms in the Totten basin. This feature, which is surface intensified, carries heat clockwise from the shelf break towards both major ice shelves, and is composed of water with temperature between -0.2 °C to 0.4 °C and salinity of 34.5 to 34.6.

5.7 Discussion

Model results show variability in melt rate over the course of each year. However, the interannual Totten melt rate, the dashed black line in Fig. 5.2(c), shows variation from high to low melt rate and vice versa, with a ∼2-3 year period. The ∼2-3 year modulation of melt rate signal is noticeable as an increasing annual average melt between 1992 to 1994 (most visible in the 3-month Totten melt rate, shown as the red line in Fig. 5.2(c)), 1998 to 2002, 2004 to 2007 and decreasing annual average melt between 1994 to 1998 and between 2002 and 2004. This pattern of increasing and decreasing melt repeats over the 1992-2007 period. However, there is no overall trend (over the 1992-2007 period) in Totten ice shelf melt discernible above the ∼2-3 year melt variation. Thus, we focus the analysis on understanding the processes governing simulated interannual variability in melt rates.

Satellite-derived estimates of ice shelf thinning indicate that for the period 2003-2008 thinning of the Totten ice shelf was the fourth highest in Antarctica (Pritchard et al., 2012). Over the period 2003-2007, the model area-averaged melt rate increases to its highest value, in agreement with an ice shelf that is rapidly thinning.

Oceanic heat is supplied to both ice shelves across the continental slope. However, variability in heat supply at the ice shelves is also dependent on the nearby Dalton ice tongue polynya. HSSW produced by the polynya can flow westwards, reducing supply of heat into the Totten ice shelf cavity. We proceed by examining model currents and atmosphere-ocean exchange together with variability in ice shelf melt rate.

5.7.1 Atmosphere-ocean exchange

Strong katabatic winds that drive polynya activity, are also partly responsible for driving the ACoC. Generally, as polynya activity increases from March to April,

large quantities of HSSW are formed in the model. When the polynya is strongly active, the ACoC is also strong and the resulting westward flow directs most of the HSSW towards the Totten ice shelf. As polynya activity decreases in August, production of HSSW decreases, allowing warm slope front current (which flows across the continental shelf break and into the Totten basin), access to the ice shelf cavity to drive high melt of the Totten ice shelf.

Times when HSSW production and ACoC are strong leads to cold, dense HSSW entering the ice shelf cavity and decreased melting. However, the timing of the minimum of Totten ice shelf melt (generally in December) lags the peak in polynya activity and HSSW production in June (compare Fig. 5.2(c) and Fig. 5.2(a)). Increasing polynya activity causes the rate of change of melt rate to become negative and so the melt rate passes through a local maximum. The melt rate continues to decrease until polynya activity decreases, at which point the rate of change of melt rate becomes positive. The melt rate then passes through a local minimum and increases. The lag between polynya maximum and Totten melt minimum is created because the bulk volume of water below the ice shelf requires time to cool as HSSW is added and time to heat up as warm water is added. The Dalton ice shelf exhibits a similar temporal pattern of melt rate as the Totten ice shelf, suggesting that polynya activity is an influential factor on Dalton melt rate as well.

The heat flux anomaly for the Dalton ice tongue polynya region is shown in Fig. 5.2(b). Here, a positive signal indicates stronger than average heat loss to the atmosphere and stronger HSSW production.

From 1993 to 1995, the heat flux anomaly is negative during the middle of the year, suggesting weaker peak polynya strength. Consequently, both ice shelves display strong melting. From 1996 to 1998, the heat flux anomaly is strongly positive, leading to strong HSSW production and the Totten progressively decreasing in melt rate during this period. From mid-1999 to mid-2002, the heat flux anomaly is negative and consequently, HSSW production drops and oceanic heat supply increases to both ice shelves. Annual average melt is thus higher for this period than for the 1996-1998 period when the heat flux anomaly was strongly positive. From late-2002 to 2004, the heat flux anomaly is weakly positive, coinciding with weakened melt rates. For mid-2004 and from 2005 to 2007, the heat flux anomaly is again strongly negative, leading to reduced production of HSSW and increased melt as heat supply increases. The years with a strong seasonal variation in melt rate (see 1992 through to 1996) are years when atmosphere-ocean exchange (in the form of heat loss to the atmosphere) is the dominant mechanism modulating seasonal variation in the melt rate. Other years, such as 1998 and 2003, display a more complex melt rate evolution that is likely a combination of atmospheric forcing and melting caused by a time-dependent warm water source.

The seasonal changes in atmosphere-ocean fluxes explains the seasonal evolution of melt of both ice shelves, while the heat flux anomaly explains the interannual trend in melt rate of both ice shelves. However, there are several periods when the melt rate of the Totten and Dalton ice shelves fluctuate quite differently from each other, indicating melting not driven solely by polynya activity.

5.7.2 Shelf exchange processes and heat supply for melting

The primary source of heat for melting is supplied across the continental shelf. Bathymetry is important for controlling intrusion of warm water by guiding the slope current. Model results show that regional topographic features (the Dalton rise and Totten basin) act to guide water onto the continental shelf. These features are regions of intermittent warm inflow. The mechanism by which the flow of the ASC can be diverted by bathymetry is probably different for each topographic feature.

Geostrophic flows tend to conserve potential vorticity f/H, where f is the Coriolis parameter (which varies with latitude) and H represents the water depth, leading to the tendency of geostrophic flows primarily following isobaths. If a change in bathymetry is encountered, resulting flow will tend to divert to a different latitude to counter the change in depth. In the model results, we see this by the poleward current generated as the ASC interacts with the edge of the Totten basin. The narrow current formation is supported by idealised modelling studies, which suggest a significant onshore flow is generated by interaction with flow along the shelf break and a trough (St-Laurent et al., 2013).

Melting of the Dalton ice shelf is strengthened by occasional flow of warm water into the basin of Paulding Bay, east of the Dalton rise. Model currents suggest counter-clockwise circulation forming in Paulding Bay when the ASC impacts with the north-eastern tip of the Dalton rise. The resulting circulation is onto the Dalton rise and into the ice shelf cavity (see Fig. 5.5(b)).

The difference between the simulated Totten and Dalton melt rates is shown in Fig. 5.2(d). A positive value indicates the Totten melting is lower than Dalton while a negative value indicates Dalton melting is weaker than Totten. The signal is smoothed by a 6-month moving average and $\pm$ 1 standard deviation is shaded. A difference greater in magnitude than 1 standard deviation indicates periods when the melt rates of the Totten and Dalton ice shelves are significantly uncorrelated. Since polynya activity drives the melt rate signal on a seasonal timescale, significantly different melt rates indicate times when the melt rate of at least one of the ice shelves is not purely driven by polynya activity.

Late 1996, late 2000, late 2003 and late 2007 are times when there is strong supply of heat to the Dalton ice shelf, but not to the Totten ice shelf (See Fig. 5.2(d)). During these times, oceanic currents supply heat over the Dalton rise only to the Dalton ice shelf, but polynya activity and formation of cold, dense HSSW is strong enough to limit Totten melting (see Fig. 5.5(b)). Circulation also shows cold Dalton melt water leaving the cavity and flowing westwards to the Totten ice shelf cavity.

Late 1998, early 1999 and late 2007 are times when the Totten ice shelf is strongly melting but the Dalton ice shelf is not. Polynya activity at these times is weaker than average, leading to lower rates of HSSW production. Model circulation at these times show weak flow of HSSW to the Totten ice shelf (see Fig. 5.5(c)). Warm water that intrudes into the Totten basin can consequently enter the ice shelf cavity and drive increased melting. Weaker westwards ACoC flow results in HSSW flowing into the nearby Dalton ice shelf cavity, decreasing Dalton melting.

5.7.3 Melt rate forcing by a combination of polynya activity and circulation

The melt rates displayed by both the Totten and Dalton ice shelves are a complex combination of a seasonal signal with occasional periods of very high and very low melt. Comparing melt rate and polynya activity, as shown in Fig. 5.2(c) and Fig. 5.2(b), we see that in general, periods of lower melt are correlated with periods of stronger polynya activity. However, there were several short periods when ocean circulation features caused the melt rate of the Dalton and Totten ice shelves to be out of phase. This suggests that a combination of atmosphere-ocean exchange and shelf break flow mechanisms is required to fully explain the melt rate of the Dalton and Totten ice shelves.

We propose a set of four main states of circulation and polynya activity, that drive melt of the Dalton and Totten ice shelves. These four states describe the configuration of on-shelf flow and polynya activity, and explain the seasonal and interannual variation of the melt rate of the Totten and Dalton ice shelves. These states are described as follows:

- State A: The meridional position of the ASC means that it interacts only with the western edge of the Dalton rise. The resulting jet flows southward into the Totten basin, following the isobaths clockwise until it rejoins the ASC north of Law Dome. The polynya and ACoC are strongly active, causing HSSW to flow into the Dalton ice shelf cavity and westwards to the Totten ice shelf cavity inhibiting melting of both ice shelves. This state is illustrated in Fig. 5.6(a) and shown in model currents in Fig. 5.5(a) and melt rate anomaly distribution in Fig. 5.4(a).

- State B: Polynya activity is strong, but now the ASC interacts with the bathymetry offshore of the Dalton rise, which gives rise to a warm current over the Dalton rise, directly to the mouth of the Dalton ice shelf. The increased melting leads to a strong meltwater outflow westwards towards the Totten ice shelf, inhibiting melting of the Totten. The Totten ice shelf shows very low melt rates, while the Dalton ice shelf displays strong melting, as illustrated in Fig. 5.6(b) and shown in model currents in Fig. 5.5(b) and melt rate anomaly distribution in Fig. 5.4(b).

- State C: Weak polynya activity and ACoC strength leads to reduced HSSW flow to both the Totten and Dalton ice shelves. The ASC only interacts with the western edge of the Dalton rise, generating a warm current into the Totten basin, which drives strong Totten ice shelf melting. Since the Dalton ice shelf has very little warm inflow, the lowered HSSW production is enough to inhibit melting. This state is shown in Fig. 5.6(c) and shown in model currents in Fig. 5.5(c) and in melt rate anomaly distribution in Fig. 5.4(c).

- State D: Polynya activity and ACoC strength is much weaker than in States A and B. As a result, HSSW production is lowered and transport of dense, cold

water to both the Dalton and Totten ice shelves decreases. The ASC interacts with the Dalton rise, leading to a warm currents flooding the Totten and the Dalton ice shelves. Both ice shelves thus display high melting, but the weak ACoC means that Dalton melt water (which now flow eastwards) does not limit Totten melting as in State B. This state is illustrated in Fig. 5.6(d) and shown in model currents in Fig. 5.5(d) and in melt rate anomaly distribution in Fig. 5.4(d).

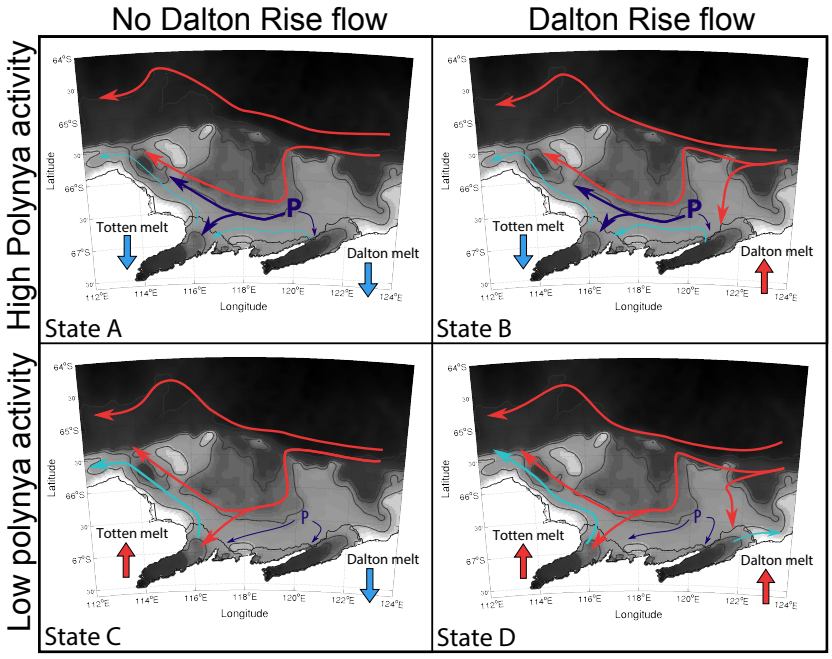

Figure 5.6: ASC (light red line), HSSW (dark blue line) and ISW (light blue line) are shown for; States A): Here, polynya activity is strong (as shown by a bold "P"), but the ASC only enters the Totten basin. Consequently, both ice shelves show lowered melt rates. B): polynya activity is strong, however the ASC comes onshore on both sides of the Dalton rise, leading to increased Dalton ice shelf melt rates. HSSW produced by the polynya and Dalton ice shelf melt water combine to lower Totten melt rates. C): polynya activity is weak (as shown by a thinner "P") and warm water only flows into the Totten basin. Consequently, the Totten ice shelf displays strong melting, while the Dalton ice shelf displays weak melting. D): polynya activity is weak and warm water on-flow over the Dalton rise and into the Totten basin lead to high melt rates for both ice shelves.

The interactions described by these four states, represented in Fig. 5.7, summarise the melt rate controls of the Dalton and Totten ice shelves. This interaction chart shows the strong negative impact of polynya activity and ACoC strength on heat supply to both ice shelves. Warm water intrusions that flow over the shelf break can interact with the shelf bathymetry and supply heat to either ice shelf, which will result in enhanced basal melting. If heat is supplied to the Dalton ice shelf,

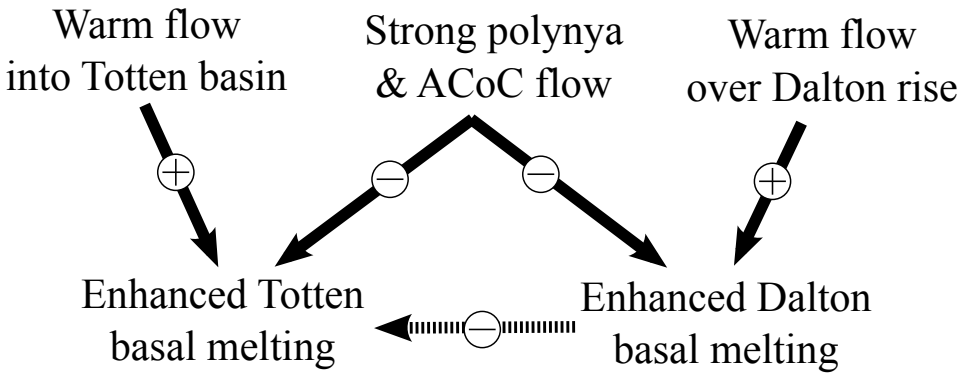

Figure 5.7: The interaction between the Totten and Dalton ice shelves, the Dalton ice tongue polynya and on shelf flow is summarised. A negative interaction is shown by $\ominus$, while a positive interaction is shown by $\oplus$. Strong polynya and ACoC flow has a negative impact on warm water supply to both ice shelves, while warm water flow into the Totten basin and over the Dalton rise has a positive impact on basal melting of the Totten and Dalton ice shelves, respectively. Increased basal melting of the Dalton ice shelf can have a strong negative affect on the Totten ice shelf. The dependence of this last interaction on strong ACoC flow is shown by the dashed line.

increased melting may lead to a decrease in heat supply for the Totten ice shelf (via outflow of cold Dalton melt water).

These interactions provide a hypothesis describing likely causes of melting of these under-researched ice shelves. A similar mechanism has been proposed linking basal melt of the Mertz Glacier Tongue and a nearby polynya (Cougnon et al., 2013).

This is also the first evidence of the interaction between two ice shelves, where the melt rate of one ice shelf affects the melt rate of the other. This indicates that the melt rate and glaciology of the Totten ice shelf cannot be studied in isolation from the Dalton ice shelf.

5.8 Conclusion

Remote sensing observations show thinning of the Totten Glacier and suggest strong basal melting of the Totten ice shelf, driven by changing ocean conditions as the most likely explanation. Previous studies have indicated that enhanced exchange of heat across the shelf break is a major cause of increased basal melting (See for example Jacobs et al., 2013). This study shows that, along with exchange of heat across the shelf break, atmosphere-ocean interaction processes on the continental shelf can modify oceanic heat supply to ice shelves, and modulate basal melting.

Dense water formation in the Dalton ice tongue polynya strongly modulates the

seasonality of melting for both ice shelves. Melting of the Totten ice shelf is increased when the interannual strength of the Dalton polynya is below average, and vice versa. The Dalton ice shelf melt rate is primarily controlled by intrusions of warm water across the Dalton rise and into the ice shelf cavity. Simulated area-averaged melt rates for the Totten ice shelf agree well with recent glaciological estimates, and suggest the Dalton ice shelf, like the Totten, as being a region of high basal melting.

Furthermore, this study suggests important evidence for the interaction between two ice shelves, where the melting of one directly influences the melting of the other. Lastly, strong interannual variability in heat supply to the ice shelves and subsequent melt rates suggest that observations will need to be long to correctly determine attributable mechanisms.

This is the first such modelling study of this region, and provides valuable information for directing future observations.

Chapter 6

TOTTEN ICE SHELF SENSITIVITY STUDIES

6.1 Chapter Abstract

In Chapter 5, the thermodynamic interaction between the Southern Ocean and the Totten Glacier ice shelf was investigated using a numerical ocean model with realistic forcing. The interannual variation in melt rate over the period 1992–2007 was linked to regional air-sea and cross-shelf exchange. Interaction between the atmosphere and the ocean at the nearby polynya forms cold dense water, which limits the inflow of warmer off-shelf waters, while the nearby Dalton ice shelf releases meltwater, cooling the Totten Glacier ice shelf cavity. These results show the important relationships between the ice shelf and the regional oceanography.

In this chapter, key uncertainties in regional models of the Totten Glacier Ice Shelf ocean cavity are investigated. The geometry comprised of the ice shelf cavity, the bathymetry and the ice draft, are less observed compared to other high melt rate ice shelves, such as Pine Island Glacier ice shelf. This chapter quantifies, using sensitivity studies, how uncertainty in the ice shelf cavity geometry may change melting spatial and temporal distributions and associated magnitude. The sensitivity of melt to ocean forcing is investigated. And, the intrinsic variability in melting, which results from internal processes as opposed to changes in external forcing (as simulated in Chapter 5), is also explored.

6.2 Recent observations of the Totten Glacier region

The Totten Glacier region has been the focus of two recent remote sensing studies. The first study investigated the change in surface elevation of the Totten Glacier ice shelf over the period 1994–2012 using satellite radar altimetry (Paolo et al., 2015). The second study used airborne geophysics to produce the most comprehensive compilation of bathymetry and ice thickness of the Totten Glacier ice shelf to-date

(Greenbaum et al., 2015).

Ice shelf surface elevation change indicates thinning, which can often be caused by enhanced basal melting. Linear trends in ice shelf elevation change over the period 2003–2007 were detected by the laser altimeter aboard ICESat (Pritchard et al., 2009). The ICESat measurements of the Totten Glacier ice shelf indicated an average thinning rate of 1.9 m yr^{-1} over the four year period. Paolo et al. (2015) combined three satellite altimetry missions to form an 18 year long record, spanning 1994–2012. These results corroborate with Pritchard et al. (2009), showing a thinning signal over the period 2003–2007. However, the thinning signal from 2003–2007 is not representative of the elevation change over the entire measured period. The linear trend over the 1994–2012 period (fitted between the end points of a polynomial fit) is 2 ± 7.5 m $decade^{-1}$ (Paolo et al., 2015). Since the fit to the longer time record does not have a trend significantly different from zero, it is impossible to say from this analysis whether the Totten Glacier ice shelf is in positive or negative mass balance.

There are, however two main problems with this analysis: 1) limitations in the analysis procedure such as exclusion of any area within 3 km of the grounding line and discretisation of data into large grid cells, and 2) coverage of only 50% of the Totten ice shelf area. Aside from doubt over the accuracy of the published thinning rates, Paolo et al. (2015) make no effort to describe the interannual variation present in Totten Glacier ice shelf thinning. Visible in the thickness change measured by Paolo et al. (2015) is a quasi-sinusoidal signal with a period of approximately 3-4 years. There was peak mass gain (leading to elevation rise) in 1998, 2002, 2005 and 2010; and peak mass loss (leading to loss in elevation) in 2000, 2004 and 2008. If the cyclic nature of this signal is linked to variations in basal melting, an ocean model would be the prime tool to investigate changes in basal melt.

The geometry of the cavity beneath an ice shelf is important for controlling how much heat is available to drive basal melting. Greenbaum et al. (2015) published high-resolution maps of the Totten Glacier ice shelf, where ice thickness was measured from airborne ice-penetrating radar and bathymetry, was inferred from gravity and magnetic measurements. Furthermore, Greenbaum et al. (2015) present the discovery of a channel, located on the eastern side of the ice shelf mouth, which they suggest is a connection between the open ocean and the cavity. They suggest this may be a source of warm inflow water, as the canal entrance is deeper than previous measurements of off-shore MCDW, allowing dense flow to enter the cavity and drive high melt rates.

The geometry of Greenbaum et al. (2015) represents a large improvement over the previous cavity geometry (Timmermann et al., 2010; Gwyther et al., 2014), but raise several questions which can be investigated with our ocean model. Firstly, what impact does the improved geometry have on mean melt rate across the Totten Glacier ice shelf? Secondly, what is the impact of the canal on the Totten Glacier melt rate?

The sensitivity to oceanic forcing, and the contribution to melt rate variation from internal variability can both be investigated with our ocean model. The questions

raised by Paolo et al. (2015) and Greenbaum et al. (2015) can also be addressed by using an ocean model of the Totten Glacier to test the sensitivity different cavity geometry.

6.3 Totten ice shelf cavity ocean model

To test the sensitivity of the Totten Glacier Ice Shelf system to changes in cavity geometry, several models will be run. The 3 model runs employ slightly different cavity bathymetry and ice draft. The difference between the bathymetry and the ice draft, the water column thickness, is shown in Fig. 6.1. The bathymetry and ice draft are shown in Fig. B.1 and Fig. B.2.

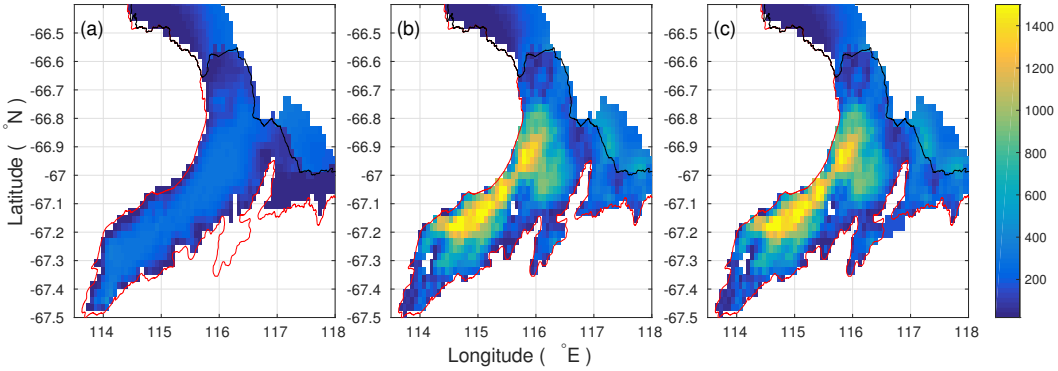

Figure 6.1: The water column thickness (m) for the (a) original bathymetry from Gwyther et al. (2014), (b) ICECAP bathymetry, and (c) ICECAP bathymetry with entrance canal. The red and black lines, sourced from the MODIS Mosaic of Antarctica (Scambos et al., 2007), show the grounding line and coastline, respectively.

The first model (see Fig. 6.1(a)) will use the geometry from Chapter 5 (Gwyther et al., 2014), which assumes hydrostatic equilibrium over the ice shelf, and a 300 m water column thickness along the ice shelf centreline. Bathymetry between the ice shelf centreline and the grounding line is linearly interpolated. The assumption of hydrostatic equilibrium will fail near the grounding line (where ice shelf flexure is affected by the grounding zone) and near grounded rumples and islands (where the ice shelf may be completely resting on land). This geometry is referred to as the 'original geometry'.

The second model geometry (see Fig. 6.1(b)) maintains the same bathymetry for the deep ocean and the continental shelf, but alters the ice shelf geometry. Ice shelf draft is now sourced from ICECAP ice-penetrating radar soundings, while bathymetry is a gravity, magnetic and geologic inversion, based on ICECAP airborne gravity and magnetic measurements (Greenbaum et al., 2015). The bathymetry inversion is derived by first estimating the geologic composition (rock density) of the sea floor which is aided by the measurements of magnetic susceptibility, and then using the gravitational acceleration measurements to determine an estimate

of distance from the gravity meter to the bedrock. This can then be interpolated to produce an 'inversion' field for bathymetry. This bathymetry and ice draft, described in Greenbaum et al. (2015), represents the most accurate understanding for the geometry of the Totten Ice Shelf cavity, with the exception of the missing canal.

The third model geometry (see Fig. 6.1(c)) maintains the same ice shelf geometry as the second model, but with the addition of the ocean-filled canal on the eastern side of the Totten Ice Shelf (Greenbaum et al., 2015). The geometry through the canal is difficult to determine from airborne and satellite geophysics, due to the several kilometre spatial smoothing associated with techniques such as gravity/bathymetry inversions. As a result, an informed guess at the bathymetric depth within the canal must be made. An estimated water column thickness of 175 m below the bottom of the ice draft is used, as it is approximately representative of the gravity-based solution for bathymetry in this region. Care has been taken to ensure the canal is at least two ocean model cells wide in order to remove any possible issues with the numerical solution.

Details of the ocean model are given in Chapter 3 and Chapter 5 (see Gwyther et al., 2015, 2014, respectively), and readers are referred to these chapters or publications for more details. In short, a version of the Regional Ocean Modelling System (ROMS), adapted for sub-ice shelf interaction (Dinniman et al., 2007; Galton-Fenzi et al., 2012), is employed. ROMS is a split-time step, hydrostatic, finite difference model that solves the primitive equations of ocean dynamics on a terrain-following vertical coordinate (Shchepetkin and McWilliams, 2005). Ice shelf–ocean thermodynamics are parameterised with the three-equation formulation of Holland and Jenkins (1999), while vertical mixing is parameterised with the K-Profile Parameterisation of Large et al. (1994).

All models are forced on the surface (with wind stress, heat and salt fluxes) and on the West, North and East lateral boundaries (currents, and heat and salt transport). Surface heat and salt fluxes are taken from satellite observed sea ice formation (SSM/I Tamura et al., 2008), surface winds are from the ERA-interim reanalysis solution (Dee et al., 2011), as well as the lateral boundary heat, salt and momentum transports from NCEP ECCO2 (Menemenlis et al., 2008).

Tides are included as perturbations to the sea surface height at the lateral boundaries, with phases and amplitudes of the 4 largest tidal constituents (M_2, S_2, K_1 and O_1) from the TPXO6.2 Global Inverse Tide Model (Egbert and Erofeeva, 2002). By applying slightly modified constituent periods, the tides were made to be cyclic over 364 days (Pingree and Griffiths, 1981a,b). Hence, the model is configured to run with years of length 364 days and any mention of year length within this chapter should be taken as 364 days.

Forcing is a repeated year of climatological forcing, calculated as the average for the 1992–2012 period. The model is spun up for 30 years, at which point it is in a pseudo steady-state, then run for a further 20 years for analysis.

6.4 Results & discussion

6.4.1 Climatology forcing of original geometry

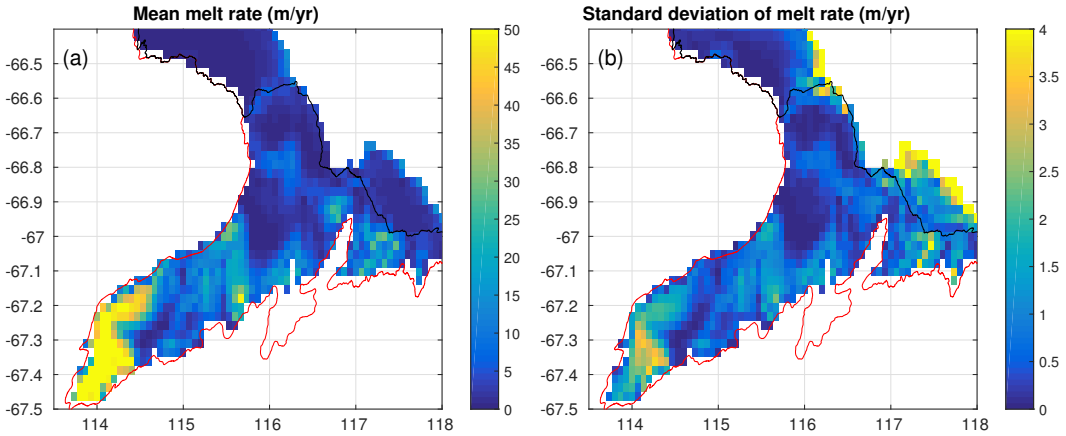

Figure 6.2: The time-averaged (a) melt rate distribution and (b) standard deviation in melt rate for the original geometry. Units for both colour scales are m yr^{-1}. The red and black lines, sourced from the MODIS Mosaic of Antarctica (Scambos et al., 2007), show the grounding line and coastline, respectively.

The spatial distribution and standard deviation of melt rate for the original geometry, averaged over the final 20 years of output, is shown in Fig. 6.2. Melting is strongest ($80 - 100$ m yr^{-1}) at the rear of the cavity, where the depression of the freezing point with pressure increases thermal driving. The standard deviation in melting follows a similar spatial distribution to the melt rate, however, strong variation in weak melting along the ice shelf front is present. This strong variation in weaker melting is due to tidal currents along the ice shelf calving front.

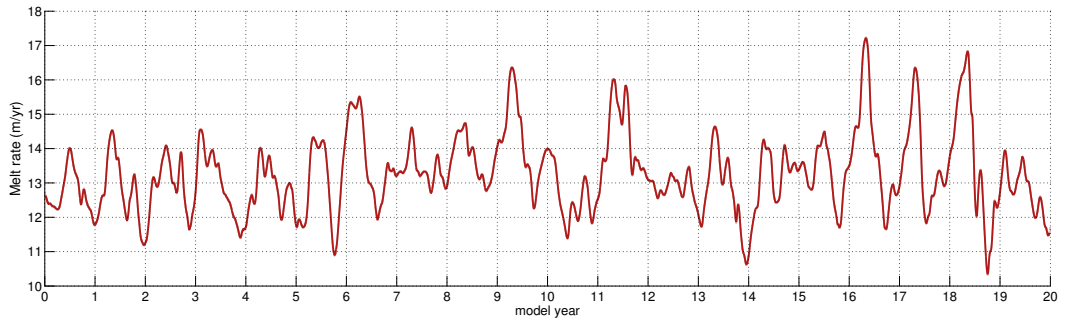

Figure 6.3: The melt rate of the Totten ice shelf, averaged over the entire ice shelf area, and shown for the last 20 years of model output.

The variation in area-average melt rate over the final 20 years of output can be seen

in Fig. 6.3. The Totten ice shelf mean melt rate is approximately 13 m yr^{-1} with a standard deviation of $\sigma = 1.7$ m yr^{-1} over the model run. A strong seasonal cycle is evident for some years (for example, years 16–18), with the remainder of the time series roughly characterised by a peak in melt in the first half of each year and a minimum in melt in the second half of the year (see Section 6.4.3). The variation in melt rate that is not seasonal or tidal can only result from internal variability.

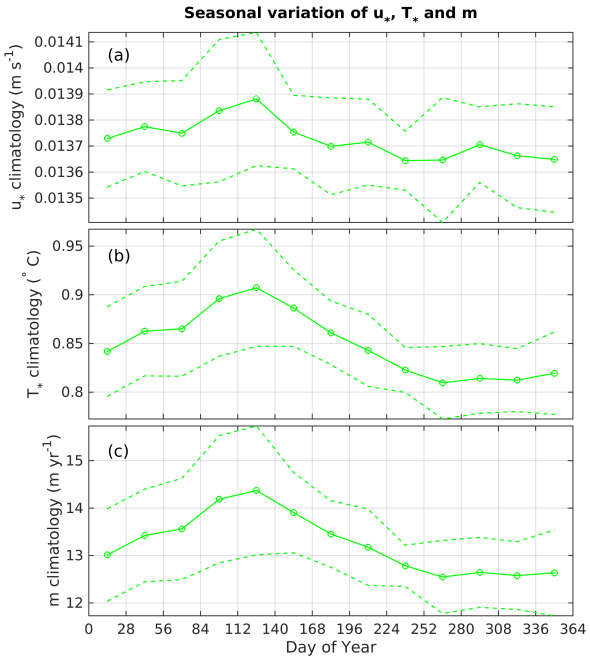

Figure 6.4: The seasonal climatology for (a) u_*(m s^{-1}) (b) T_*(°C), and (c) m(m yr^{-1}) is shown for the original Totten ice shelf geometry. Dashed lines represent ±1 standard deviation.

Climatological averages of the 20 years of high-resolution output into 28-day months, shows the seasonal cycle of area-averaged melting (see Fig. 6.4(c)). Melting displays a seasonal cycle, with a maximum of $\sim$ 14.5 m yr^{-1} in April and a minimum of $\sim$ 12.5 m yr^{-1} from September to December. Friction velocity (Fig. 6.4(a)) and thermal driving (Fig. 6.4(b), and hence melting, display a maximum between day 112 and 140, and a minimum between approximately day 252 and 280. Melt rate displays a stronger connection with T_* than with u_*.

To explore the modes of variability in the melt rate, the power spectral density (power spectrum) for the area-averaged melt rate is calculated (Fig. 6.5). The power spectrum is the distribution of variability in the detrended $m(t)$ as a function of frequency, and is calculated as the real, positive component of the fourier transform of $m(t)$, appropriate scaled by the length of the time series and the sampling frequency (F_s). The power response on a logarithmic scale ($|X(t)|^2/F_s$; Fig. 6.5(a)) shows the trend over the entire frequency range. For variation on a shorter timescale than 1 year, the spectrum is pink; power decreases as frequency increases. Strong

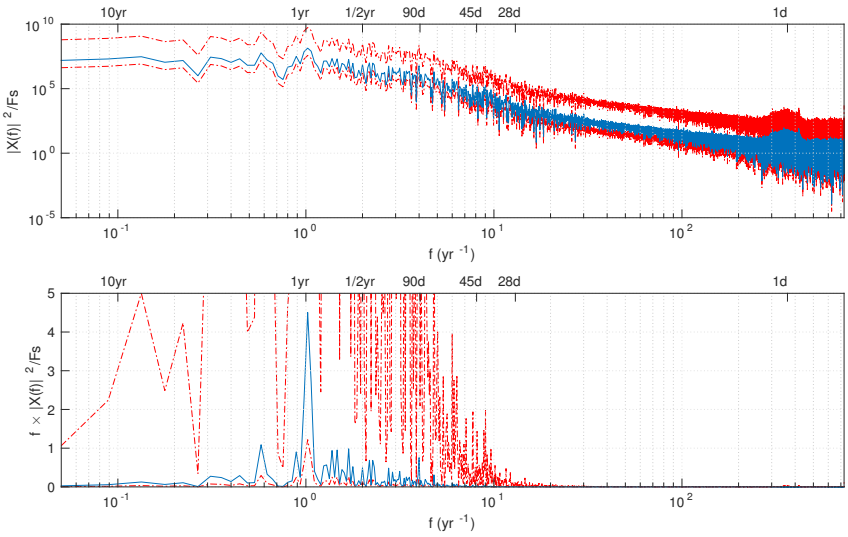

Figure 6.5: The power spectrum of the area-average melt rate time series for the original cavity geometry, $|X(t)|^2/F_s$, shows the decrease in power as the frequency increases. The bottom plot shows $f \times |X(t)|^2/F_s$ and so the area of the peaks represents how much variability they explain. The red dashed lines show the 95% confidence intervals. The axis along the top of each plot shows the time scale.

frequency responses are seen at 21, 24.5 and 29 hours, which result from the tidal forcing frequencies. There are two modes of variability at approximately 40 days and 90 days which register above the noise. Lastly, there is a strong signal at 364 days, which results from the annual cycle of strong melting in winter and weaker melting in summer. The confidence intervals (±95% confidence; red dashed lines) show that variation about 24 hours is not significant compared to the noise. Plotting the power response scaled by the frequency ($f \times |X(t)|^2/F_s$; Fig. 6.5(b)) distributes the variability present at different frequencies evenly. The variability driven by annual forcing is much stronger than any other frequency of variability. The scaling present in this plot also demonstrates that almost all of the total variance occurs through the 1 year peak, with a small amount of variance explained by $\sim 1/2$ year and ~ 2 year variability. It is possible that these $\sim 1/2$ and ~ 2 year modes of variability could explain the variability in surface elevation change that was observed by Paolo et al. (2015) from satellite altimetry.

6.4.2 Sensitivity to ocean forcing

Another important sensitivity is the relationship between melting and oceanic conditions adjacent to the ice front. Any changes to the oceanic forcing, such as warming, may impact the sub-ice shelf conditions and melt rate. Quantifying this transfer relationship is thus important for understanding the response of ice shelf basal melting to ocean forcing changes.

The relationship between melting and thermal driving for the Totten ice shelf, over the T_* range which occurs in the model results, is linear (see Fig. 6.6 with a gradient of 18.7 m yr^{-1}C^{-1} and y-intercept of -2.64 m yr^{-1}. The linear fit suggests that melting increases at a rate of 18.7 m yr^{-1} for every degree of increase in thermal driving. As the thermal driving goes to zero, the melt rate should also decrease to zero. The non-zero y-intercept likely results from fitting to a small range of data (0.81 °C to 0.91 °C), and possibly a non-linearity in melting at lower thermal driving. A non-linear (quadratic) melt–thermal driving relationship has been suggested by others (Holland et al., 2008; Little et al., 2009).

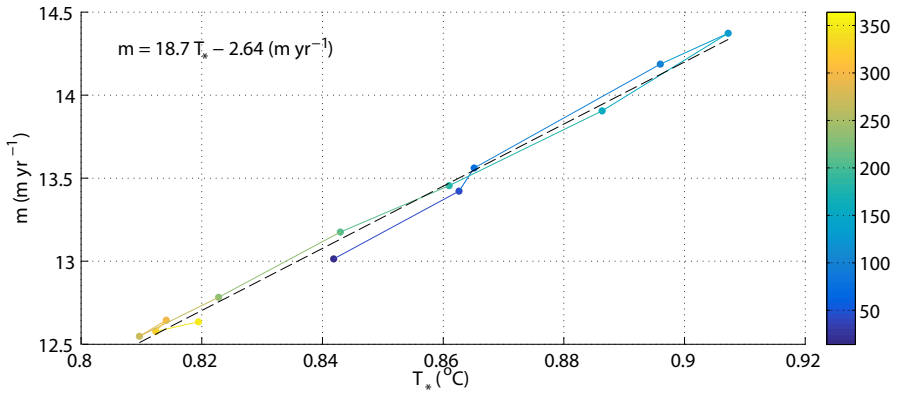

Figure 6.6: The relationship between thermal driving and melting is shown for the melt rate climatology. The data is coloured for the day of the year. The linear fit (black dashed line) is $m = 18.7 \times T_* - 2.64$ m yr^{-1}.

The linear relationship linking heat beneath the ice shelf and melting describes the susceptibility of the ice shelf to heat that has already entered the ice shelf cavity. To determine how melting might react to increased oceanic heat, the relationship between melting and heat outside the cavity must be established. Heat that enters the cavity must come across the continental shelf and is controlled through warm water intrusions from off-shelf and through atmospheric-driven modification. It is expected that processes that modify continental shelf water as it flows across the continental shelf and into the ice shelf cavity, will produce an annual cycle in the temperature that will be similar to that beneath the ice shelf, but with a translation in T-space.

The annual cycle in temperature over a spatially-averaged region on the continental shelf (T_2; 117–119°E, 66–67°S) can be compared to the annual cycle in temperature directly adjacent to the ice shelf base (T_1) and the annual cycle of in situ freezing point (T_f). The variation in the temperature difference between the continental shelf (T_2) and the freezing point beneath the ice shelf (T_f) compared to the melt rate, has a similar slope to the same relationship of water directly beneath the ice shelf ($T_1 - T_f$). As shown in Fig. 6.7, both ΔT–m relationships exhibit similar slopes (melt sensitivity $\Delta m/\Delta T$; units of m yr^{-1} °C^{-1}). The higher variation present in the ΔT–m relationship for the continental shelf should be expected, due to the mixing

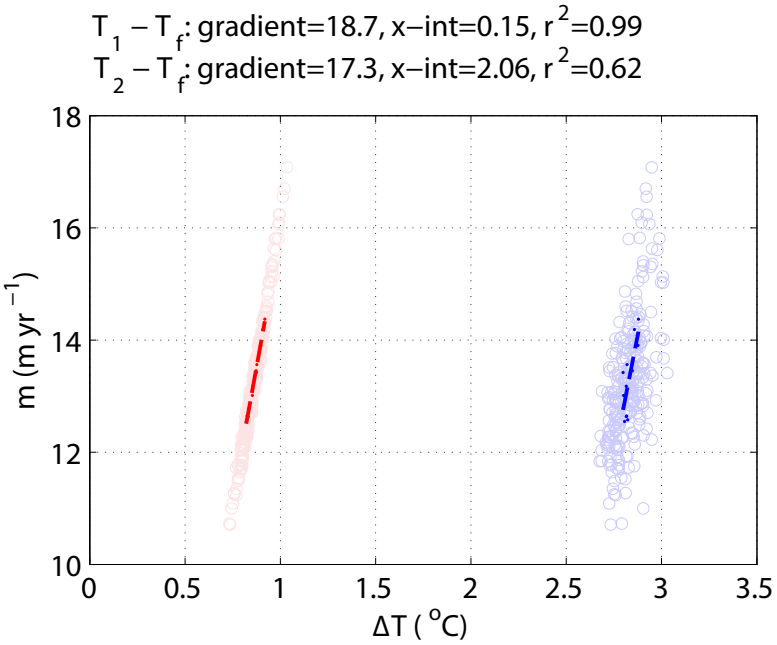

Figure 6.7: The difference between ocean water and the freezing point beneath the ice shelf (ΔT) is plotted against the melt rate. Water beneath the ice shelf (T_1) is shown with 20 years of monthly averages (faint red circles), monthly climatology (red dots) and a linear fit to the monthly climatology (red dashed line). Water on the continental shelf (T_2) is shown with 20 years of monthly averages (faint blue circles), monthly climatology (blue dots), and a linear fit to the monthly climatology (blue dashed line). The gradients of sub-ice shelf water and continental shelf water linear fits are 18.7 m yr^{-1} °C^{-1} (r^2=0.99) and 17.3 m yr^{-1} °C^{-1} (r^2=0.62) respectively.

and modification processes described above. The two relationships can be related by a horizontal translation, calculated as the difference between the x-intercept of each fit, and equal to $\Delta T_{\text{xoffset}} = 1.91°\text{C}$. The relationship linking the approximate melt rate beneath the Totten Glacier and temperature on the continental shelf is

$$\begin{aligned} m &= \frac{\Delta m}{\Delta T}\left(T_{ocean} - T_f - \Delta T_{\text{xoffset}}\right) \\ m &= 18.0\left(T_{ocean} - T_f - 1.91\right) \\ m &= 18.0\left(\Delta T_{cs} - 1.91\right). \end{aligned} \tag{6.1}$$

Here, $\Delta m/\Delta T = 18.0$ m yr^{-1} °C^{-1} is calculated as the mean of the melt sensitivities for both relationships and $\Delta T_{cs} = T_{ocean} - T_f$ is defined as the difference in the continental shelf temperature from the freezing point. Eq. 6.1 allows a temperature on the continental shelf to be converted into an expected melt rate.

The relationship described by Eq. 6.1 allows simple predictions of melt rate using ocean temperature on the continental shelf. This is a similar method to that

suggested by Rignot and Jacobs (2002), who arrive at a melt sensitivity of $\sim$ 10 m yr^{-1} °C^{-1} for a range of Antarctic ice shelves and 15.8 m yr^{-1} °C^{-1} for just the Totten Glacier. The melt sensitivity relationship described in Eq. 6.1 should be more accurate to that of Rignot and Jacobs (2002) as it captures the transfer relationship between shelf water and sub-ice shelf water and uses a numerical model to provide this relationship. Eq. 6.1 can be used to assess the response of melting to a future climate projection scenario. This can be achieved by extrapolating to a perturbation in temperature, $\delta T_{\mathrm{CMIP5}}$, which represents an expected change in ocean temperature. A value for $\delta T_{\mathrm{CMIP5}}$ is sourced from Sallée et al. (2013), which summarises the results from the multiple models that contribute to the Coupled Model Intercomparison Project 5 (CMIP5) experiments. Applying the mean model warming of Circumpolar Deep Water (CDW) under the RCP8.5 scenario at 2100, leads to a $\delta T_{\mathrm{CMIP5}} = 0.412$°C. The mean temperature of the relationship between ΔT and m (blue line; Fig. 6.7) is $\overline{\Delta T_{cs}} \approx 2.8$°C and applying the perturbation of $\delta T_{\mathrm{CMIP5}}$, gives $\Delta T_{cs} = \overline{\Delta T_{cs}} + \delta T_{\mathrm{CMIP5}}$. Substituting ΔT_{cs} into Eq. 6.1, leads to an estimation of melt rate of $m_{\mathrm{CMIP5}} = 23$ m yr^{-1}, which is an increase of 77% above the average melt rate that results from unperturbed continental shelf temperatures (13 m yr^{-1}; Section 6.4.1). Converting the Totten Glacier mean melt rate for the unperturbed continental shelf temperatures into the mean mass loss (over the Totten Glacier ice shelf area; $\sim$ 5700 km^2), gives $\sim$66 Gt yr^{-1}. Assuming that this volume of basal mass loss is fed across the grounding line, and it is then spread over the area of the world's oceans (ETOPO1; Amante and Eakins, 2009), the contribution from the Totten Glacier ice shelf system to global mean sea level would be $\sim$0.20 mm yr^{-1}. The perturbed value of melting (m_{CMIP5} or $\sim$119 Gt yr^{-1}; see above) gives a rough estimate of 2100 conditions, leading to a 80% increase in global mean sea level contribution, equal to 0.36 mm yr^{-1}. This may be a lower bound on sea level contribution due to the marine ice sheet instability.

In Holland et al. (2008), a variety of idealised ice shelf cavity shapes are simulated over a range of thermal driving, to produce a sensitivity relationship between melting and thermal driving. Melting responds to thermal driving following a quadratic relationship; this is attributed to the combined linear increases in thermal driving and sub-ice shelf currents (Holland et al., 2008). Little et al. (2009) suggest that inefficiencies in converting entrained heat into melting increase as temperature is increased. Thus, melting increases with ocean temperature at a less-than-quadratic rate, but is still non-linear. We perform a linear fit for melt sensitivity. Hence, if the true relationship is quadratic, our results represent a lower bound on the increased melt response to ocean warming.

There are several caveats with this simple model. Firstly, the melt rate is filtered via area and temporal averaging; spatial variation in melt rate is not taken into account. Secondly, the function describing the relationship between melt beneath Totten Glacier ice shelf and temperature on the continental shelf is inherently complex and to describe it as linear is probably neglecting several sources of variability. Thirdly, the assumption of a constant temperature offset belies significant uncertainty in the actual future response of the world's oceans (for example, currents may change location and flow strength), and the ability to be accurately predicted by CMIP5

models. It is possible that the Southern Ocean will respond to climate change differently than the model predictions, and it is also possible that CDW will not be the dominant water mass driving melting in the future. Lastly, the perturbed melt rate is achieved assuming a steady-state ice shelf. The basal melt rate will respond to changes in ice draft and hence water column geometry, which will not occur with a constant cavity geometry. Furthermore, a constant cavity geometry does not take into account the response of the ice sheet to increased basal melting, but given that small changes in ice draft did not alter mean melt rates significantly (see Section 6.4.3), this is expected to be a second order effect. Likewise, this analysis is likely to produce similar results with a more accurate cavity geometry (such as the ICECAP geometry with the canal), but is likely to be a second order correction, as the continental shelf bathymetry (and the processes that control heat supply into the cavity) are identical.

However, to the first-order, the m-ΔT relationship will provide representative estimates of changes in melt rate. The estimate of ocean warming is of the same order of magnitude as the projected temperature changes of many other southern ocean water masses (Sallée et al., 2013). As a result, it represents a plausible and probably realistic perturbation to apply. Not taking into account the dynamic response of the ice sheet to changes in basal melting is justified through the magnitude of the change; basal melting does not increase or decrease by orders of magnitude. To do this better requires a coupled ocean–ice sheet model, which are still being developed as of the writing of this thesis. Since the Totten ice shelf is already floating, basal melting does not directly add to sea level. However, without the dynamic response of the ice sheet, the ice shelf is assumed to still be in steady-state, and it is posited that all of that mass loss through basal melting must be replenished as drainage across the grounding line.

Eq. 6.1 should also prove useful for ice sheet modellers; the melt sensitivity relationship presented here will allow melt rate to be estimated, given some ocean temperature on the continental shelf.

6.4.3 Sensitivity to geometry

The area averaged melt rate for each of the three cavity geometries is shown in Fig. 6.8. Interannual melting differs across all three experiments. However, the magnitude of melting is approximately the same across all three cavity geometries with a mean rates of 13.3 m yr^{-1}, 12.8 m yr^{-1} and 13.1 m yr^{-1} for the original geometry, ICECAP geometry without, and with the canal, respectively (one standard deviation of 1.67 m yr^{-1}, 1.43 m yr^{-1}, 1.45 m yr^{-1}, respectively).

The melt rate of the original geometry and the melt rate of the new ICECAP geometry are similar; this is most likely because changes in the depth of the ice draft and bathymetry were not enough to significantly diminish or enhance the thermal driving through altering the pressure freezing point. This suggests that the choice of bathymetry in Gwyther et al. (2014) and Chapter 5 is sound, and the simulated melt rates would be very similar to that with a more realistic ice shelf cavity geometry.

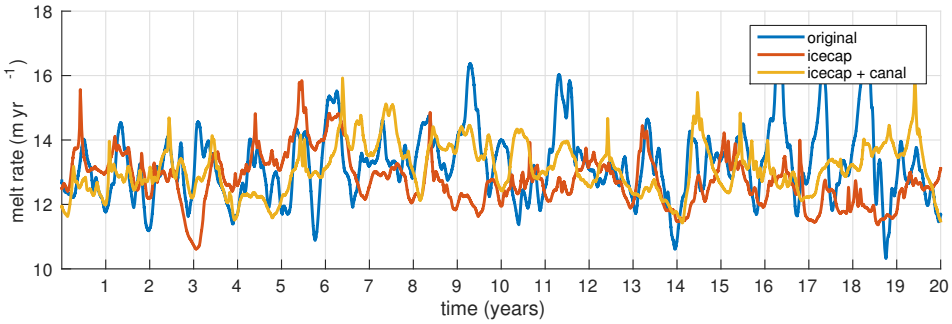

Figure 6.8: Time series of area-average melt rate (m yr^{-1}) for the original geometry, more realistic geometry, and more realistic geometry with canal (marked in the figure legend as original, icecap and icecap + canal, respectively).

Comparing the melt rate of the ICECAP geometry and the ICECAP geometry with the canal, the similarity in the mean melt rate indicates that the canal does not significantly increase heat supply, at least not enough to increase the magnitude of the mean melt rate. The variability present in these melt rate patterns is highly variable, and so must result from internal variability of the ice shelf system. This is further proof that the Totten Glacier ice shelf is a complex system and subject to significant internal variability. Any observations of ice shelf mass balance must be long enough to filter the internal variability, in order to capture the response to external forcing changes, such as climate change. Likewise, observations of the local oceanography must be long enough that they can be placed in the context of external forcing, as opposed to internal variability in basal melting.

The spatial distribution of melting for the ICECAP geometry (Fig. 6.9(a)) and the ICECAP geometry with the canal (Fig. 6.9(b)) show strong melting at the deep grounding line, and for the geometry with the canal, strong melting towards the southern end of the canal. The difference in melt rate between these geometries and the original geometry is compared by the melt rate difference: $m_{\text{sensitivity}} - m_{\text{control}}$. The change in melt between the ICECAP geometry and the original geometry (Fig. 6.9(c) shows reduced melting at the deep grounding line but increased melting across the centre (at $\sim$ 115°E and $\sim$ 116°E). As might be expected, melt rates over most of the ice shelf are similar between the ICECAP geometries with and without the canal. However, the southern end of the canal which connects into the cavity proper displays a strong increase in melting when the canal is hydrologically connected to the open ocean ($\sim$50 m yr^{-1} versus $\sim$25 m yr^{-1}; a 100% increase in the melt rate). These results show that the addition of more realistic ice draft and bathymetry has decreased deep-grounding line melting, but increased melting at mid- and shallow depths; it is possible these positive and negative changes cancel somewhat, leading to similar area-averaged melt rates (see Fig. 6.8).

Comparing the distribution of melt rate demonstrates that while the original geometry predicts representative area-averaged melt rates (see Chapter 5), the addition of realistic bathymetry and ice draft is important for predicting a more representa-

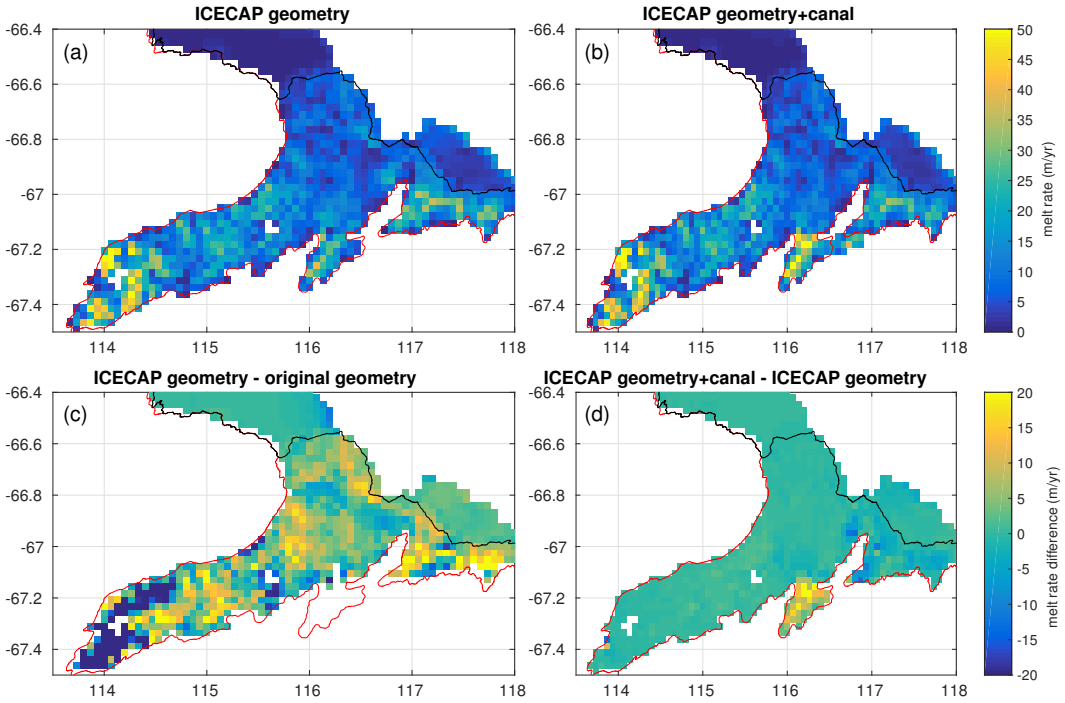

Figure 6.9: (a-b) Temporal average of melt rate (m yr^{-1}) for the (a) ICECAP geometry and (b) the ICECAP geometry with the canal. The melt rate difference (m yr^{-1}) compares (c) the ICECAP geometry against the original geometry (calculated as $m_{\text{ICECAP}} - m_{\text{original}}$) and (d) the ICECAP geometry with canal to that without the canal (calculated as $m_{\text{ICECAP+canal}} - m_{\text{ICECAP}}$). The red and black lines, sourced from the MODIS Mosaic of Antarctica (Scambos et al., 2007), show the grounding line and coastline, respectively.

tive spatial distribution of melting. The increased mass loss at the southern end of the canal is important as it could explain the mass loss observed in this region (e.g. Flament and Rémy, 2012). This may potentially become an important contributor to mass loss if the grounding line in this area retreats further.

The annual variation in melting is investigated with a climatology of the three model runs. Fig. 6.10 shows the climatology, calculated for each model across the last 20 years of the model run. The variation in u_* (shown as the % anomaly from the mean; Fig. 6.10(a)) is generally $\sim 1-2\%$ for all three model runs, while the variation in T_* (Fig. 6.10(b)) is much larger, at $\sim 5-6\%$ over the year. As the variation in melt rate (Fig. 6.10(c)) is similar in magnitude and shape (i.e. timing) to the variation in T_*, the area-averaged melt rate has a stronger correlation with thermal driving than with current speed beneath the ice shelf. This could be expected for the Totten Glacier, as it is subject to relatively warm water intrusions which drive a high thermal difference.

Comparing the different model runs in Fig. 6.10, shows that the seasonal cycle of

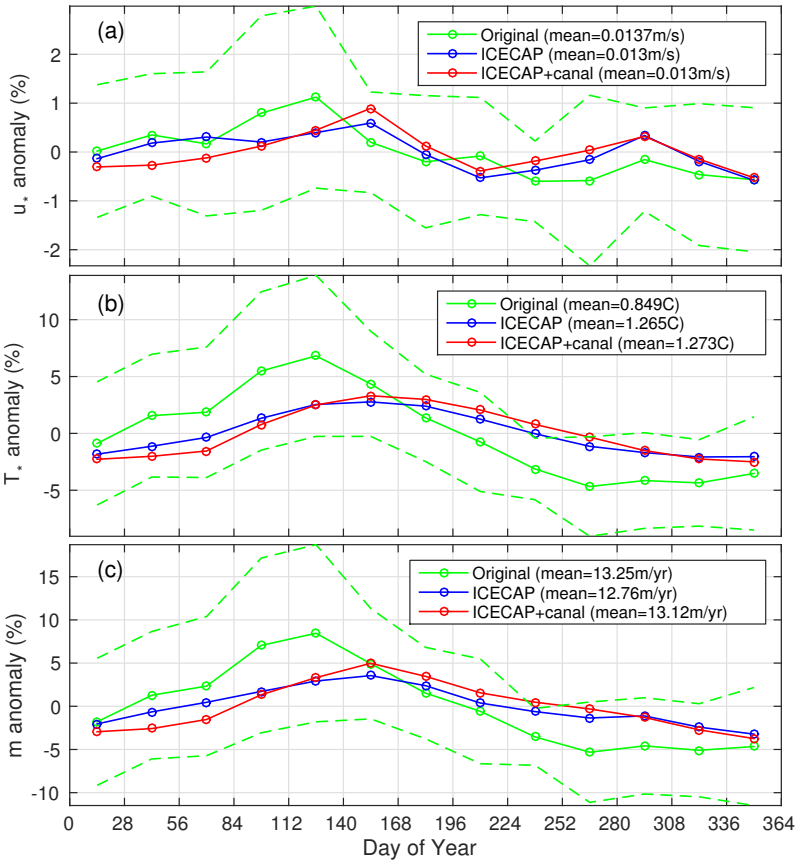

Figure 6.10: The climatology of (a) u_* anomaly, (b) T_* anomaly and (c) m anomaly are shown for the three cavity geometries; original geometry (green), ICECAP without canal (blue), and ICECAP with canal (red). The anomaly is calculated as the difference from the mean over the climatological year normalised by the mean. The mean for each relationship is shown.

melting has a strong peak and lower minimum for the original geometry model (green line), while the ICECAP geometry without canal (blue) and with canal (red) both display similar magnitude and temporal variation in melting. The mean T_* is larger in the two models with ICECAP geometry (mean T_* of approximately $1.27°C^{-1}$) compared to the original geometry (mean T_* of $0.85°C^{-1}$). The larger mean T_* is expected from the ICECAP geometries, as they have a deeper mean ice draft than the original model geometry (see Table 6.1). The in situ freezing point decreases as the mean ice draft increases and as a result, the thermal driving becomes greater.

In Fig. 6.11, the melt rate is plotted against the thermal driving for the original geometry (green circles), the ICECAP geometry without canal (blue circles) and the ICECAP geometry with canal (red circles). The dashed lines show the linear fit to each respective model with the fit parameters shown in Table 6.1. The ICECAP geometry (with or without canal) is less sensitive to thermal driving. There is a

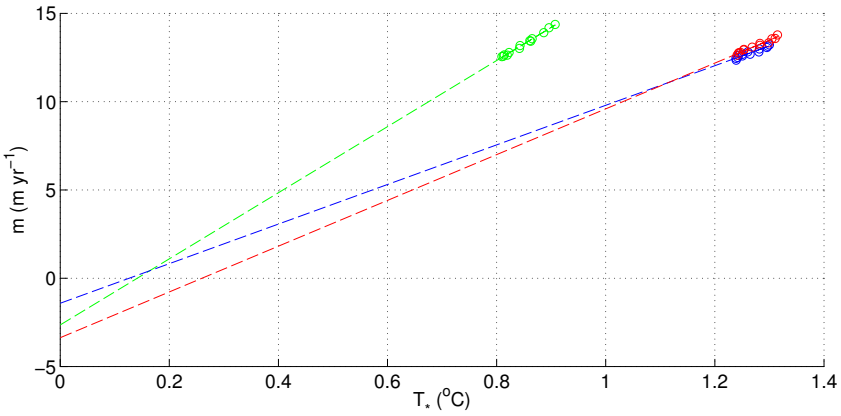

Figure 6.11: The relationship between thermal driving (difference between the top model cell temperature and salinity, and the temperature and salinity at the ice shelf interface) and melt rate is shown for the three model runs. The climatology of original geometry (green circles), ICECAP without canal (blue circles) and ICECAP geometry with canal (red circles) are shown, while the dashed lines show the linear fit for each model.

Run	m-T_* slope (m yr^{-1} °C^{-1})	m-intercept	r^2	Average ice draft (m below MSL)
Original geometry	18.7	-2.64	0.99	641 m
ICECAP	11.2	-1.42	0.92	789 m
ICECAP + canal	13.0	-3.37	0.97	791 m

Table 6.1: Summary of experiments showing the slope of the m-T_* relationship, the intercept with the m axis, the r^2 value for the fit and the average ice draft for each geometry measured in metres below mean sea level (MSL).

50-60% reduction in the slope of the m-T_* fit between the original geometry and the models with ICECAP geometries, despite the ICECAP geometries being subject to thermal driving approximately 1°C higher.

Since processes that control the mixing and modification of heat supply to the base of the ice shelf have the strongest control on melt rates, varying the geometry and in situ freezing point does not have a major effect on the melt rate. That is, the thermal driving across the boundary layer has less effect on the melt rate than the heat that is supplied to the boundary layer. This is a key result - improving understanding of heat supply to the ice shelf is more important than improving the understanding of sub-ice shelf processes.

This result strongly motivates regional modelling studies of ice shelves; the processes that control heat supply across the continental shelf (such as polynya activity or bathymetry) will vary regionally. It also indicates that the melt sensitivity result presented here should not necessarily be applied to different ice shelves which are subject to different continental shelf forcing.

6.5 Conclusion and final remarks

Recent airborne observation campaigns have shown that the Totten Glacier and ice shelf system is susceptible to deep warm water access. However, longer term satellite altimetry analysis shows that the ice shelf experiences significant annual and interannual elevation change.

The sensitivity of basal melting to the ice shelf cavity geometry was modelled. Climatological forcing was applied and the internal variability inherent in the system was investigated.

The area-average melt rate is approximately similar between the geometries tested and the greatest effect of a more realistic cavity geometry is spatial changes in basal melting. The addition of the ocean-access canal to the geometry leads to an increased basal melting on the eastern edge of the cavity, which may explain the observed regional mass loss. The ICECAP cavity geometries are subject to greater thermal driving, but experience the same melt rate as the original geometry; they have a lower melt sensitivity.

A simple linear model relating melt rate and continental shelf temperatures was presented. This relationship can be used to approximate melt rate projections under warming scenarios and will provide ice sheet modellers with a melt rate parameterisation. Using this relationship, the current contribution to global mean sea level from basal mass loss of the Totten Glacier is $\sim$0.20 mm yr^{-1}, which will increase by 80% to 0.36 mm yr^{-1} under the RCP8.5 scenario.

The internal variability of the Totten Glacier ice shelf system was investigated. The temporal evolution of the area-averaged melt rate was not purely annual for any of the cavity geometries that were tested, even with the annual climatology forcing. This suggests that internal variability of the system is significant and important. A power spectral analysis showed power at modes of variability that would be expected, but also variability at sub-year length frequencies. As such, it would seem that the pattern of ice shelf elevation change observed by satellite is likely to include a significant amount of internal variability, and it is only with longer term observations that changes from external forcing will be observed. Likewise, oceanographic observations need to be long enough (e.g. long-term moorings) in order to extend beyond the internal variability in ice shelf melting.

Through this sensitivity study of different ice shelf geometries, important progress in understanding how ice shelves react to external oceanic forcing has been made. Ice shelf melting is relatively insensitive to variations in sub-ice shelf conditions (such as different basal conditions) compared to heat flux into the cavity and oceanographic processes that occur on the continental shelf.

These results shed light on the sensitivity of basal melting to the cavity geometry and strongly motivate long-term monitoring of ice shelf elevation in order to capture the long-term trends in mass balance.

Chapter 7

CONCLUSIONS

7.1 Summary of findings

Ice shelves and the buttressing effect they impose on ice sheet flow is critically important for ice sheet mass balance and sea level rise. One such glacier–ice shelf system which has large sea level rise potential and has been shown by satellite observations to exhibit large changes in surface elevation is the Totten Glacier in East Antarctica. Observations of basal melting, the principle form of ice shelf mass loss, are limited by the difficulty in accessing the ice shelf cavity environment. Numerical simulations present the best method for exploring present and future ice shelf–ocean interaction, but are limited by key uncertainties in numerical models and in ice shelf–ocean interaction as a whole.

A version of ROMS, previously modified to allow thermodynamic interaction between ice and water, was used to explore the ice shelf–ocean interaction in the region of the Totten glacier ice shelf in East Antarctica using a range of configurations. These models were forced on the boundaries with ocean reanalysis products and satellite-derived surface conditions over specified time frames. The resultant melt rate represented the response of the ice shelf to the oceanographic conditions over the same time period.

The same modified ROMS framework was employed in models simulating an idealised geometry ice shelf to investigate the fundamentals and uncertainties of ice-ocean interaction. ROMS was further modified to allow a spatially-varying ice shelf bottom roughness, the effect of which was tested. These results help improve understanding of the key uncertainties in numerical models and how ice shelves interact with the ocean.

The major conclusions of this thesis are summarised below; the chapter which contains each conclusion is noted in parentheses:

1. Melting and freezing increases as the drag at the ice shelf–ocean interface increases; melting increases approximately as the square root of the quadratic drag coefficient. For a hotter ocean cavity environment, a plateauing of melt

may occur at higher drag. And, for a cavity with very high thermal driving, melting may be weaker at higher drag values. (Chapter 3)

2. A spatially-varying hydrodynamic drag coefficient at the ice shelf–ocean, with rougher ice in refreeze zones and smoother ice in melt zones, leads to widespread changes in circulation and hence melting. This indicates the need for spatially-varying drag coefficients and widespread geophysical observations of roughness. (Chapter 3)

3. Melting may be driven by the location of strong flow, as opposed to just the availability of heat. In reality, this may occur in regions of strong tidal currents or rapid flow past bathymetric features. These results strongly emphasise the importance of accounting for the effect of strong flow in the parameterisation of melting (through turbulent exchange rates that vary as a function of velocity); and they inform the planning of field observation that the expected region of high melting may not be located at the deep grounding line. (Chapter 3-4)

4. Idealised modelling suggests that melt distribution is correlated more with either thermal driving or flow velocity, depending on the thermal environment of the ice shelf cavity. For example, in a hot cavity environment, melting is more correlated with thermal driving rather than flow velocity; leading to high melting in the region of strongest thermal driving. Conversely, melting in a cold cavity is more correlated with the strongest flow. Consequently, in changing ocean conditions (e.g. ocean warming), the distribution of melt may shift. (Chapter 4)

5. Modelled basal melt rates beneath the Totten Glacier ice shelf for 1992–2007, show good agreement with glaciological estimates, with an area-averaged melt rate of 9.1 m yr^{-1} (44.5 Gt yr^{-1}), which varies on seasonal timescales (mean range of 3.4 m yr^{-1}) and on a ∼2-3 year interannual timescales (mean range of 5.7 m yr^{-1}). Melt rates are driven by the presence of warmer off-shelf waters, but the interannual variation in melt rate results from the relative cold, dense water production rate of the nearby Dalton ice tongue polynya; a relatively strong polynya year will produce more cold, dense water, which will act to restrict flow of off-shelf waters to the Totten Glacier ice shelf cavity. (Chapter 5)

6. Basal melting beneath the neighbouring ice shelf, the Dalton ice shelf, was shown to be comparable to the Totten Glacier ice shelf over the period 1992–2007 (mean melt of 10.1 m yr^{-1}), with interannual variation driven by inflowing off-shelf water. Interestingly, ice shelf melt water was modelled to flow from the Dalton ice shelf, west and beneath the Totten Glaicer ice shelf, reducing melt rates. (Chapter 5)

7. Area-averaged melt rates beneath the Totten Glacier ice shelf were shown to be relatively insensitive to cavity geometry. A detailed cavity geometry based on airborne observations produced average melt rates of 13.1 m yr^{-1}. The impact of the canal posited by Greenbaum et al. (2015) is greater localised mass loss which may explain satellite observations in the area. (Chapter 6)

8. The climatologically forced model of the Totten Glacier ice shelf, with the original geometry, produced a thermal sensitivity of 18.0 m yr^{-1} $°C^{-1}$. Based on a simple linear relationship between sub-ice shelf cavity water and continental shelf water, and assuming a steady-state ice shelf and a CMIP5 projection of 2100 RCP8.5 CDW temperature anomaly, basal mass loss will increase by 80% from the mean current basal mass loss rate of 66 Gt yr^{-1} to 119 Gt yr^{-1}, with caveats. The difference between this mass loss and that reported in conclusion 4 originates from the different forcing conditions. (Chapter 6)

9. Internal variability of the Totten Glacier ice shelf was shown to be large and hence any observations of ice shelf mass loss will need to occur over a long enough time scale to filter the internal variability. (Chapter 6)

7.2 Future work

The investigations presented in this thesis represent a valuable and unique contribution to understanding ice shelf–ocean interaction. Chapter 3 investigated the effect of basal drag on melting and modelled, and showed the importance of understanding and parameterising spatially-varying basal roughness. In Chapter 4, the difference in melting between a cold and a hot ocean cavity ice shelf was explored; these results have important implications for warming oceans and field observation planning. Simulations of realistic ice shelves were undertaken in Chapter 5 and Chapter 6, producing melt rates (in good agreement with glaciological estimates), mechanisms causing interannual variability, and estimates of sensitivity to changes in ice shelf cavity geometry.

However, there are several pathways to improve upon this research and address questions raised within this thesis. This further work includes:

- Applying a realistic spatially-varying basal roughness to a realistic ice shelf model and determining the effect on melt distribution.
- Testing basal roughness models with different boundary conditions and different cavity geometry.
- Upgrading basal drag parameterisations to use logarithmically varying boundary layer velocity.
- Investigating the effect of subglacial freshwater inflow on ice shelf cavity dynamics and melting.
- Improving the current parameterisations of heat flux through the boundary layer. This is particularly important as model vertical resolution improves and the boundary layer becomes better resolved.
- Run more advanced future climate sensitivity simulations on the Totten Glacier ice shelf model. This will determine the relative impact of changes to oceanographic and atmospheric forcing on melt rate.

- Quantify the impact of Dalton ice shelf meltwater on cooling beneath the Totten Glacier ice shelf.
- Quantify the factors that drive internal variability of melting beneath the Totten Glacier ice shelf.

Appendix A

3-Equation Parameterisation

Thermodynamic interaction at the ice–ocean interface is not directly solved but must be parameterised via equations describing the in situ freezing temperature, and the heat and salt conservation at the interface. The most commonly used formulation for capturing thermodynamic interaction at the ice–ocean interface is the 3-equation parameterisation (Hellmer and Olbers, 1989; Scheduikat and Olbers, 1990; Holland and Jenkins, 1999). This is based on the following three equations,

$$T_B = aS_B + b + cp_B \tag{A.1}$$
$$Q^T_{latent} = Q^T_I - Q^T_M \tag{A.2}$$
$$Q^S_{brine} = Q^S_I - Q^S_M \tag{A.3}$$

Eq. A.1 defines the temperature of seawater film in contact with the base of the ice (T_B) to be at the local freezing point, calculated as a function of the in situ salinity, S_B and the in situ pressure, p_B. The constant coefficients are $a = -5.73 \times 10^{-2}$ °C, $b = 9.39 \times 10^{-2}$ °C and $c = 7.53 \times 10^{-8}$ °C Pa^{-1} (Holland and Jenkins, 1999). In Eq. A.2, the excess/deficit of heat flux at the interface (the heat flux conducted into the ice shelf, Q^T_I, minus the heat flux diffused to the interface from the log layer below, Q^T_M) is balanced by latent heat absorbed/released due to melting/freezing, Q^T_{latent}. By analogy, Eq. A.3 describes the brine flux Q^S_{brine} required to maintain the interface salinity during melting and freezing as the difference between diffusive salt flux in the ice, Q^S_I, and diffusive salt flux to the interface, Q^S_M. Following Holland and Jenkins (1999), diffusion of salt into the ice shelf is considered to be null ($Q^S_I = 0$). A schematic of these properties are shown in Fig. 3.2.

Both the latent heat (Q^T_{latent}) and brine flux (Q^S_{brine}) are a function of a melt/freeze rate, which is defined as a thickness of ice melted (or frozen) per unit time. Likewise, the heat and salt fluxes to the interface (Q^T_M and Q^S_M respectively) vary with the temperature difference and salinity difference across the upper log layer. Furthermore, both heat and salt fluxes in the log layer are functions of the thermal exchange velocities, γ_T and the salinity exchange velocities γ_S, respectively.

Following others (Kader and Yaglom, 1972; McPhee et al., 1987; Holland and Jenkins, 1999), we define these exchange velocities in terms of the friction velocity, u_*,

the turbulent transfer parameter Γ_{turb} and the molecular transfer parameter $\Gamma^{T/S}_{mole}$,

$$\gamma_{T/S} = \frac{u_*}{\Gamma_{turb} + \Gamma^{T/S}_{mole}}, \tag{A.4}$$

where, the contribution from molecular diffusion,

$$\Gamma^{T/S}_{mole} = 12.5(Pr, Sc)^{2/3} - 6, \tag{A.5}$$

is related to the Prandtl number ($Pr = 13.8$; ratio of viscosity to thermal diffusivity) for thermal diffusion (Γ^{T}_{mole}) and the Schmidt number ($Sc = 2432$; ratio of viscosity to saline diffusivity) for saline diffusion (Γ^{S}_{mole}). The turbulent transfer coefficient is given by

$$\Gamma_{turb} = \frac{1}{\kappa} \ln\left(\frac{u_* \xi_N \eta_*^2}{f h_\nu}\right) + \frac{1}{2\xi_N \eta_*} - \frac{1}{\kappa}, \tag{A.6}$$

where h_ν is the viscous sublayer thickness, $\xi_N = 0.052$ is a dimensionless stability constant, η_* is the stability parameter, Von Kármán's constant is $\kappa = 0.40$ and f is the coriolis parameter (See Holland and Jenkins, 1999, for full parameterisation details).

Note that unless otherwise specified, we define the thermal driving (T_*) as the temperature and salinity difference between the temperature in the top layer of the model and the interface temperature. We define the thermal forcing ($T*$) as the temperature difference between the top layer of the model and the interface temperature. This is following Holland and Jenkins (1999), who define the thermal driving as $T_* = T_M - T_B - a(S_M - S_B)$, while defining the thermal forcing as the temperature difference between the interface and top model cell, disregarding the salinity difference ($T_M - T_B$).

Appendix B

Supplementary plots of Totten Ice Shelf model geometry

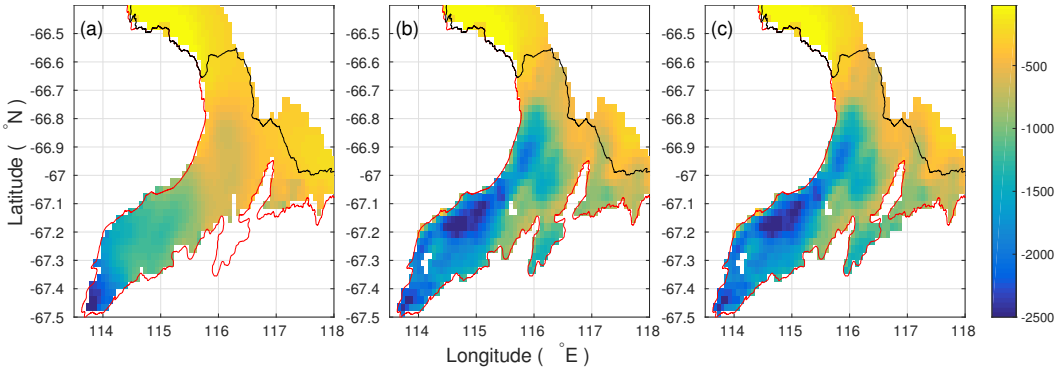

Figure B.1: The bathymetry (height above MSL) for the (a) original bathymetry (see Gwyther et al., 2014), (b) ICECAP bathymetry, and (c) ICECAP bathymetry with entrance canal. The red and black lines, sourced from the MODIS Mosaic of Antarctica (Scambos et al., 2007), show the grounding line and coastline, respectively.

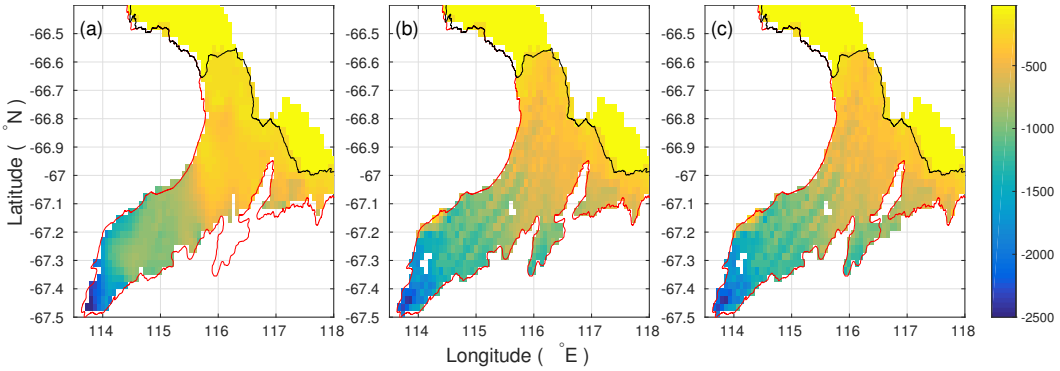

Figure B.2: The ice draft (height above MSL) for the (a) original bathymetry (see Gwyther et al., 2014), (b) ICECAP bathymetry, and (c) ICECAP bathymetry with entrance canal. The red and black lines, sourced from the MODIS Mosaic of Antarctica (Scambos et al., 2007), show the grounding line and coastline, respectively.

Appendix C

Configuration options for Ice shelf–ocean models

	Chapter 3	Chapter 4	Chapter 5	Chapter 6
Model location	Idealised	Idealised	Totten Glacier	Totten Glacier
Horizontal resolution	0.1°	0.1°	1/15°	1/15°
Vertical resolution	24	24	31	31
Baroclinic timestep	300 s	300 s	300 s	300 s
Barotropic timestep	10 s	10 s	10 s	10 s
Horizontal harmonic diffusivity	100 m^2/s	100 m^2/s	0 m^2/s	0 m^2/s
Horizontal viscosity	600 m^2/s	600 m^2/s	800 m^2/s	800 m^2/s
Momentum advection scheme (horz.)	3rd order upstream bias (for 3D momentum) and 2nd order centered (for 2D momentum)			
Momentum advection scheme (vert)	4th order centered (for 3D momentum)			
Tracer scheme (horz.)	4th order centered horizontal tracer advection		3rd order upstream horizontal tracer advection	
Tracer scheme (vert.)	4th order centered vertical tracer advection			
Surface forcing	Hot/cold restoring	Hot/cold restoring	Wind (COREv2; Large and Yeager, 2009), heat/salt fluxes (Tamura et al., 2008)	Wind (ERA-interim; Dee et al., 2011), heat/salt fluxes (Tamura et al., 2008)
Lateral forcing	None	None	ECCO2 (Menemenlis et al., 2008)	ECCO2 (Menemenlis et al., 2008)
Tides	None	Idealised M_2	10-constituents free-surface forcing	4-constituents free-surface forcing
Frazil	None	None	Yes (see Galton-Fenzi et al., 2012)	Yes (see Galton-Fenzi et al., 2012)
Ice–ocean thermodynamics	Velocity-dependent three-equation parameterisation (Holland and Jenkins, 1999)			
Vertical mixing scheme	K-profile parameterisation (Large et al., 1994)			
Slope at ice front	$\sim 1/50$		$\sim 1/20$	

Table C.1: Configuration parameters for models run in each chapter. Horizontal momentum diffusivity for Chapters 5-6 is set to 0 m^2/s, as the 3rd order upstream advection scheme is naturally dissipative (see Dinniman et al., 2003). Surface forcing for Chapters 3-4 is achieved by restoring the surface layer salinity and temperature to constant values.

BIBLIOGRAPHY

Adcroft, A. J., Hill, C. N., and Marshall, J. C. A New Treatment of the Coriolis Terms in C-Grid Models at Both High and Low Resolutions. *Monthly Weather Review*, 127(8): 1928–1936, 1999. doi: 10.1175/1520-0493(1999)127¡1928:ANTOTC¿2.0.CO;2.

Amante, C. and Eakins, B. W. ETOPO1 1 Arc-Minute Global Relief Model: Procedures, Data Sources and Analysis. NOAA Technical Memorandum NESDIS NGDC-24. National Geophysical Data Center, NOAA, 2009.

Arakawa, A. and Lamb, V. R. Computational design of the basic dynamical processes of the UCLA general circulation model. In *Methods in Computational Physics, Volume 17: General Circulation Models of the Atmosphere*, pages 174–267. Academic Press, 1977.

Arzeno, I. B., Beardsley, R. C., Limeburner, R., Owens, B., Padman, L., Springer, S. R., Stewart, C. L., and Williams, M. J. M. Ocean variability contributing to basal melt rate near the ice front of Ross Ice Shelf, Antarctica. *Journal of Geophysical Research: Oceans*, 119(7):4214–4233, 2014. doi: 10.1002/2014JC009792.

Bamber, J. L., Riva, R. E. M., Vermeersen, B. L. a., and LeBrocq, A. M. Reassessment of the potential sea-level rise from a collapse of the West Antarctic Ice Sheet. *Science*, 324 (5929):901–3, 2009. doi: 10.1126/science.1169335.

Bindoff, N. L., Rosenberg, M. A., and Warner, M. J. On the circulation and water masses over the Antarctic continental slope and rise between 80 and 150°E. *Deep-Sea Research Pt. II*, 47(12-13):2299–2326, 2000. doi: 10.1016/S0967-0645(00)00038-2.

Böning, C. W., Dispert, A., Visbeck, M., Rintoul, S. R., and Schwarzkopf, F. U. The response of the Antarctic Circumpolar Current to recent climate change. *Nature Geoscience*, 1(12):864–869, 2008. doi: 10.1038/ngeo362.

British Oceanographic Data Centre. Centenary edition of the gebco digital atlas. [CD-ROM]: Published on behalf of the Intergovernmental Oceanographic Commission and the International Hydrographic Organization, Liverpool, UK., 2003.

Budgell, W. Numerical simulation of ice-ocean variability in the barents sea region. *Ocean Dynamics*, 55(3-4):370–387, 2005. doi: 10.1007/s10236-005-0008-3.

Chelton, D. B., DeSzoeke, R. A., Schlax, M. G., Naggar, K. E., and Siwertz, N. Geographical variability of the first baroclinic Rossby radius of deformation. *Journal of Physical Oceanography*, 28:433–460, 1998.

Chen, J. L., Wilson, C. R., Blankenship, D., and Tapley, B. D. Accelerated Antarctic ice loss from satellite gravity measurements. *Nature Geoscience*, 2(12):859–862, 2009. doi: 10.1038/ngeo694.

Church, J., Gregory, J., Huybrechts, P., Kuhn, M., Lambeck, C., Nhuan, M., Qin, D., and Woodworth, P. Changes in Sea Level. In Houghton, J., Ding, Y., Griggs, D., Noguer, M., der Linden, P. V., Dai, X., Maskell, K., and Johnson, C., editors, *Climate Change 2001: The Scientific Basis: Contribution of Working Group I to the Third Assessment Report of the Intergovernmental Panel on Climate Change*, pages 639–694. Cambridge University Press (Cambridge, New York), 2001.

Church, J. A., White, N. J., Konikow, L. F., Domingues, C. M., Cogley, J. G., Rignot, E., Gregory, J. M., van den Broeke, M. R., Monaghan, A. J., and Velicogna, I. Revisiting the Earth's sea-level and energy budgets from 1961 to 2008. *Geophysical Research Letters*, 38(18):1–8, 2011. doi: 10.1029/2011GL048794.

Church, J. A., Clark, P. U., Cazenave, A., Gregory, J. M., Jevrejeva, S., Levermann, A., Merrifield, M. A., Milne, G. A., Nerem, R. S., Nunn, P. D., Payne, A. J., Pfeffer, W. T., Stammer, D., and Unnikrishnan, A. S. Sea Level Change. In Stocker, T., Qin, D., Plattner, G.-K., Tignor, M., Allen, S., Boschung, J., Nauels, A., Xia, Y., Bex, V., and Midgley, P., editors, *Climate Change 2013: The Physical Science Basis. Contribution of Working Group I to the Fifth Assessment Report of the Intergovernmental Panel on Climate Change*. Cambridge University Press, Cambridge, United Kingdom and New York, NY, USA., 2013.

Cougnon, E. A., Galton-Fenzi, B. K., Meijers, A. J. S., and Legrésy, B. Modelling inter-annual dense shelf water export in the region of the Mertz Glacier Tongue (1992-2007). *Journal of Geophysical Research: Oceans*, 118:5858–5872, 2013. doi: 10.1002/2013JC008790.

Craven, M., Allison, I., Fricker, H. A., and Warner, R. Properties of a marine ice layer under the Amery Ice Shelf, East Antarctica. *Journal of Glaciology*, 55(192):717–728, 2009. doi: 10.3189/002214309789470941.

Cushman-Roisin, B. and Beckers, J.-M. *Introduction to Geophysical Fluid Dynamics*. Academic Press, 2nd edition, 2009. ISBN 9780120887590.

Dansereau, V., Heimbach, P., and Losch, M. Simulation of subice shelf melt rates in a general circulation model: Velocity-dependent transfer and the role of friction. *Journal of Geophysical Research: Oceans*, 119(3):1765–1790, 2014. doi: 10.1002/2013JC008846.

De Angelis, H. and Skvarca, P. Glacier surge after ice shelf collapse. *Science*, 299(5612): 1560–1562, 2003. doi: 10.1126/science.1077987.

De Rydt, J., Holland, P. R., Dutrieux, P., and Jenkins, A. Geometric and oceanographic controls on melting beneath Pine Island Glacier. *Journal of Geophysical Research: Oceans*, 119(4):2420–2438, 2014. doi: 10.1002/2013JC009513.

Dee, D. P., Uppala, S. M., Simmons, a. J., Berrisford, P., Poli, P., Kobayashi, S., Andrae, U., Balmaseda, M. a., Balsamo, G., Bauer, P., Bechtold, P., Beljaars, a. C. M., van de Berg, L., Bidlot, J., Bormann, N., Delsol, C., Dragani, R., Fuentes, M., Geer, a. J., Haimberger, L., Healy, S. B., Hersbach, H., Hólm, E. V., Isaksen, L., Kå llberg, P., Köhler, M., Matricardi, M., McNally, A. P., Monge-Sanz, B. M., Morcrette, J.-J., Park, B.-K., Peubey, C., de Rosnay, P., Tavolato, C., Thépaut, J.-N., and Vitart, F. The ERA-Interim reanalysis: configuration and performance of the data assimilation system. *Quarterly Journal of the Royal Meteorological Society*, 137(656):553–597, 2011. doi: 10.1002/qj.828.

Depoorter, M. A., Bamber, J. L., Griggs, J. A., Lenaerts, J. T. M., Ligtenberg, S. R. M., van den Broeke, M. R., and Moholdt, G. Calving fluxes and basal melt rates of Antarctic ice shelves. *Nature*, 502(7469):89–92, 2013. doi: 10.1038/nature12567.

Dinniman, M. S., Klinck, J. M., and Hofmann, E. E. Sensitivity of Circumpolar Deep Water transport and ice shelf basal melt along the west Antarctic Peninsula to changes in the winds. *Journal of Climate*, 5:4799–4816, 2012.

Dinniman, M. S. and Klinck, J. M. A model study of circulation and cross-shelf exchange on the west Antarctic Peninsula continental shelf. *Deep-Sea Research Pt. II*, 51(17-19): 2003–2022, 2004. doi: 10.1016/j.dsr2.2004.07.030.

Dinniman, M. S., Klinck, J. M., and Smith, W. O. Cross-shelf exchange in a model of the Ross Sea circulation and biogeochemistry. *Deep Sea Research Part II: Topical Studies in Oceanography*, 50(22-26):3103–3120, 2003. doi: 10.1016/j.dsr2.2003.07.011.

Dinniman, M. S., Klinck, J. M., and Smith, W. O. Influence of sea ice cover and icebergs on circulation and water mass formation in a numerical circulation model of the Ross Sea, Antarctica. *Journal of Geophysical Research*, 112(C11):C11013, 2007. doi: 10.1029/2006JC004036.

Dupont, T. K. and Alley, R. B. Assessment of the importance of ice-shelf buttressing to ice-sheet flow. *Geophysical Research Letters*, 32(4):1–4, 2005. doi: 10.1029/2004GL022024.

Dutrieux, P., Vaughan, D. G., Corr, H. F. J., Jenkins, a., Holland, P. R., Joughin, I., and Fleming, A. H. Pine Island glacier ice shelf melt distributed at kilometre scales. *Cryosphere*, 7(5):1543–1555, 2013. doi: 10.5194/tc-7-1543-2013.

Dutrieux, P., Stewart, C., Jenkins, A., Nicholls, K. W., Corr, H. F. J., Rignot, E., and Steffen, K. Basal terraces on melting ice shelves. *Geophysical Research Letters*, 41:5506–5513, 2014. doi: 10.1002/2014GL060618.

Dutton, A. and Lambeck, K. Ice volume and sea level during the last interglacial. *Science*, 6091(337):216–219, 2012. doi: 10.1126/science.1205749.

Egbert, G. D. and Erofeeva, S. Y. Efficient Inverse Modeling of Barotropic Ocean Tides. *Journal of Atmospheric and Oceanic Technology*, 19(2):183–204, 2002. doi: 10.1175/1520-0426(2002)019¡0183:EIMOBO¿2.0.CO;2.

Fernandez-Vasquez, R., Domack, E., Lavoie, C., Gulick, S., Saustrup, S., Frederick, B., Leventer, A., Shevenell, A., and Blankenship, D. D. The geomorphic and sedimentary record of past subglacial water outbursts, Sabrina Coast, East Antarctica. In *AGU Fall Meeting 2014*2, pages PP21A–1313, 2014.

Flament, T. and Rémy, F. Dynamic thinning of Antarctic glaciers from along-track repeat radar altimetry. *Journal of Glaciology*, 58(211):830–840, 2012. doi: 10.3189/2012JoG11J118.

Fraser, A. D., Massom, R. a., Michael, K. J., Galton-Fenzi, B. K., and Lieser, J. L. East Antarctic Landfast Sea Ice Distribution and Variability, 2000-08. *Journal of Climate*, 25 (4):1137–1156, 2012. doi: 10.1175/JCLI-D-10-05032.1.

Fretwell, P., Pritchard, H. D., Vaughan, D. G., Bamber, J. L., Barrand, N. E., Bell, R., Bianchi, C., Bingham, R. G., Blankenship, D. D., Casassa, G., Catania, G., Callens, D.,

Conway, H., Cook, A. J., Corr, H. F. J., Damaske, D., Damm, V., Ferraccioli, F., Forsberg, R., Fujita, S., Gim, Y., Gogineni, P., Griggs, J. A., Hindmarsh, R. C. A., Holmlund, P., Holt, J. W., Jacobel, R. W., Jenkins, A., Jokat, W., Jordan, T., King, E. C., Kohler, J., Krabill, W., Riger-Kusk, M., Langley, K. A., Leitchenkov, G., Leuschen, C., Luyendyk, B. P., Matsuoka, K., Mouginot, J., Nitsche, F. O., Nogi, Y., Nøst, O. A., Popov, S. V., Rignot, E., Rippin, D. M., Rivera, A., Roberts, J., Ross, N., Siegert, M. J., Smith, A. M., Steinhage, D., Studinger, M., Sun, B., Tinto, B. K., Welch, B. C., Wilson, D., Young, D. A., Xiangbin, C., and Zirizzotti, A. Bedmap2: improved ice bed, surface and thickness datasets for Antarctica. *The Cryosphere*, 7(1):375–393, 2013. doi: 10.5194/tc-7-375-2013.

Fricker, H. A., Popov, S., Allison, I., and Young, N. Distribution of marine ice beneath the Amery Ice Shelf. *Geophysical Research Letters*, 28(11):2241, 2001. doi: 10.1029/2000GL012461.

Galton-Fenzi, B. K., Hunter, J. R., Coleman, R., Marsland, S. J., and Warner, R. C. Modeling the basal melting and marine ice accretion of the Amery Ice Shelf. *Journal of Geophysical Research*, 117(C9):C09031, 2012. doi: 10.1029/2012JC008214.

Galton-fenzi, B. K. *Modelling Ice-Shelf/Ocean Interaction*. PhD thesis, University of Tasmania, 2009.

Galton-Fenzi, B., Maraldi, C., Coleman, R., and Hunter, J. The cavity under the Amery Ice Shelf, East Antarctica. *Journal of Glaciology*, 54(188):881–887, 2008. doi: 10.3189/002214308787779898.

Gill, A. E. *Atmosphere-Ocean Dynamics*. Academic Press, 1982. ISBN 978-0-12-283522-3.

Gille, S. T. Decadal-Scale Temperature Trends in the Southern Hemisphere Ocean. *Journal of Climate*, 21(18):4749–4765, 2008. doi: 10.1175/2008JCLI2131.1.

Gladish, C. V., Holland, D. M., Holland, P. R., and Price, S. F. Ice-shelf basal channels in a coupled ice/ocean model. *Journal of Glaciology*, 58(212):1227–1244, 2012. doi: 10.3189/2012JoG12J003.

Goldberg, D. N., Little, C. M., Sergienko, O. V., Gnanadesikan, A., Hallberg, R., and Oppenheimer, M. Investigation of land ice-ocean interaction with a fully coupled ice-ocean model: 2. Sensitivity to external forcings. *Journal of Geophysical Research*, 117 (F2):F02038, 2012. doi: 10.1029/2011JF002247.

Greenbaum, J. S., Blankenship, D. D., Young, D. A., Richter, T. G., Roberts, J. L., Aitken, A. R. A., Legresy, B., Schroeder, D. M., Warner, R. C., van Ommen, T. D., and Siegert, M. J. Ocean access to a cavity beneath Totten Glacier in East Antarctica. *Nature Geoscience*, 8:294–298, 2015. doi: 10.1038/NGEO2388.

Greene, C. A., Bliss, A. K., and Blankenship, D. D. A Bedmap2 Toolbox for Matlab. In *American Geophysical Union Fall Meeting 2013*, pages C51A–0495. American Geophysical Union, 2013.

Gregory, J. M., White, N. J., Church, J. A., Bierkens, M. F. P., Box, J. E., Van den Broeke, M. R., Cogley, J. G., Fettweis, X., Hanna, E., Huybrechts, P., Konikow, L. F., Leclercq, P. W., Marzeion, B., Oerlemans, J., Tamisiea, M. E., Wada, Y., Wake, L. M., and Van de Wal, R. S. W. Twentieth-century global-mean sea-level rise: Is the Whole Greater than the sum of the parts? *Journal of Climate*, 26(13):4476–4499, 2013. doi: 10.1175/JCLI-D-12-00319.1.

Grima, C., Schroeder, D. M., Blankenship, D. D., and Young, D. A. Planetary landing-zone reconnaissance using ice-penetrating radar data: Concept validation in Antarctica. *Planetary and Space Science*, 103:191–204, 2014. doi: 10.1016/j.pss.2014.07.018.

Grosfeld, K., Gerdes, R., and Determann, J. Thermohaline circulation and interaction between ice shelf cavities and the adjacent open ocean. *Journal of Geophysical Research*, 102(C7):15595, 1997. doi: 10.1029/97JC00891.

Gwyther, D. E., Galton-Fenzi, B. K., Hunter, J. R., and Roberts, J. L. Simulated melt rates for the Totten and Dalton ice shelves. *Ocean Science*, 10(3):267–279, 2014. doi: 10.5194/os-10-267-2014.

Gwyther, D. E., Cougnon, E. A., Galton-Fenzi, B. K., Roberts, J. L., Hunter, J. R., and Dinniman, M. S. Modelling ice shelf melting in a changing ocean cavity environment. *Annals of Glaciology*, submitted 2015b.

Gwyther, D. E., Galton-Fenzi, B. K., and Roberts, J. L. Controls of the basal mass balance of floating ice shelves. In *18th Australasian Fluid Mechanics Conference*, pages 1–4, 2012.

Gwyther, D. E., Galton-Fenzi, B. K., Dinniman, M. S., Roberts, J. L., and Hunter, J. R. The effect of basal friction on melting and freezing in ice shelf–ocean models. *Ocean Modelling*, 95:38–52, 2015. doi: 10.1016/j.ocemod.2015.09.004.

Hattermann, T., Smedsrud, L. H., Nøst, O. A., Lilly, J. M., and Galton-Fenzi, B. K. Eddy-resolving simulations of the Fimbul Ice Shelf cavity circulation: Basal melting and exchange with the open ocean. *Ocean Modelling*, 82:28–44, 2014. doi: 10.1016/j.ocemod.2014.07.004.

Hellmer, H. H. Impact of Antarctic ice shelf basal melting on sea ice and deep ocean properties. *Geophysical Research Letters*, 31(10):L10307, 2004. doi: 10.1029/2004GL019506.

Hellmer, H. H. and Olbers, D. J. A two-dimensional model for the thermohaline circulation under an ice shelf. *Antarctic Science*, 1(4):325–336, 1989.

Hellmer, H. H., Kauker, F., Timmermann, R., Determann, J., and Rae, J. Twenty-first-century warming of a large Antarctic ice-shelf cavity by a redirected coastal current. *Nature*, 485(7397):225–228, 2012. doi: 10.1038/nature11064.

Herraiz-Borreguero, L., Allison, I., Craven, M., Nicholls, K. W., and Rosenberg, M. A. Ice shelf/ocean interactions under the Amery Ice Shelf: Seasonal variability and its effect on marine ice formation. *Journal of Geophysical Research: Oceans*, 118:7117–7131, 2013. doi: 10.1002/2013JC009158.

Holland, D. M. and Jenkins, A. Modeling Thermodynamic Ice-Ocean Interactions at the Base of an Ice Shelf. *Journal of Physical Oceanography*, 29(8):1787–1800, 1999. doi: 10.1175/1520-0485(1999)029<1787:MTIOIA>2.0.CO;2.

Holland, D. M. and Jenkins, A. Adaptation of an isopycnic coordinate ocean model for the study of circulation beneath ice shelves. *Monthly Weather Review*, 129(8):1905–1927, 2001. doi: 10.1175/1520-0493(2001)129<1905:AOAICO>2.0.CO;2.

Holland, D. M., Jacobs, S. S., and Jenkins, A. Modelling the ocean circulation beneath the Ross Ice Shelf. *Antarctic Science*, 15(1):13–23, 2003. doi: 10.1017/S0954102003001019.

Holland, P. R. A model of tidally dominated ocean processes near ice shelf grounding lines. *Journal of Geophysical Research: Oceans*, 113(11):1–15, 2008. doi: 10.1029/2007JC004576.

Holland, P. R., Jenkins, A., and Holland, D. M. The Response of Ice Shelf Basal Melting to Variations in Ocean Temperature. *Journal of Climate*, 21(11):2558–2572, 2008. doi: 10.1175/2007JCLI1909.1.

Holland, P. R., Jenkins, A., and Holland, D. M. Ice and ocean processes in the Bellingshausen Sea, Antarctica. *Journal of Geophysical Research*, 115(C5):1–16, 2010. doi: 10.1029/2008JC005219.

Hughes, T. Is the West Antarctic Ice Sheet disintegrating? *Journal of Geophysical Research*, 78(33):7884–7910, November 1973. doi: 10.1029/JC078i033p07884.

Humbert, A. The temperature regime of Fimbulisen, Antarctica. *Annals of Glaciology*, 51 (55):56–64, 2010. doi: 10.3189/172756410791392673.

Hunter, J. R. Specification for Test Models of Ice Shelf Cavities. Technical Report June, Antarctic Climate & Ecosystems Cooperative Research Centre, 2006.

Hunter, J. R. Personal Communication, 2015.

IOC and SCOR and IAPSO. The international thermodynamic equation of seawater – 2010: Calculation and use of thermodynamic properties. In *Intergovernmental Oceanographic Commission, Manuals and Guides No. 56*, page 196. UNESCO (English), 2010.

Jacobs, S. S. On the nature and significance of the Antarctic Slope Front. *Marine Chemistry*, 35(1-4):9–24, 1991. doi: 10.1016/S0304-4203(09)90005-6.

Jacobs, S. S. Bottom water production and its links with the thermohaline circulation. *Antarctic Science*, 16(4):427–437, 2004. doi: 10.1017/S095410200400224X.

Jacobs, S. S., Hellmer, H. H., and Jenkins, A. Antarctic ice sheet melting in the Southeast Pacific. *Geophysical Research Letters*, 23(9):957–960, 1996.

Jacobs, S. S., Jenkins, A., Giulivi, C. F., and Dutrieux, P. Stronger ocean circulation and increased melting under Pine Island Glacier ice shelf. *Nature Geoscience*, 4(8):519–523, 2011. doi: 10.1038/ngeo1188.

Jacobs, S. S., Giulivi, C., Dutrieux, P., Rignot, E., Nitsche, F., and Mouginot, J. Getz Ice Shelf melting response to changes in ocean forcing. *Journal of Geophysical Research: Oceans*, 118(9):4152–4168, 2013. doi: 10.1002/jgrc.20298.

Jamieson, S. S. R., Vieli, A., Livingstone, S. J., Cofaigh, C. Ó., Stokes, C., Hillenbrand, C.-D., and Dowdeswell, J. A. Ice-stream stability on a reverse bed slope. *Nature Geoscience*, 5(11):799–802, 2012. doi: 10.1038/ngeo1600.

Jenkins, A. and Bombosch, A. Modeling the effects of frazil ice crystals on the dynamics and thermodynamics of ice shelf water plumes. *Journal of Geophysical Research*, 100: 6967–6981, 1995.

Jenkins, A. Convection-Driven Melting near the Grounding Lines of Ice Shelves and Tidewater Glaciers. *Journal of Physical Oceanography*, 41(12):2279–2294, 2011. doi: 10.1175/JPO-D-11-03.1.

Jenkins, A., Corr, H. F. J., Nicholls, K. W., Stewart, C. L., and Doake, C. S. Interactions between ice and ocean observed with phase-sensitive radar near an Antarctic ice-shelf grounding line. *Journal of Glaciology*, 52(178):325–346, 2006. doi: 10.3189/172756506781828502.

Jenkins, A., Dutrieux, P., Jacobs, S. S., McPhail, S. D., Perrett, J. R., Webb, A. T., and White, D. Observations beneath Pine Island Glacier in West Antarctica and implications for its retreat. *Nature Geoscience*, 3(7):468–472, 2010. doi: 10.1038/ngeo890.

Joughin, I., Alley, R. B., and Holland, D. M. Ice-sheet response to oceanic forcing. *Science*, 338(6111):1172–1176, 2012. doi: 10.1126/science.1226481.

Joughin, I., Smith, B. E., and Medley, B. Marine ice sheet collapse potentially under way for the Thwaites Glacier Basin, West Antarctica. *Science*, 344(6185):735–8, 2014. doi: 10.1126/science.1249055.

Kader, B. and Yaglom, A. Heat and mass transfer laws for fully turbulent wall flows. *International Journal of Heat and Mass Transfer*, 15(12):2329–2351, 1972. doi: 10.1016/0017-9310(72)90131-7.

Kämpf, J. Cascading-driven upwelling in submarine canyons at high latitudes. *Journal of Geophysical Research*, 110(C2):C02007, 2005. doi: 10.1029/2004JC002554.

Kämpf, J. On the magnitude of upwelling fluxes in shelf-break canyons. *Continental Shelf Research*, 27(17):2211–2223, 2007. doi: 10.1016/j.csr.2007.05.010.

Khazendar, A., Schodlok, M. P., Fenty, I., Ligtenberg, S. R. M., Rignot, E., and van den Broeke, M. R. Observed thinning of Totten Glacier is linked to coastal polynya variability. *Nature communications*, 4:2857, 2013. doi: 10.1038/ncomms3857.

Kimura, S., Nicholls, K., and Venables, E. Estimation of Ice Shelf Melt Rate in the Presence of a Thermohaline Staircase. *Journal of Physical Oceanography*, 45(1):133–148, 2015. doi: 10.1175/JPO-D-14-0106.1.

Kimura, S., Holland, P. R., Jenkins, A., and Piggott, M. The Effect of Meltwater Plumes on the Melting of a Vertical Glacier Face. *Journal of Physical Oceanography*, 44(12): 3099–3117, 2014. doi: 10.1175/JPO-D-13-0219.1.

Klinck, J. M. and Dinniman, M. S. Exchange across the shelf break at high southern latitudes. *Ocean Science*, 6(2):513–524, 2010. doi: 10.5194/os-6-513-2010.

Kusahara, K., Hasumi, H., and Tamura, T. Modeling sea ice production and dense shelf water formation in coastal polynyas around East Antarctica. *Journal of Geophysical Research*, 115(C10):C10006, 2010. doi: 10.1029/2010JC006133.

Large, W. G. and Yeager, S. G. The global climatology of an interannually varying airsea flux data set. *Climate Dynamics*, 33(2-3):341–364, 2009. doi: 10.1007/s00382-008-0441-3.

Large, W. G., McWilliams, J. C., and Doney, S. C. Oceanic vertical mixing: A review and a model with a nonlocal boundary layer parameterization. *Reviews of Geophysics*, 32(4): 363, 1994. doi: 10.1029/94RG01872.

Le Brocq, A. M., Ross, N., Griggs, J. A., Bingham, R. G., Corr, H. F. J., Ferraccioli, F., Jenkins, A., Jordan, T. A., Payne, A. J., Rippin, D. M., and Siegert, M. J. Evidence from ice shelves for channelized meltwater flow beneath the Antarctic Ice Sheet. *Nature Geoscience*, 6(10):1–4, 2013. doi: 10.1038/ngeo1977.

Lemke, P., Ren, J., Alley, R. B., Allison, I., Carrasco, J., Flato, G., Fujii, Y., Kaser, G., Mote, P., Thomas, R. H., and Zhang, T. Observations: Changes in Snow, Ice and Frozen Ground. In Solomon, S., Qin, D., Manning, M., Chen, Z., Marquis, M., Averyt, K. B., Tignor, M., and Miller, H. L., editors, *Climate Change 2007: The Physical Science Basis. Contribution of Working Group I to the Fourth Assessment Report of the Intergovernmental Panel on Climate Change*, chapter 4, pages 337–383. Cambridge University Press (Cambridge, New York), 2007.

Lewis, E. L. and Perkin, R. G. Ice Pumps and Their Rates. *Journal of Geophysical Research*, 91(C10):11756–11762, 1986. doi: 10.1029/JC091iC10p11756.

Little, C. M., Gnanadesikan, A., and Oppenheimer, M. How ice shelf morphology controls basal melting. *Journal of Geophysical Research*, 114:C12007, 2009. doi: 10.1029/2008JC005197.

Liu, H., Jezek, K., Li, B., and Zhao, Z. Radarsat antarctic mapping project digital elevation model version 2. Boulder, Colorado USA: National Snow and Ice Data Center, 2001.

Liu, Y., Moore, J. C., Cheng, X., Gladstone, R. M., Bassis, J. N., Liu, H., Wen, J., and Hui, F. Ocean-driven thinning enhances iceberg calving and retreat of Antarctic ice shelves. *Proceedings of the National Academy of Sciences*, 112(11):3263–3268, 2015. doi: 10.1073/pnas.1415137112.

Losch, M. Modeling ice shelf cavities in a z coordinate ocean general circulation model. *Journal of Geophysical Research: Oceans*, 113(8):C08043, 2008. doi: 10.1029/2007JC004368.

MacAyeal, D. R. Numerical simulations of the Ross Sea tides. *Journal of Geophysical Research*, 89(C1):607, 1984. doi: 10.1029/JC089iC01p00607.

Makinson, K., Schröder, M., and Østerhus, S. Effect of critical latitude and seasonal stratification on tidal current profiles along Ronne Ice Front, Antarctica. *Journal of Geophysical Research*, 111(C3):C03022, 2006. doi: 10.1029/2005JC003062.

Makinson, K., Holland, P. R., Jenkins, A., Nicholls, K. W., and Holland, D. M. Influence of tides on melting and freezing beneath Filchner-Ronne Ice Shelf, Antarctica. *Geophysical Research Letters*, 38(6):L06601, 2011. doi: 10.1029/2010GL046462.

Marks, K. M. and Smith, W. H. F. An Evaluation of Publicly Available Global Bathymetry Grids. *Marine Geophysical Research*, 27(1):19–34, 2006. doi: 10.1007/s11001-005-2095-4.

Martinson, D. G. and McKee, D. C. Transport of warm Upper Circumpolar Deep Water onto the western Antarctic Peninsula continental shelf. *Ocean Science*, 8(4):433–442, 2012. doi: 10.5194/os-8-433-2012.

Massom, R. A., Harris, P. T., Michael, K. J., and Potter, M. J. The distribution and formative processes of latent-heat polynyas in East Antarctica. *Annals of Glaciology*, 27: 420–426, 1998.

Massom, R. A., Hill, K. L., Lytle, V. I., Worby, A. P., Paget, M. J., and Allison, I. Effects of regional fast-ice and iceberg distributions on the behaviour of the Mertz Glacier polynya, East Antarctica. *Annals of Glaciology*, 33(1):391–398, 2001.

Mathiot, P., Goosse, H., Fichefet, T., Barnier, B., and Gallée, H. Modelling the seasonal variability of the Antarctic Slope Current. *Ocean Science*, 7(4):455–470, 2011. doi: 10.5194/os-7-455-2011.

McDougall, T. J., Barker, P. M., Feistel, R., and Galton-Fenzi, B. K. Melting of Ice and Sea Ice into Seawater and Frazil Ice Formation. *Journal of Physical Oceanography*, 44(7): 1751–1775, 2014. doi: 10.1175/JPO-D-13-0253.1.

McPhee, M. Turbulent heat flux in the upper ocean under sea ice. *Journal of Geophysical Research*, 97:5365–5379, 1992.

McPhee, M. G. An analytic similarity theory for the planetary boundary layer stabilized by surface buoyancy. *Boundary-Layer Meteorology*, 21(3):325–339, 1981. doi: 10.1007/BF00119277.

McPhee, M. G. On the Turbulent Mixing Length in the Oceanic Boundary Layer. *Journal of Physical Oceanography*, 24(9):2014–2031, 1994. doi: 10.1175/1520-0485(1994)024¡2014:OTTMLI¿2.0.CO;2.

McPhee, M. G., Maykut, G. A., and Morison, J. H. Dynamics and thermodynamics of the ice/upper ocean system in the marginal ice zone of the Greenland Sea. *Journal of Geophysical Research*, 92:7017–7031, 1987. doi: 10.1029/JC092iC07p07017.

Meier, M. F., Dyurgerov, M. B., Rick, U. K., O'neel, S., Pfeffer, W. T., Anderson, R. S., Anderson, S. P., and Glazovsky, A. F. Glaciers dominate eustatic sea-level rise in the 21st century. *Science*, 317(5841):1064–7, 2007. doi: 10.1126/science.1143906.

Meijers, a. J. S., Shuckburgh, E., Bruneau, N., Sallee, J.-B., Bracegirdle, T. J., and Wang, Z. Representation of the Antarctic Circumpolar Current in the CMIP5 climate models and future changes under warming scenarios. *Journal of Geophysical Research*, 117(C12): C12008, 2012. doi: 10.1029/2012JC008412.

Menemenlis, D., Campin, J.-m., Heimbach, P., Hill, C., Lee, T., Nguyen, A., Schodlok, M., and Zhang, H. ECCO2: High Resolution Global Ocean and Sea Ice Data Synthesis. *Mercator Ocean Quarterly Newsletter*, 31(October):13–21, 2008.

Mercer, J. H. West Antarctic ice sheet and CO2 greenhouse effect: a threat of disaster. *Nature*, 271(5643):321–325, 1978. doi: 10.1038/271321a0.

Millgate, T., Holland, P. R., Jenkins, A., and Johnson, H. L. The effect of basal channels on oceanic ice-shelf melting. *Journal of Geophysical Research: Oceans*, 118:6951–6964, 2013. doi: 10.1002/2013JC009402.

Moffat, C., Owens, B., and Beardsley, R. C. On the characteristics of Circumpolar Deep Water intrusions to the west Antarctic Peninsula Continental Shelf. *Journal of Geophysical Research*, 114(C5):C05017, 2009. doi: 10.1029/2008JC004955.

Moholdt, G., Padman, L., and Fricker, H. A. Basal mass budget of Ross and Filchner-Ronne ice shelves, Antarctica, derived from Lagrangian analysis of ICESat altimetry. *Journal of Geophysical Research: Earth Surface*, 119(11):2361–2380, 2014. doi: 10.1002/2014JF003171.

Motyka, R. J., Dryer, W. P., Amundson, J., Truffer, M., and Fahnestock, M. Rapid submarine melting driven by subglacial discharge, LeConte Glacier, Alaska. *Geophysical Research Letters*, 40(19):5153–5158, 2013. doi: 10.1002/grl.51011.

Mueller, R. D., Padman, L., Dinniman, M. S., Erofeeva, S. Y., Fricker, H. a., and King, M. a. Impact of tide-topography interactions on basal melting of Larsen C Ice Shelf, Antarctica. *Journal of Geophysical Research*, 117(C5):1–20, 2012. doi: 10.1029/2011JC007263.

Munk, W. Twentieth century sea level: An enigma. *Proceedings of the National Academy of Science, USA*, 99:6550–6555, 2002.

NEEM community members. Eemian interglacial reconstructed from a greenland folded ice core. *Nature*, 7433(493):489–494, 2013. doi: 10.1038/nature11789.

Nikurashin, M. and Ferrari, R. Radiation and Dissipation of Internal Waves Generated by Geostrophic Motions Impinging on Small-Scale Topography: Application to the Southern Ocean. *Journal of Physical Oceanography*, 40(9):2025–2042, 2010. doi: 10.1175/2010JPO4315.1.

Orsi, A. H., Whitworth III, T., and Nowlin Jr, W. D. On the meridional extent and fronts of the Antarctic Circumpolar Current. *Deep-Sea Research Pt. I*, 42(5):641–673, 1995.

Padman, L., Costa, D. P., Dinniman, M. S., Fricker, H. a., Goebel, M. E., Huckstadt, L. a., Humbert, A., Joughin, I., Lenaerts, J. T. M., Ligtenberg, S. R. M., Scambos, T., and van den Broeke, M. R. Oceanic controls on the mass balance of Wilkins Ice Shelf, Antarctica. *Journal of Geophysical Research*, 117(C1):C01010, 2012. doi: 10.1029/2011JC007301.

Paolo, F. S., Fricker, H. A., and Padman, L. Volume loss from Antarctic ice shelves is accelerating. *Science*, 348(6232):327–331, 2015. doi: 10.1126/science.aaa0940.

Paterson, W. S. B. *The Physics of Glaciers*. Butterworth-Heinemann, 3rd edition, 2002.

Paulson, C. A. The Mathematical Representation of Wind Speed and Temperature Profiles in the Unstable Atmospheric Surface Layer. *Journal of Applied Meteorology*, 9(6):857–861, 1970. doi: "10.1175/1520-0450(1970)009¡0857:TMROWS¿2.0.CO;2".

Pedlosky, J. *Geophysical Fluid Dynamics*. Springer New York, 2nd edition, 1982. doi: 10.1007/978-1-4612-4650-3.

Pingree, R. D. and Griffiths, D. K. S2 tidal simulations on the northwest European shelf. *Journal of the Marine Biological Association of the United Kingdom*, 61:609–616, 1981a. doi: 10.1017/S0025315400048074. URL `http://dx.doi.org/10.1017/S0025315400048074`.

Pingree, R. D. and Griffiths, D. K. The N2 tide and semidiurnal amphidromes around the British Isles. *Journal of the Marine Biological Association of the United Kingdom*, 61: 617–625, 1981b. doi: 10.1017/S0025315400048086.

Pritchard, H. D., Ligtenberg, S. R. M., Fricker, H. A., Vaughan, D. G., van den Broeke, M. R., and Padman, L. Antarctic ice-sheet loss driven by basal melting of ice shelves. *Nature*, 484(7395):502–505, 2012. doi: 10.1038/nature10968.

Pritchard, H. D., Arthern, R. J., Vaughan, D. G., and Edwards, L. A. Extensive dynamic thinning on the margins of the Greenland and Antarctic ice sheets. *Nature*, 461(7266): 971–975, 2009. doi: 10.1038/nature08471.

Reddy, T. E., Holland, D. M., and Arrigo, K. R. Ross ice shelf cavity circulation, residence time, and melting: Results from a model of oceanic chlorofluorocarbons. *Continental Shelf Research*, 30(7):733–742, 2010. doi: 10.1016/j.csr.2010.01.007.

Rignot, E., Jacobs, S., Mouginot, J., and Scheuchl, B. Ice Shelf Melting Around Antarctica. *Science*, 341(6143):266–270, 2013. doi: 10.1126/science.1235798.

Rignot, E., Mouginot, J., Morlighem, M., Seroussi, H., and Scheuchl, B. Widespread, rapid grounding line retreat of Pine Island, Thwaites, Smith, and Kohler glaciers, West Antarctica, from 1992 to 2011. *Geophysical Research Letters*, 41(10):3502–3509, 2014. doi: 10.1002/2014GL060140.

Rignot, E. J. Fast Recession of a West Antarctic Glacier. *Science*, 281(5376), 1998.

Rignot, E. Changes in ice dynamics and mass balance of the Antarctic ice sheet. *Philosophical Transactions of the Royal Society A*, 364(1844):1637–1655, 2006. doi: 10.1098/rsta.2006.1793.

Rignot, E. J. Mass balance of East Antarctic glaciers and ice shelves from satellite data. *Annals of Glaciology*, 34(1):217–227, 2002. doi: 10.3189/172756402781817419.

Rignot, E. J. and Jacobs, S. S. Rapid bottom melting widespread near Antarctic Ice Sheet grounding lines. *Science*, 296(5575):2020–2023, 2002. doi: 10.1126/science.1070942.

Rignot, E. J., Bamber, J. L., van den Broeke, M. R., Davis, C., Li, Y., van de Berg, W. J., and van Meijgaard, E. Recent Antarctic ice mass loss from radar interferometry and regional climate modelling. *Nature Geoscience*, 1(2):106–110, 2008. doi: 10.1038/ngeo102.

Rignot, E. J., Mouginot, J., and Scheuchl, B. Antarctic grounding line mapping from differential satellite radar interferometry. *Geophysical Research Letters*, 38(10):1–6, 2011. doi: 10.1029/2011GL047109.

Rintoul, S. R., Hughes, C. W., and Olbers, D. Chapter 4.6 the antarctic circumpolar current system. In Gerold Siedler, J. C. and Gould, J., editors, *Ocean Circulation and Climate Observing and Modelling the Global Ocean*, volume 77 of *International Geophysics*, pages 271–302. Academic Press, 2001. doi: 10.1016/S0074-6142(01)80124-8.

Roberts, J. L., Warner, R. C., Young, D., Wright, A., van Ommen, T. D., Blankenship, D. D., Siegert, M., Young, N. W., Tabacco, I. E., Forieri, A., Passerini, A., Zirizzotti, A., and Frezzotti, M. Refined broad-scale sub-glacial morphology of Aurora Subglacial Basin, East Antarctica derived by an ice-dynamics-based interpolation scheme. *The Cryosphere*, 5(3):551–560, 2011. doi: 10.5194/tc-5-551-2011.

Robertson, R. Tidally induced increases in melting of Amundsen Sea ice shelves. *Journal of Geophysical Research: Oceans*, 118(6):3138–3145, 2013. doi: 10.1002/jgrc.20236.

Robinson, N. J., Williams, M. J. M., Barrett, P. J., and Pyne, A. R. Observations of flow and ice-ocean interaction beneath the McMurdo Ice Shelf, Antarctica. *Journal of Geophysical Research: Oceans*, 115:C03025, 2010. doi: 10.1029/2008JC005255.

Sallée, J. B., Shuckburgh, E., Bruneau, N., Meijers, a. J. S., Bracegirdle, T. J., and Wang, Z. Assessment of Southern Ocean mixed-layer depths in CMIP5 models: Historical bias and forcing response. *Journal of Geophysical Research: Oceans*, 118(4):1845–1862, 2013. doi: 10.1002/jgrc.20157.

Scambos, T. A., Bohlander, J. A., Shuman, C. A., and Skvarca, P. Glacier acceleration and thinning after ice shelf collapse in the Larsen B embayment, Antarctica. *Geophysical Research Letters*, 31(18):L18402, 2004. doi: 10.1029/2004GL020670.

Scambos, T. A., Haran, T. M., Fahnestock, M. A., Painter, T. H., and Bohlander, J. MODIS-based Mosaic of Antarctica (MOA) data sets: Continent-wide surface morphology and snow grain size. *Remote Sensing of Environment*, 111(2):242–257, 2007. doi: 10.1016/j.rse.2006.12.020.

Scheduikat, M. and Olbers, D. A one-dimensional mixed layer model beneath the Ross Ice Shelf with tidally induced vertical mixing. *Antarctic Science*, 2(1):29–42, 1990. doi: 10.1017/S0954102090000049.

Schoof, C. Ice sheet grounding line dynamics: Steady states, stability, and hysteresis. *Journal of Geophysical Research*, 112(F3):F03S28, jul 2007. doi: 10.1029/2006JF000664.

Shchepetkin, A. F. A method for computing horizontal pressure-gradient force in an oceanic model with a nonaligned vertical coordinate. *Journal of Geophysical Research*, 108(C3): 1–34, 2003. doi: 10.1029/2001JC001047.

Shchepetkin, A. F. and McWilliams, J. C. The regional oceanic modeling system (ROMS): a split-explicit, free-surface, topography-following-coordinate oceanic model. *Ocean Modelling*, 9(4):347–404, 2005. doi: 10.1016/j.ocemod.2004.08.002.

Shchepetkin, A. F. and McWilliams, J. C. Correction and commentary for Ocean forecasting in terrain-following coordinates: Formulation and skill assessment of the regional ocean modeling system by Haidvogel et al., J. Comp. Phys. 227, pp. 35953624. *Journal of Computational Physics*, 228(24):8985–9000, 2009a. doi: 10.1016/j.jcp.2009.09.002.

Shchepetkin, A. F. and McWilliams, J. C. Computational Kernel Algorithms for Fine-Scale, Multiprocess, Longtime Oceanic Simulations. In Temam, R. M. and Tribbia, J. J., editors, *Handbook of Numerical Analysis*, volume XIV, pages 121–183. North-Holland, 2009b. doi: 10.1016/S1570-8659(08)01202-0.

Shepherd, A. and Wingham, E. J., D.and Rignot. Warm ocean is eroding West Antarctic Ice Sheet. *Geophysical Research Letters*, 31(23):4–7, 2004.

Shepherd, A., Ivins, E. R., A, G., Barletta, V. R., Bentley, M. J., Bettadpur, S., Briggs, K. H., Bromwich, D. H., Forsberg, R., Galin, N., Horwath, M., Jacobs, S. S., Joughin, I., King, M. a., Lenaerts, J. T. M., Li, J., Ligtenberg, S. R. M., Luckman, A., Luthcke, S. B., McMillan, M., Meister, R., Milne, G., Mouginot, J., Muir, A., Nicolas, J. P., Paden, J., Payne, A. J., Pritchard, H., Rignot, E., Rott, H., Sørensen, L. S., Scambos, T. A., Scheuchl, B., Schrama, E. J. O., Smith, B., Sundal, A. V., van Angelen, J. H., van de Berg, W. J., van den Broeke, M. R., Vaughan, D. G., Velicogna, I., Wahr, J., Whitehouse, P. L., Wingham, D. J., Yi, D., Young, D., and Zwally, H. J. A reconciled estimate of ice-sheet mass balance. *Science*, 338(6111):1183–9, 2012. doi: 10.1126/science.1228102.

Smith, B. E., Fricker, H. A., Joughin, I. R., and Tulaczyk, S. An inventory of active subglacial lakes in Antarctica detected by ICESat (2003-2008). *Journal of Glaciology*, 55 (192):573–595, 2009. doi: 10.3189/002214309789470879.

Smith, W. and Sandwell, D. Global sea floor topography from satellite altimetry and ship depth soundings. *Science*, 2:209–215, 1997.

Soulsby, R. L. THE BOTTOM BOUNDARY LAYER OF SHELF SEAS. In Johns, B., editor, *Physical Oceanography of Coastal and Shelf Seas*, pages 189–266. Elsevier Science Publishers B.V., Amsterdam, 1983.

St-Laurent, P., Klinck, J. M., and Dinniman, M. S. On the Role of Coastal Troughs in the Circulation of Warm Circumpolar Deep Water on Antarctic Shelves. *Journal of Physical Oceanography*, 43(1):51–64, 2013. doi: 10.1175/JPO-D-11-0237.1.

Stanton, T. P., Shaw, W. J., Truffer, M., Corr, H. F. J., Peters, L. E., Riverman, K. L., Bindschadler, R., Holland, D. M., and Anandakrishnan, S. Channelized ice melting in the ocean boundary layer beneath Pine Island Glacier, Antarctica. *Science*, 341(6151): 1236–9, 2013. doi: 10.1126/science.1239373.

Steele, M., Mellor, G. L., and McPhee, M. G. Role of the Molecular Sublayer in the Melting or Freezing of Sea Ice. *Journal of Physical Oceanography*, 19:139–147, 1989. doi: 10.1175/1520-0485(1989)019¡0139:ROTMSI¿2.0.CO;2.

Steig, E. J., Ding, Q., Battisti, D., and Jenkins, A. Tropical forcing of Circumpolar Deep Water Inflow and outlet glacier thinning in the Amundsen Sea Embayment,West Antarctica. *Annals of Glaciology*, 53(60):19–28, 2012.

Stevens, C., McPhee, M., Forrest, A., Leonard, G., Stanton, T., and Haskell, T. The Influence of an Antarctic Glacier Tongue on Near-field Ocean Circulation and Mixing. *Journal of Geophysical Research: Oceans*, 119:2344–2362, 2014. doi: 10.1002/2013JC009070.

Tamura, T., Ohshima, K. I., and Nihashi, S. Mapping of sea ice production for Antarctic coastal polynyas. *Geophysical Research Letters*, 35(7):L07606, 2008. doi: 10.1029/2007GL032903.

Thoma, M., Jenkins, A., Holland, D., and Jacobs, S. Modelling Circumpolar Deep Water intrusions on the Amundsen Sea continental shelf, Antarctica. *Geophysical Research Letters*, 35(18):L18602, 2008. doi: 10.1029/2008GL034939.

Thomas, R. H. and Bentley, C. R. A model for Holocene retreat of the West Antarctic Ice Sheet. *Quaternary Research*, 10(2):150–170, 1978. doi: 10.1016/0033-5894(78)90098-4.

Timmermann, R. Simulations of ice-ocean dynamics in the Weddell Sea 1. Model configuration and validation. *Journal of Geophysical Research*, 107(C3):1–11, 2002. doi: 10.1029/2000JC000741.

Timmermann, R., Le Brocq, A., Deen, T., Domack, E., Dutrieux, P., Galton-Fenzi, B., Hellmer, H., Humbert, A., Jansen, D., Jenkins, A., Lambrecht, A., Makinson, K., Niederjasper, F., Nitsche, F., Nøst, O. a., Smedsrud, L. H., and Smith, W. H. F. A consistent data set of Antarctic ice sheet topography, cavity geometry, and global bathymetry. *Earth System Science Data*, 2(2):261–273, 2010. doi: 10.5194/essd-2-261-2010.

Treverrow, A., Warner, R., and Budd, W. Meteoric and marine ice crystal orientation fabrics from the Amery Ice Shelf, East Antarctica. *Journal of Glaciology*, 56(199):877–890, 2010.

Vaughan, D. G., Comiso, J. C., Allison, I., Carrasco, J., Kaser, G., Kwok, R., Mote, P., Murray, T., Paul, F., Rem, J., Rignot, E. J., Solomina, O., Steffen, K., and Zhang, T. Observations: cryosphere. In Stocker, T., Qin, D., Plattner, G.-K., Tignor, M., Allen, S., Boschung, J., Nauels, A., Xia, Y., Bex, V., and Midgley, P. M., editors, *Climate Change 2013: The Physical Science Basis. Contribution of Working Group I to the Fifth Assessment Report of the Intergovernmental Panel on Climate Change*. Cambridge University Press, Cambridge, United Kingdom and New York, NY, USA, 2013.

Vaughan, D. G., Corr, H. F. J., Bindschadler, R. a., Dutrieux, P., Gudmundsson, G. H., Jenkins, A., Newman, T., Vornberger, P., and Wingham, D. J. Subglacial melt channels and fracture in the floating part of Pine Island Glacier, Antarctica. *Journal of Geophysical Research*, 117(F3):F03012, 2012. doi: 10.1029/2012JF002360.

Warner, R. C. and Roberts, J. L. Pine Island Glacier (Antarctica) velocities from Landsat7 images between 2001 and 2011: FFT-based image correlation for images with data gaps. *Journal of Glaciology*, 59(215):571–582, 2013. doi: 10.3189/2013JoG12J113.

Watson, C. S., White, N. J., Church, J. A., King, M. A., Burgette, R. J., and Legresy, B. Unabated global mean sea-level rise over the satellite altimeter era. *Nature Climate Change*, 5(6):565–568, 2015. doi: 10.1038/nclimate2635.

Weertman, J. Stability of the junction of an ice sheet and an ice shelf. *Journal of Glaciology*, 13(67):3–11, 1974.

Whitworth III, T., Orsi, A. H., Kim, S.-J., Nowlin Jr, W. D., and Locarnini, R. A. WATER MASSES AND MIXING NEAR THE ANTARCTIC SLOPE FRONT. In *Ocean, Ice, and Atmosphere: Interactions at the Antarctic Continental Margin*, volume 75, pages 1–27. American Geophysical Union, 1998. doi: 10.1029/AR075p0001.

Williams, G. D., Bindoff, N. L., Marsland, S. J., and Rintoul, S. R. Formation and export of dense shelf water from the Adélie Depression, East Antarctica. *Journal of Geophysical Research*, 113(C4):C04039, 2008. doi: 10.1029/2007JC004346.

Williams, G. D., Meijers, A. J. S., Poole, A., Mathiot, P., Tamura, T., and Klocker, A. Late winter oceanography off the Sabrina and BANZARE coast (117-128°E), East Antarctica. *Deep-Sea Research Pt. II*, 58(9-10):1194–1210, 2011. doi: 10.1016/j.dsr2.2010.10.035.

Wingham, D. J., Shepherd, A., Muir, A., and Marshall, G. J. Mass balance of the Antarctic ice sheet. *Philosophical Transactions of the Royal Society A*, 364(1844):1627–35, 2006.

Wright, A. P., Young, D. A., Roberts, J. L., Schroeder, D. M., Bamber, J. L., Dowdeswell, J. a., Young, N. W., Le Brocq, a. M., Warner, R. C., Payne, a. J., Blankenship, D. D., van Ommen, T. D., and Siegert, M. J. Evidence of a hydrological connection between the ice divide and ice sheet margin in the Aurora Subglacial Basin, East Antarctica. *Journal of Geophysical Research*, 117(F1):F01033, 2012. doi: 10.1029/2011JF002066.

Young, D. A., Wright, A. P., Roberts, J. L., Warner, R. C., Young, N. W., Greenbaum, J. S., Schroeder, D. M., Holt, J. W., Sugden, D. E., Blankenship, D. D., van Ommen, T. D., and Siegert, M. J. A dynamic early East Antarctic Ice Sheet suggested by ice-covered fjord landscapes. *Nature*, 474(7349):72–75, 2011. doi: 10.1038/nature10114.

Young, D. A., Lindzey, L. E., Blankenship, D. D., Greenbaum, J. S., Garcia De Gorordo, A., Kempf, S. D., Roberts, J. L., Warner, R. C., Van Ommen, T., Siegert, M. J., and Le Meur, E. Land-ice elevation changes from photon-counting swath altimetry: first applications over the Antarctic ice sheet. *Journal of Glaciology*, 61(225):17–28, 2015. doi: 10.3189/2015JoG14J048.

Zwally, H. J., Giovinetto, M. B., Li, J., Cornejo, H. G., Beckley, M. A., Brenner, A. C., Saba, J. L., and Yi, D. Mass changes of the Greenland and Antarctic ice sheets and shelves and contributions to sea-level rise: 19922002. *Journal of Glaciology*, 51(175): 509–527, 2005. doi: 10.3189/172756505781829007.